DOT/FAA/TT-20/40

Federal Aviation Administration
William J. Hughes Technical Center
Aviation Research Division
Atlantic City International Airport
New Jersey 08405

Full-Field Measurement of the Taylor-Quinney Coefficient in Tension Tests of Ti-6Al-4V, Aluminum 2024-T351, and Inconel 718 at Various Strain Rates

October, 2020

Technical Thesis

The research described in this report was funded by the FAA as part of its mission to improve aircraft safety. The views and opinions expressed are those of the author alone and do not necessarily represent the views of the FAA. The FAA assumes no liability for the contents or use thereof. The FAA has not edited or modified the contents of the report in any manner.

This document is available to the U.S. public through the National Technical Information Services (NTIS), Springfield, Virginia 22161.

This document is also available from the Federal Aviation Administration William J. Hughes Technical Center at actlibrary.tc.faa.gov.

U.S. Department of Transportation
Federal Aviation Administration

NOTICE

This report is available at the Federal Aviation Administration William J. Hughes Technical Center's Full-Text Technical Reports page: actlibrary.tc.faa.gov in Adobe Acrobat portable document format (PDF).

Technical Report Documentation Page

Form DOT F 1700.7 (8-72) Reproduction of completed page authorized

1. Report No.	2. Government Accession No.	3. Recipient's Catalog No.
DOT/FAA/TCTT-20/40		

4. Title and Subtitle	5. Report Date
Full-Field Measurement of the Taylor-Quinney Coefficient in Tension Tests of Ti-6Al-4V, Aluminum 2024-T351, and Inconel 718 at Various Strain Rates	October 2020
	6. Performing Organization Code
7. Author(s)	8. Performing Organization Report No.
Jarrod Lee Smith	
9. Performing Organization Name and Address	10. Work Unit No. (TRAIS)
The Ohio State University Department of Mechanical Engineering Scott Laboratory 201 W 19th Ave Columbus, OH, 43214	11. Contract or Grant No. 16-G-007
12. Sponsoring Agency Name and Address	13. Type of Report and Period Covered
U.S. Department of Transportation Federal Aviation Administration Air Traffic Organization Operations Planning Office of Aviation Research and Development Washington, DC 20591	Technical Thesis
	14. Sponsoring Agency Code AIR-6A1

15. Supplementary Notes

The FAA William J. Hughes Technical Center Aviation Research Division Technical Monitor was Daniel Cordasco.

16. Abstract

During plastic deformation of metals only a portion of the plastic work done on the material is expended to modify its physical properties while the remaining energy is converted to heat. The associated rise in temperature during deformation can affect the mechanical response of the material (e.g. strain hardening, thermal softening, precipitating localizations, etc.). At low strain rates the conditions are virtually isothermal as there is sufficient time for the heat to transfer to the surroundings. At high strain rates the temperature in the metal can increase significantly and the conditions can become nearly adiabatic as the heat cannot dissipate to the surroundings. The portion of plastic work that is converted to heat is determined by the Taylor-Quinney coefficient (β) and is quantified by measuring both the plastic work and temperature rise in a material during deformation. By including the Taylor-Quinney coefficient, complex material models can more accurately model the thermoplastic deformation of the material over a wide range of strains, strain rates, and temperatures.

An experimental program is introduced to investigate the dependence of the Taylor-Quinney coefficient on strain rate and strain. Tension tests with specimens made of Ti-6Al-4V, Aluminum 2024-T351, and Inconel 718 are performed at various strain rates ranging from 1E-4 to 6000 s^{-1}. The quasi-static tests are completed on a hydraulic load frame while tests ranging from 500 to 6000 s^{-1} are completed using the split-Hopkinson bar (SHB) technique. Flat thin tensile specimens are used where strain is measured on one side of the specimen using 2D or 3D Digital Image Correlation (DIC) and simultaneous temperature measurements are recorded on the opposite side of the specimen via infrared thermography. A method to determine β by combining the full-field temperature and strain measurements together with the recorded force data is developed. The dependence of β on plastic strain and strain rate is determined.

17. Key Words	18. Distribution Statement
Taylor-Quinney, plastic work, plastic heat, thermoplastic, strain hardening, thermal softening, localization, split-Hopkinson bar, digital image correlation, infrared thermography, Aluminum 2024-T351, Ti-6Al-4V, Inconel 718	This document is available to the U.S. public through the National Technical Information Service (NTIS), Springfield, Virginia 22161. This document is also available from the Federal Aviation Administration William J. Hughes Technical Center at actlibrary.tc.faa.gov.

19. Security Classif. (of this report)	20. Security Classif. (of this page)	21. No. of Pages	22. Price
Unclassified	Unclassified		

Full-Field Measurement of the Taylor-Quinney Coefficient in Tension Tests of Ti-6Al-4V, Aluminum 2024-T351, and Inconel 718 at Various Strain Rates

Dissertation

Presented in Partial Fulfillment of the Requirements for the Degree Doctor of Philosophy in the Graduate School of The Ohio State University

By

Jarrod Lee Smith, M.S.

Graduate Program in Mechanical Engineering

The Ohio State University

2019

Dissertation Co mmittee

Dr. Amos Gilat, Advisor

Dr. Rebecca B. Dupaix

Dr. Prasad Mokashi

Dr. Soheil Soghrati

Abstract

During plastic deformation of metals only a portion of the plastic work done on the material is expended to modify its physical properties while the remaining energy is converted to heat. The associated rise in temperature during deformation can affect the mechanical response of the material (e.g. strain hardening, thermal softening, precipitating localizations, etc.). At low strain rates the conditions are virtually isothermal as there is sufficient time for the heat to transfer to the surroundings. At high strain rates the temperature in the metal can increase significantly and the conditions can become nearly adiabatic as the heat cannot dissipate to the surroundings. The portion of plastic work that is converted to heat is determined by the Taylor-Quinney coefficient (β) and is quantified by measuring both the plastic work and temperature rise in a material during deformation. By including the Taylor-Quinney coefficient, complex material models can more accurately model the thermoplastic deformation of the material over a wide range of strains, strain rates, and temperatures.

An experimental program is introduced to investigate the dependence of the Taylor-Quinney coefficient on strain rate and strain. Tension tests with specimens made of Ti-6Al-4V, Aluminum 2024-T351, and Inconel 718 are performed at various strain rates ranging from 1E-4 to 6000 s^{-1}. The quasi-static tests are completed on a hydraulic load frame while tests ranging from 500 to 6000 s^{-1} are completed using the split-

Hopkinson bar (SHB) technique. Flat thin tensile specimens are used where strain is measured on one side of the specimen using 2D or 3D Digital Image Correlation (DIC) and simultaneous temperature measurements are recorded on the opposite side of the specimen via infrared thermography. A method to determine β by combining the full-field temperature and strain measurements together with the recorded force data is developed. The dependence of β on plastic strain and strain rate is determined.

Dedication

This document is dedicated to my closest friends, my family,

and the memory of my mother.

Acknowledgments

Several people have helped me during my life to get to this point and I would like to take the time to thank them now. First I'd like to thank my parents Mike and Marsha whose inspiration, love, and courage throughout my life and academic career has made this possible. To my sisters Shanna and Maryssa: your guidance, love, and resilience throughout all the pitfalls and peaks of our lives has been a beacon for me to follow. To my brothers in life Bryan Middlebrooks and Jordan Misamore for being my closest confidants for the most important years of my life. To my closest friends- Patrick Burr, Lucy Leard, Michael Heit, Alex Rickels, Jon Bentley, Brandon Edwards, Ashley Kolbeck, Tim Jamison, David Dean, Blake Marble and MacGregor Obergfell - your friendship, support, and guidance has forever changed my life.

My Advisor, Dr. Amos Gilat has been both an inspiration and incredibly supportive throughout my time here and it has been a pleasure to work with him. Dr. Jeremy Seidt has been a tremendous mentor for me in and out of the laboratory and I'm eternally grateful for all of his help and guidance over the past few years. I would also like to thank Dr. Rebecca Dupaix, Dr. Prasad Mokashi, and Dr. Soheil Soghrati for taking the time to serve on my dissertation defense co mmittee.

This research was supported by the Federal Aviation Administration in collaboration with the National Aeronautics and Space Administration, George

Washington University and George Mason University. Thanks to William E mmerling, Chip Queitzsch, Dr. Tom Vasko, Dr. Daniel Cordasco at the FAA for their advice and support on the project. I would also like to thank other members of the FAA Aerospace Working Group Dr. J. Michael Pereira, Dr. Kelly Carney, Paul Du Bois, Dr. Cing-Dao (Steve) Kan, Dr. C.K. Park, Stefano Dolci, and Dr. Sean Haight.

Lastly, I would like to thank my fellow students and colleagues from the Dynamic Materials of Mechanics Laboratory: Kelton Rieske, Jeremiah Ha mmer, Dr. Kevin Gardner, Tim Liutkus, Aaron Ressa, Peiyu Yang, Dr. Robert Lowe, Stuart Brand, Lowell Toms, Mark Konieczny, Naiara Vazquez-Fernandez, Nathan Spulak, Brian Smith, and Elliott Harrod. These researchers have been an important part in my experience not only through providing insight in our discussions but also through their friendship.

Vita

2008.....Xenia High School

2012.....B.S. Mechanical Engineering
The Ohio State University

2012- present .....Graduate Research Associate, Dynamic Mechanics of Materials Laboratory, Department of Mechanical and Aerospace Engineering, The Ohio State University

2015.....M.S. Mechanical Engineering
The Ohio State University

Publications

J. L. Smith, "Ductile Fracture Behavior of a Nickel-Based Superalloy and Thermally- Induced Strain Behavior of an Aluminum Alloy," Ohio State University, 2015.

J. L. Smith, J. D. Seidt, and A. Gilat, "Full-Field Determination of the Taylor-Quinney Coefficient in Tension Tests of Ti-6Al-4V at Strain Rates up to 7000 s^{-1}," in Conference Proceedings of the Society for Experimental Mechanics Series, 2019. (In Preparation)

J. D. Seidt, V.-T. Kuokkala, J. L. Smith, and A. Gilat, "Synchronous Full-Field Strain and Temperature Measurement in Tensile Tests at Low, Intermediate and High Strain Rates," Experimental Mechanics, vol. 57, no. 2, pp. 219–229, 2017.

J. L. Smith, V.-T. Kuokkala, J. D. Seidt, and A. Gilat, "Full-field temperature and strain measurement in dynamic tension tests on SS 304," in Conference Proceedings of the Society for Experimental Mechanics Series, 2017, vol. 1B.

J. L. Smith, J. D. Seidt, and A. Gilat, "Thermal deformation analysis of an aluminum alloy utilizing 3D DIC," in Conference Proceedings of the Society for Experimental Mechanics Series, 2016, vol. 9.

J. L. Smith, V.-T. Kuokkala, J. D. Seidt, and A. Gilat, “Internal heat generation in tension tests of AISI 316 using full-field temperature and strain measurements,” in Conference Proceedings of the Society for Experimental Mechanics Series, 2018, vol. 3, pp. 97–103.

A. Gilat, V.-T. Kuokkala, J. D. Seidt, and J. L. Smith, “Full-Field Measurement of Strain and Temperature in Quasi-Static and Dynamic Tensile Tests on Stainless Steel 316L,” Procedia Eng., vol. 207, pp. 1994–1999, 2017.

P. Gilmore, V.-B. Sundaresan, J. Seidt, and J. Smith, “Design and analysis of a synthetic jet actuator-based fluid atomization device,” Journal of Intelligent Materials Systems and Structures, vol. 28, no. 17, 2017.

Fields of Study

Major Field: Mechanical Engineering

Specializations: Experimental Mechanics, Dynamic Behavior of Materials, Plasticity, Computational Mechanics, Infrared Thermography

Table of Contents

List of Tables

List of Figures

Chapter 1 Introduction

1.1 Motivation and Objectives

The design of co mmercial jet engines has been under intense scrutiny since their inception due to their catastrophic and fatal potential in the event of failure. An uncontained blade-off event is the most potentially damaging accident and occurs when a single blade in the engine detaches from the main rotor hub, is ejected laterally through the engine shroud, and causes damage such as: puncturing the main fuselage, cutting essential fuel lines, or damaging the attachment structure of the engine to the airframe. On July 19, 1989 a DC-10 experienced an uncontained engine failure in its tail-mounted engine which led to the failure of the engine and the loss of all hydraulic flight controls. With the assistance of a DC-10 flight instructor who was onboard, the pilots were able to assume limited control the aircraft with the use of differential power in the two wing-mounted engines and performed an emergency landing at Sioux City International Airport, Iowa. Of the 296 passengers and crew onboard, 185 survived. After a thorough accident investigation the National Transportation Safety Board (NTSB) concluded in its report that the titanium first-stage fan disc on the tail engine contained a manufacturing defect that created a hairline crack after thousands of operational hours [3]. The disk then separated during flight, was ejected through the engine shroud, and severed all three of

the plane's hydraulic lines. Images of the failed fan disk, recovery of the fan disk, and an investigative recreation of the failed engine are shown in Figure 1.1.

From these findings the NTSB had several reco mmendations for reducing the disastrous consequences of blade-off events and created the Systems Review Task Force (SRTF) comprised of the Federal Aviation Administration (FAA) Research and Development Advisory Co mmittee and industry members Boeing, Douglas, Airbus, Lockheed, General Electric, Pratt & Whitney, and Rolls Royce. Within the SRTF was an Engine Containment Working Group focused on the

"…categorization of parts that may not be contained in the event of failure. This concept states that there are parts that cannot be contained by any known means. The group's approach to this problem is to identify the potential parts in this group, to characterize their damage potential to the airplanes, and to pay special attention to them during design, in-service inspection, and repair." [3]

This working group eventually evolved into the FAA Aircraft Catastrophic Failure Prevention Program (ACFPP) which was created by the United States Congress under the Omnibus Budget Reconciliation Act of 1990. The explicit goal of this program is stated as the following:

"…to develop technologies and methods to assess the risk or and prevent defects, failures and malfunctions of products, parts, processes and articles manufactured for use in aircraft, aircraft engines, propellers, and appliances which could result in a catastrophic failure of an aircraft." [5]

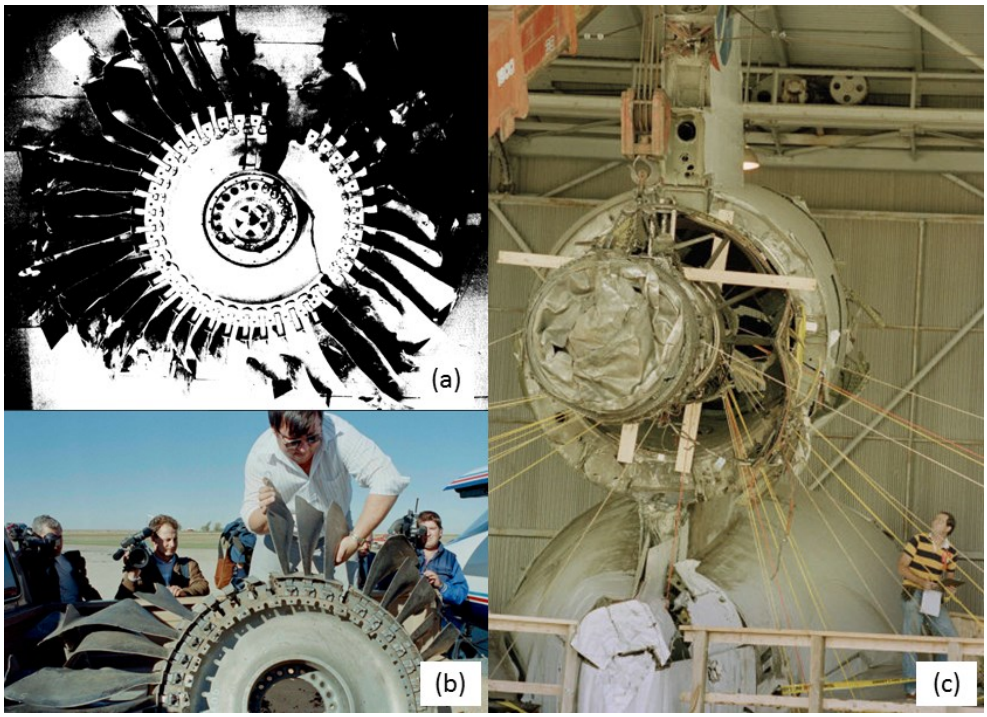

Figure 1.1 (a) No.2 Engine Stage 1 Fan Disk Reconstructed with Blades [3] (b) Recovery of a Fan Disk Blade from the No.2 Engine [4] (c) Recreation of the Tail Engine to Investigate the Ejection of Fan Blades after Failure [4]

With these stated goals in mind, the FAA ACFPP has sponsored research since the mid-1990s focusing on mitigating blade-off events by developing physics-based material models that can accurately predict the failure modes and damage caused by turbine engine fragments. These new analysis tools are to be provided across the aerospace industry to standardize the analysis, design, and certification phases of engine development.

During each blade-off event the projectiles and containment rings realize high strain rates, elevated temperatures, and complex states of stress and therefore the data used to calibrate these models must come from physical tests in those conditions. Through a collaborative effort between the FAA, the National Aeronautics and Space

Administration at the Glenn Research Center (NASA-GRC) Impact Dynamics Group, the Ohio State University (OSU) Dynamic Mechanics Material Laboratory (D MML), the Center for Collision Safety and Analysis (CCSA) at George Mason University (GMU) and the LS-DYNA Aerospace Working Group (AWG) a family of tabulated plasticity models (MAT_224, MAT_224_GYS, and MAT_264) based on the Johnson-Cook approach has been developed for Ti-6Al-4V, Aluminum 2024-T351, and Inconel 718 in LS-DYNA [6]–[12]. For each model an extensive material characterization was carried out by OSU D MML, experimental data was delivered to GMU for model development, and the model simulations were compared against dynamic impact data from NASA-GRC tests. All models have the ability to consider the plastic strain as a function of stress state, strain rate, and temperature. The resultant temperatures in each material model are based on the following equation:

$$T = T_0 + \frac{\beta}{c_p \rho} \int_0^{\epsilon_p} \sigma_p \dot{\epsilon}_p \, dt \quad (1\text{-}1)$$

Where T is the material temperature, T_0 is the ambient temperature, $c_p$is the specific heat, ρ is the density, σ_p is the plastic stress, ϵ_p is the plastic strain, $\dot{\epsilon}_p$ is the plastic strain rate, and β is the Taylor-Quinney coefficient. In the current material models the Taylor-Quinney coefficient is a constant. However, previous works have shown that β is strain and strain rate dependent in compression tests [13]–[15]. Each of the LS-DYNA material models can support a variable Taylor-Quinney coefficient based on reliable physical data. This study will further calibrate the material models by determining the temperature increase due to plastic work for Ti-6Al-4V, Aluminum

2024-T351, and Inconel 718 using coupled load, strain, and temperature measurements. Tension tests are carried out on the same 12.7 mm thick plates that were used in previous experiments to maintain a consistent methodology. Plastic strain and strain rate dependence of the Taylor-Quinney coefficient is found by testing in tension at strain rates from 1.0E-4 to 6000 s^{-1} for each material.

1.2 Literature Review

Several researchers have studied the conversion of plastic work into heat. The first attempts to quantify the fraction of plastic work stored as cold work versus released as heat were conducted by Farren and Taylor [16] and Taylor and Quinney[17]. In these experiments, large torsional plastic strains were induced in mild steel, pure iron, and copper rods using a geared torsional apparatus. The temperature of each rod was recorded with a thermocouple on the surface of each sample and with a calorimeter i mmediately following the loading. In these tests they concluded that the fraction of plastic work converted to heat was greater than or equal to 0.85. They also concluded that the fraction of work converted to heat was nearly constant for copper and mild steel over a range of strains. For many years following these experiments, β was assumed to be a constant value between 0.85 and 1 and insensitive to strain and strain rate. A review of similar experiments is thoroughly explored in Bever et al. [18].

Mason et al. [15] performed the first attempt to quantify the dependence of β on strain and strain rate in Aluminum 2024, 4340 steel and Ti-6Al-4V using a compression Kolsky bar and a high speed infrared detector first designed to measure temperatures in a

propagating crack by Zehnder et al. [19]. The detector consisted of 8 individual InSb sensors sensitive to radiation with wavelengths from 1 to 5.5 μm and operated with a sampling rate of 2 MHz. The detectors were calibrated by placing the specimen in the experimental apparatus and simultaneously measuring the temperature of the sample and the voltage output of the sensor. Specimens of Aluminum 2024, Ti-6Al-4V and 4340 Steel were tested to failure at strain rates from 1000 to 3000 s^{-1}. The values of β obtained for Aluminum 2024 and 4340 calculated to be 0.85 matching earlier low strain rate tests [5] which means β is not rate sensitive for these materials. Ti-6Al-4V showed signs of strain sensitivity as β increased from 0.65 at 3% strain to 0.95 at a strain of 5% then decreased to 0.5 at a strain of 18%. The measured temperature values from the 4340-steel test revealed that the temperature field on the surface of each specimen were inhomogeneous which called into question the strain energy measurement for the calculation of β. Utilizing the same infrared detector, Hodowany [14] performed compression tests on Aluminum 2024 and alpha-Titanium. In each test it was assumed the specimen experienced homogeneous deformation, uniform temperature distribution, adiabatic behavior, and negligible thermoelastic heating. Aluminum 2024 was found to be strain dependent as β increased from 0.3 to 1 during plastic deformation from 2 to 55% plastic strain.

It is important to mention that these calculations of β are defined as β_{diff} which differs from another calculation of β known as β_{int}. This difference in β calculation was first noted by Rittel [20] and is described by the following equations: $\beta_{int} = \frac{\rho c_p \Delta T}{\int_0^t W_p}$ (1-2)

or $\beta_{diff} = \frac{\rho c_p \dot{T}}{d\dot{W}_p}$ (1-3) where ρ is the density of the material, c_p is the specific heat of the material, ΔT is the change in temperature, $\dot{T}$ is the rate of the change in temperature, $\int_0^t W_p$ is the plastic work and $d\dot{W}_p$ is the rate mechanical power. β_{int} is a relation of the thermal dissipation to mechanical work and requires simultaneous strain and temperature measurements. β_{diff} is the ratio of the rate of thermal dissipation to mechanical power and is calculated from the derivatives of the best fit curves of the plastic work and temperature data.

Several other researchers have used similar methods to determine the fraction of plastic work converted to heat in metals during high strain rate deformation assuming adiabatic conditions. Kapoor and Nemat-Nasser [21] calculated the temperature rise in compression tests of Ta-2.5% W alloy, pure Titanium, 1018 Steel, 6061 Aluminum and OFHC Copper at strain rates of 3000 s^{-1}. The temperature increase was determined with a 2 mm InSb sensor divided into 4 separate quadrants connected to a 1MHz amplifier. Errors in temperature measurement on the surface of the specimen due to the curve of the surface or the roughness caused by plastic deformation were assumed to be negligible. β_{int} for the various materials were calculated to range from 0.6 to 0.85 but strain and strain rate sensitivity was not investigated.

Macdougall and Harding [22] measured β_{diff} in torsion tests of Ti-6Al-4V and also measured the surface temperature of tension tests at strain rates on the order of 1000 s^{-1}. Temperatures were measured using a 12-element Hg-Cd-Te radiometer sensitive to radiation in the range of 2 to 5.5 μm. The researchers used a calibration method similar to

[12] and [16] but found their temperatures to be underestimated. Macdougall [23] created a new calibration system that removed extraneous sources of radiation and allowed the temperature of the specimen to be more closely monitored and controlled. With the new calibration method Macdougall found the β_{diff} in the torsion tests increased from 0.6 at 2% strain to 0.9 at 5% strain and remained at 0.9 up to 30% strain. β_{diff} values were not calculated for the tension tests as the strain in the necking region of the specimen could not be properly evaluated.

More recently, Rittel et al. [13] studied β_{int} for Ti-6Al-4V, Aluminum 2024 and 5086, SS 304L, 1020 Steel and C300 in compression, tension and shear at strain rates ranging from 1200 to 7000 s^{-1}. The β_{int} for Ti-6Al-4V was strain dependent as β_{int} decreased from 0.5 to 0.38 with strains from 2 to 35%. Similarly, Aluminum 2024 was slightly strain dependent as β_{int} decreased from 0.4 at a strain of 5% to 0.25 at a strain of 10% strain and then remained constant at 0.25 up to a strain of 30%. Neither material was strain rate or loading mode dependent. β_{int} in tension could only be calculated from strains of 2 to 7% because the determination of the strain energy from the engineering stress and strain is no longer valid once homogeneous deformation ends and necking begins.

Simultaneous temperature and DIC measurements have been recorded by multiple researchers at low strain rates [24]–[31] but only two of these researchers investigated the partition of plastic work converted to heat. Knysh [28] tested slender rods of 303 and 316 stainless steel, co mmercial-pure titanium, and Ti-6Al-4V inside a thermally isolated vacuum tube with well-defined thermal boundary conditions to emulate a simple 1D heat

transfer model. 2D-DIC images were taken on one side of the specimen with a single 2MPixel camera while infrared images were captured simultaneously with a FLIR SC-645 infrared camera capable of detecting temperature from -20ºC to 150ºC at a spatial resolution of 640x480 pixels. The infrared camera viewed the specimen through a potassium bromide window allowing all relevant wavelengths of infrared to be visible to the camera. Tests were conducted at strain rates from 0.001 to 0.01 s^{-1} meaning tests were not adiabatic in nature. Using the 1D heat transfer model the heat generated from deformation was isolated from the heating caused by conduction in the rod. It was found that β_{int} is not constant with the plastic strain, instead it drops as the plastic deformation accumulates. In most cases β_{int} varied between 0.55 and 0.8. All 4 metals exhibited strain rate dependency as β_{int} increased with increasing strain rate although the stainless steels were less strain rate dependent.

Duomoulin [31] measured the displacement and temperature fields in 3 different TRIP steels during tensile loading tests at a strain rate of 1.7E-3 s^{-1}. Utilizing the simultaneous measurements, a thermodynamically consistent elastic-plastic constitutive model including the von Mises yield criterion with the associated flow rule could be employed with a local heat diffusion equation to recreate the behavior exhibited during the test. The model was able to recreate the Lüders band phenomena and was also successful in capturing β_{diff} which remains constant at 0.6 throughout the test.

Chapter 2 Experimental Procedures and Techniques

This chapter presents the experimental program that was used to measure the Taylor-Quinney coefficient of Aluminum 2024, Ti-6Al-4V, and Inconel 718 over a range of strain rates in tension. Loading techniques for the quasi-static and dynamic strain rate tests and the analysis of experimental data are described. A novel method to combine full-field strain and temperature measurements is presented.

2.1 Material Selection

Materials used in these tension experiment are from the same production lots as the preceding Aluminum 2024-T351 [8], Ti-6Al-4V [6], [10], and Inconel 718 [7], [9] characterization studies. Using material from the same production lots removes material variations that could occur from plate to plate which could obscure results and impact the overall performance of the material model. The chemical makeup from the Aluminum 2024-T351 12.7 mm plate obtained from Kaiser Aluminum is presented in Table 2.1.

Table 2.1 Chemical Composition of Aluminum2024-T351 12.7 mm Plate

Material/Alloy/Treatment	Chemistry									
	Si	Fe	Cu	Mn	Cr	Zn	Ti	V	Zr	Al
Aluminum 2024-T351	0.08	0.22	4.47	0.59	1.37	0.01	0.18	0.02	0.01	bal

The Ti-6Al-4V 12.7 mm plate was obtained from Titanium Industries Inc. and its chemical makeup was determined by the NASA – Glenn Research Center as shown in Table 2.2 Chemical Composition of Titainium-6Al-4V 12.7 mm Plate

Table 2.2 Chemical Composition of Titainium-6Al-4V 12.7 mm Plate

Material/Alloy	Chemistry						
	Al	V	Fe	O	C	N	Ti
Titanium-6Al-4V	6.64	4.04	0.13	0.19	0.011	0.006	bal

The Inconel 718 12.7 mm plate was obtained from Allegheny Ludlum in the annealed condition and then heat treated using the method presented in Table 2.3.

Table 2.3 Heat Treatment of Inconel 718 12.7 mm Plate

Phase	Duration (hrs.)	Description
Temperature Hold	8	Hold at 718ºC
Ramp Cool	1.76	Ramp Cool at 55ºC/hr
Temperature Hold	8	Hold at 621ºC

The material composition of the Inconel 718 plate is summarized in Table 2.4:

Table 2.4 Chemical Composition of Inconel 718 12.7 mm Plate

	Chemistry															
Material/Alloy	C	Mn	P	S	Si	Ni	Cr	Mo	Co	Cu	Al	Ti	Cb	B	Fe	Ta
Inconel 718	0.048	0.08	0.008	0.0001	0.072	52.6	18.32	2.87	0.2	0.034	0.54	1.02	4.94	0.0029	9.25	0.01

2.2 Specimen Design

Tensile tests are conducted on thin flat dog-bone specimens of each material shown in Figure 2.1 at strain rates 1 E-4 s^{-1}, 1 E-1 s^{-1}, 1 s^{-1}, 500 s^{-1}, 2000 s^{-1}, and 6000 s^{-1}. These specimens are used to study the strain and strain rate dependence of the temperature rise and related Taylor-Quinney coefficient of each material. The gage section of 5.08 mm is standard for each specimen and is constrained by the duration of the tensile wave that can be generated in the split-Hopkinson bars. The width of the gage section varies for each material due to differences in ultimate stress of each material and the limited incident force that can be transmitted by the split-Hopkinson bars. Modifications are made to the tabs of each specimen to allow for the specimen to be

attached to each loading apparatus. The specimens for load frame have an increased tab length of 31.75 mm while those tested on the direct tension SHB have 3.97 mm diameter through holes in the center of the tab. These modifications do not affect the gage area of the specimen and should not affect results. Each specimen is Electric Discharge Machine (EDM) wire cut from 0.5" plates of each material in the rolling direction. The surface of each specimen is ground to remove the recast EDM layer and cleaned with ethanol to ensure a consistent surface finish. An inconsistent surface finish can result in differences in emissivity and a reduction in the material strength properties between comparable specimens. The width and thickness of each specimen is measured before each test to ensure that slight variances in the machining and grinding of each individual specimen does not affect the calculation of engineering stress. An overview of the test program is shown in Table 2.5.

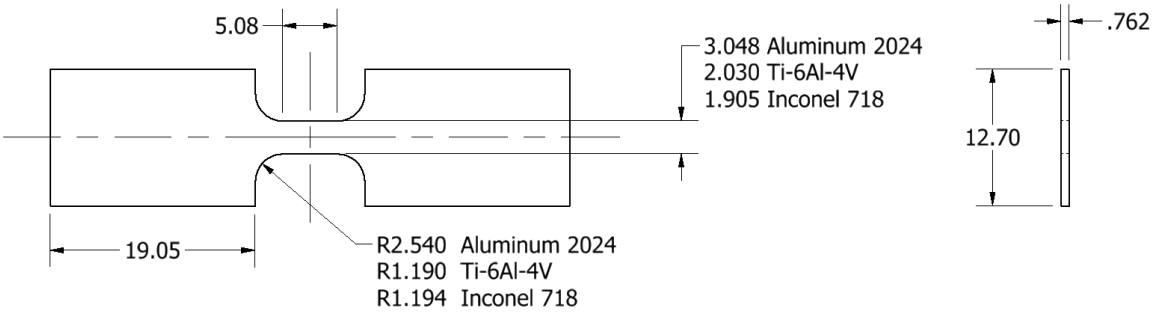

Figure 2.1 Specimen Geometry for each Material

Table 2.5 Experimental Test Program Overview

Material	Strain Rate (s^{-1})	Experimental Apparatus	Target Actuator Velocity
Aluminum 2024-T351 Ti-6Al-4V Inconel 718	1.00E-04	Hydraulic Load Frame	5.08E-4 mm/s
	0.1		0.508 mm/s
	1		5.08 mm/s
	500	Direct Tension Split-Hopkinson Bar	2.54 m/s
	2000		10.16 m/s
	6000	Direct Impact Split-Hopkinson Bar	40.64 m/s

2.3 Quasi-Static Tensile Test Procedure

Quasi-static tensile tests at strain rates of 1 E-4 s^{-1}, 0.1 s^{-1}, and 1 s^{-1} are carried out on an Instron 1321 servo-hydraulic biaxial load frame. The machine is equipped with an Interface 1216CEW-2K load cell capable of recording a maximum uniaxial load of 8.896 kN and a torque maximum of 113 N-m. The axial displacement of the load frame is controlled by Multipurpose Testing Software and an MTS FlexTest SE controller connected to a Linear Variable Differential Transformer (LVDT) inside the load frame. The MTS FlexTest SE also records the digital data output by the load cell, LVDT, and Rotary Variable Differential Transformer (RVDT). Specimens are attached to the machine using MTS647.02B-22 hydraulic wedge grips. The faces of the grips are placed in contact with each specimen and the controller is set to load control to maintain the axial load at 0 N on the specimen while the grips are clamped to a force of 4500 N. Each specimen is deformed by running an axial ramp program on the controller. The displacement velocity of each program is calculated by multiplying the desired strain rate

by the gage length of the specimen. The engineering stress during each tension test is determined by the following:

$$\sigma_e(t) = \frac{F(t)}{A_s} \quad (2\text{-}1)$$

Where $\sigma_e(t)$ is the engineering stress, $F(t)$ is the force measured by the load cell, and A_s is the original area of the specimen. An image of the MTS setup is shown in Figure 2.2.

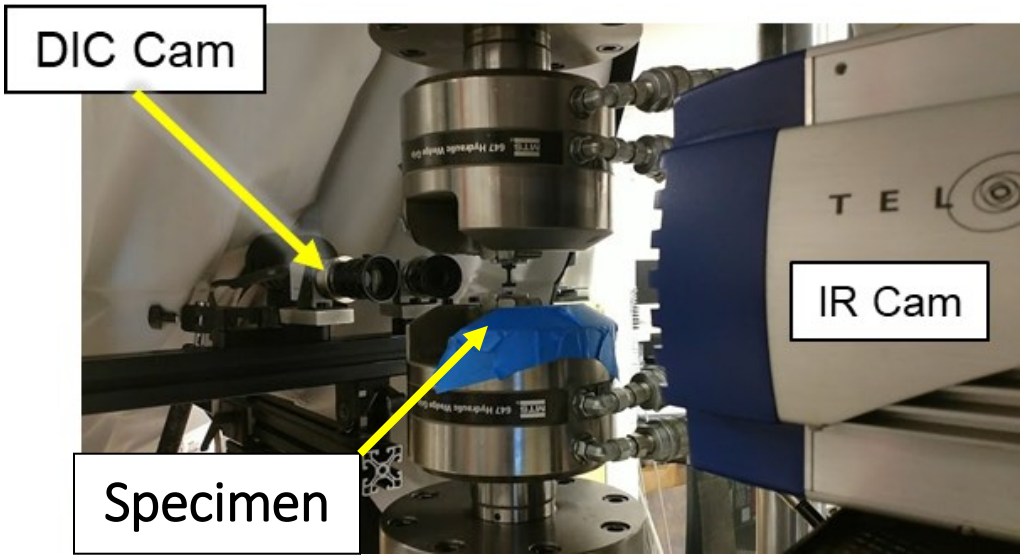

Figure 2.2 Overview of the Load Frame Test Setup

2.4 Direct Tension Split Hopkinson Bar Procedure

Tensile tests at strain rates of 500 s^{-1} and 2000 s^{-1} are performed for each material on a direct tension split-Hopkinson bar designed by Staab and Gilat [32]. The apparatus consists of two 12.7 mm diameter aluminum 7075 bars: a 3.68m long incident bar and a 1.83m long transmitter bar. Each test specimen is placed between the two bars by epoxying the specimen into two 12.7 mm diameter aluminum 2024 slotted adapters and then epoxying the entire assembly to the bars. The adapters are designed to ensure that

impedance mismatches between the bars and specimen assembly are kept to a minimum to reduce wave reflections. A schematic and experimental setup overview of the direct tension bar are presented in Figure 2.3 and Figure 2.4. Each tensile test is performed by first clamping the incident bar with a modified vise clamp at the mid-span and then applying a static tensile force to the end using a pulley system. The applied tensile force is proportional to the strain rate of the test and is measured by foil strain gages in a Wheatstone bridge configuration located between the end of the bar and the modified vise clamp. Once the incident bar is loaded to the appropriate tensile force a fracture pin located in the vise grip is loaded to failure by a hydraulic C-clamp and an elastic tensile wave (ϵ_i) is generated in the incident bar. The specimen begins to plastically deform as the wave travels through the specimen due to differences in the displacements at the ends of the incident and transmitter bars. Part of the tensile wave passes through the specimen (ϵ_t) while a compressive wave is reflected in the incident bar (ϵ_r). The strains generated by the incident, reflected, and transmitted waves in the respective bars are measured by three different Wheatstone bridges labeled Gage A, Gage B, Gage C. Each bridge consists of four Micro-Measurements ED-DY-075AM-10C 1000Ω strain gages and are powered by a 15.0V DC excitation voltage through two Hewlett-Packard 6200B power supplies. The signal from each bridge is amplified by a Tektronix ADA435A Differential preamplifier with a 100kHz low pass filter and are measured using an 8 bit Tektronix TDS5034B oscilloscope sampling at 5MHz. A fourth strain gage arrangement is located 0.156m from Gage C and consists of 4 KSP-21K-E4 Kyowa 1000Ω semiconductor strain gages arranged in a half Wheatstone bridge. This arrangement has a higher sensitivity

than the foil bridges used in Gages A-C and is used as a redundant force check in these experiments.

The velocities at the end of each bar are denoted by $\dot{u}_i(t)$ for the incident bar and $\dot{u}_t(t)$ for the transmitter bar and can be determined at any time t by using 1-D wave propagation theory as follows:

$$\dot{u}_i(t) = \frac{1}{\rho_b A_b c_b}\left[F_A\left(t - \frac{L_A}{c_b}\right) + F_A\left(t - \frac{L_A}{c_b} + \frac{2L_B}{c_b}\right) - F_B\left(t + \frac{L_B}{c_b}\right)\right] \quad (2\text{-}2)$$

and

$$\dot{u}_t(t) = \frac{1}{\rho_b A_b c_b}\left[F_C\left(t - \frac{L_C}{c_b}\right)\right] \quad (2\text{-}3)$$

Where ρ_b is the density of the bars, A_b is the cross-sectional area of the bars, and c_b is the elastic wave speed of the bars. The forces measured by the strain gage bridges A, B and C are represented by F_A, F_B and F_C respectively. L_A , L_B , and L_C are the measured distances from the bar ends to the stain gage bridges A, B, and C respectively. Assuming the specimen undergoes homogeneous deformation the engineering strain rate $\dot{\epsilon_e}$ can be determined from the bar velocities and the specimen's original gage length, L_s,

$$\dot{\epsilon}_e(t) = \frac{\dot{u}_i(t) - \dot{u}_t(t)}{L_s} \quad (2\text{-}4)$$

The instantaneous engineering strain $\epsilon_e(t)$ can be found from the end displacements of each bar ($u_i(t)$, $u_t(t)$) or by integrating the strain rate history,

$$\epsilon_e(t) = \frac{u_i(t) - u_t(t)}{L_s} = \int_0^t \dot{\epsilon}(t)dt \quad (2\text{-}5)$$

Engineering stress σ_e in the specimen at time t is expressed by

$$\sigma_e(t) = \frac{F_C}{A_s}\left(t + \frac{L_C}{c_b}\right) \quad (2\text{-}6)$$

where A_s is the original cross section area of the specimen.

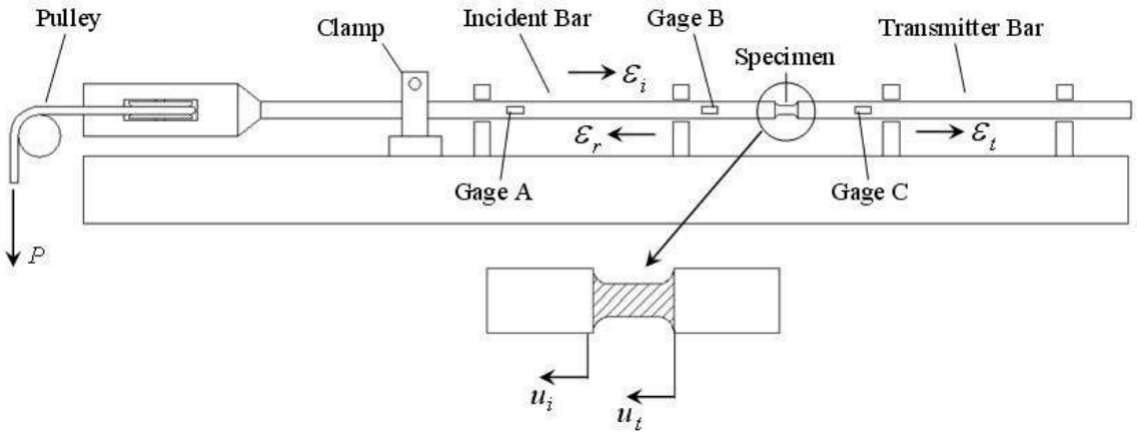

Figure 2.3 Schematic of the Direct Tension Split-Hopkinson Bar [8]

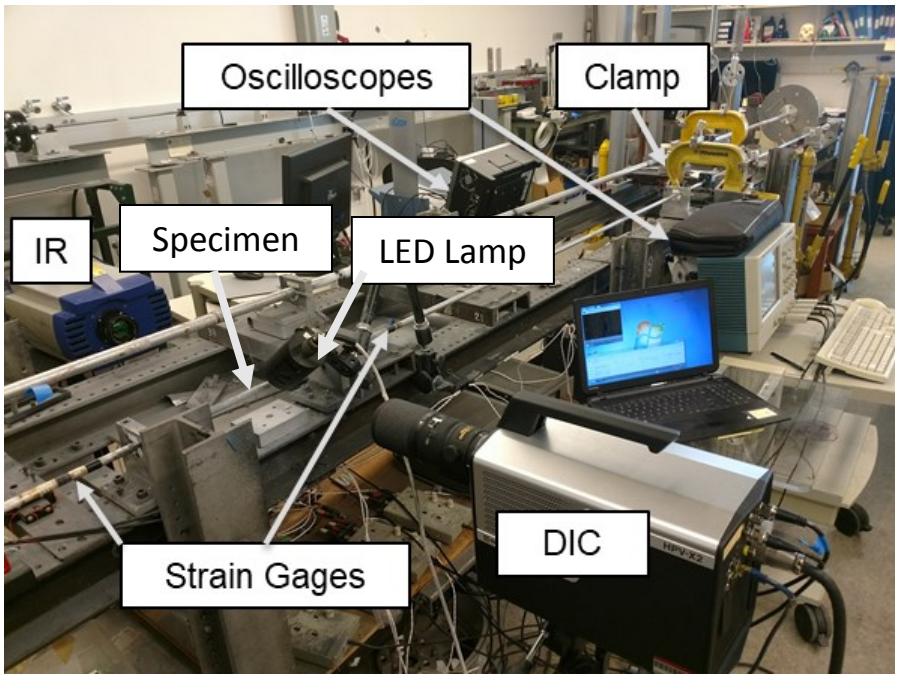

Figure 2.4 Overview of the Direct Tension Split-Hopkinson Bar Setup

2.5 Direct Impact Split-Hopkinson Bar Procedure

A direct impact split-Hopkinson bar is used to test tension specimens to failure strain rates of 6000 s^{-1}. The tension bar design is similar to that of Ogawa [33] and uses a gas gun and striker tube to generate an elastic tensile wave. A schematic of the apparatus

is presented in Figure 2.5. In this apparatus, a hollow striker tube is propelled over the incident bar by a sabot and pressurized shop air stored in the tank of the gas gun. The pressure of the air used to propel the striker tube is proportional to the velocity of the tube and the strain rate of each test. When the striker tube impacts the transfer flange attached to the end of the incident bar an elastic tensile wave is generated and propagates toward the specimen. As the wave travels through the incident bar Gage A measures the incident wave (ϵ_i). The portion of the wave that is transmitted through the specimen (ϵ_t) is measured by Gages B and C on the transmitter bar and the reflected wave measured in the incident bar (ϵ_r) is measured by Gage A. The amplitude of the initial elastic wave is proportional to the velocity of the striker and is determined by

$$\epsilon_i = \frac{v}{2c_b} \qquad (2\text{-}7)$$

where v is the velocity of the striker and c_b is the elastic wave speed of the incident bar. The relative displacement $\dot{u}$ and engineering strain rate $\dot{\epsilon}_e$ are determined from 1-D wave theory:

$$\boldsymbol{\dot{u}(t) = 2c_b\epsilon_r(t)} \qquad (2\text{-}8)$$

$$\boldsymbol{\dot{\epsilon}_e(t) = \frac{\dot{u}(t)}{L_s}} \quad (2\text{-}9)$$

where F_A is the force of the reflected wave measured at Gage A, A_B is the area of the bar, E_B is the elastic modulus of the bar, and L_s is the original length of the gage section of the specimen. Engineering stress $\sigma_e(t)$ is calculated by:

$$\boldsymbol{\sigma_e(t) = \frac{F_B(t)}{A_s}} \qquad (2\text{-}10)$$

where A_s is the original cross section area of the specimen, $F_B(t)$ is the force measured by Gage B. The test setup including the experimental apparatus is presented in Figure 2.6. The 15.875 mm diameter Ti-6Al-4V incident and transmitter bars are 3568 mm and 1828 mm long respectively. The striker tube with an inside diameter of 16.51 mm and outside diameter of 22.91 mm and a length of 609.6 mm generates an elastic strain pulse of 240.5 μs. The foil strain gages at Gage A and Gage B and the semiconductor bridge at Gage C are identical to those used on the direct tension SHB. The excitation voltages, power supplies, amplifiers and oscilloscope are also identical to those used in the direct tension SHB test.

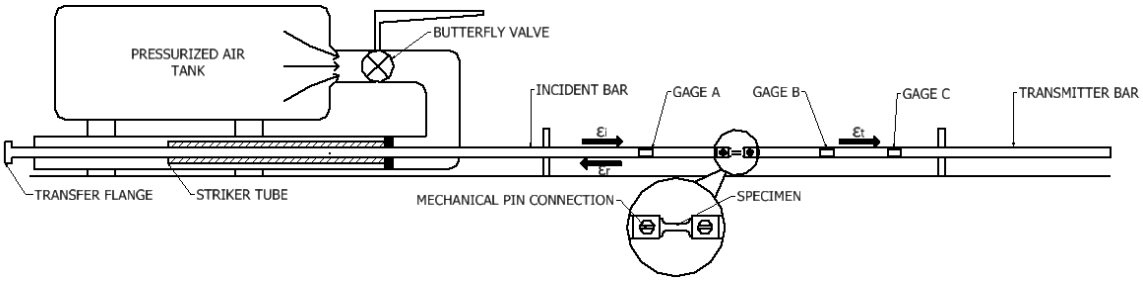

Figure 2.5 Direct Impact Split-Hopkinson Bar Schematic

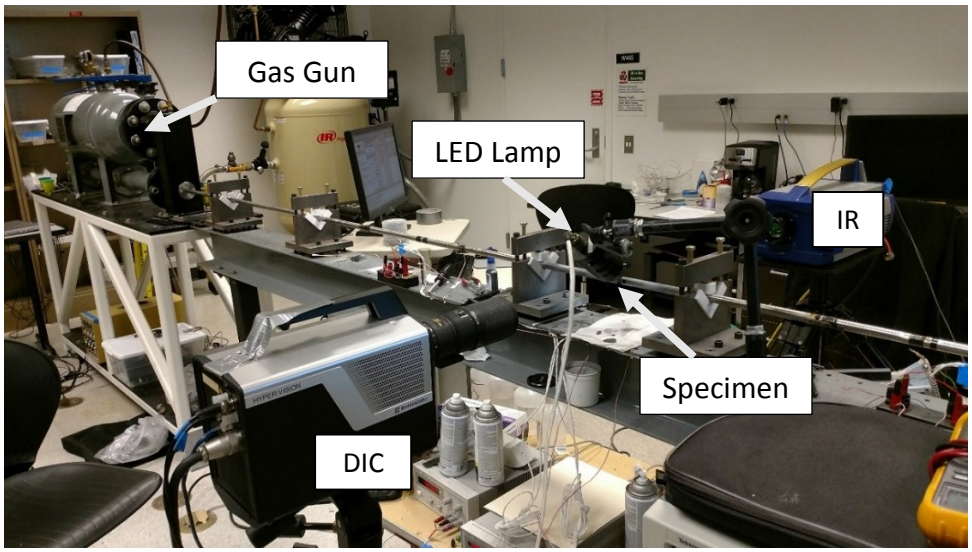

Figure 2.6 Overview of the Direct Impact Split-Hopkinson Bar Setup

2.6 Digital Image Correlation

Digital Image Correlation (DIC) is a noncontact optical technique to measure the displacements and strains on the surface of a deforming test specimen. A review of all relevant theory and practice of the DIC technique to experimental mechanics is provided by Sutton et al [34]. Two dimensional (2D) and three dimensional (3D) DIC techniques are used in the current work. The displacements and strains for each relevant test are resolved using VIC-2D 6 and VIC-3D 7 distributed by Correlated Solutions [35].

The basic concept of DIC involves tracking the deformation of a subset of nxn pixels through consecutive digital images during deformation. Each subset is characterized by the grayscale values of the pixels in each subset. A speckle pattern is applied to each specimen before the test to ensure a high contrast surface finish and distinct grayscale values within each subset. In the present experiments a speckle pattern was applied using a white spray paint to apply a primer layer followed by a misting of black spray paint as shown in Figure 2.7. The deformation points on the surface are determined by the step parameter which tells the software to place a subset center at every nth pixel. The strain on the surface is determined using an algorithm in the DIC software and a strain tensor definition. A logarithmic Hencky strain tensor is used in the experiments. The strains are smoothed with a 90% center weighted gaussian filter over a user defined number of displacement data points determined by the size of the filter parameter. The virtual strain gage length is calculated by the following equation:

$$\boldsymbol{VSG} = \frac{\boldsymbol{mm}}{\boldsymbol{pixel}} \times \boldsymbol{Step} \times \boldsymbol{Filter} \quad \textbf{(2-11)}$$

where $\frac{mm}{pixel}$ is the physical length of each pixel in the image determined by the camera placement and lens type. The virtual strain gage length is used in sizing the mesh for the numerical simulations and is important in comparing results. The filter is adjusted between the different tests to keep the VSG between 0.295-0.335 mm. In these tests the u,v,w, displacements and exx,exy,eyy strains are recorded for each pixel on the surface of the specimen and a 4 mm-EXT is used to describe the average strain seen by the gage section during the experiment. The displacement of a single data point located at near the point of failure and maximum strain is also extracted for each test. The location of these inspection elements on the DIC image is shown in Figure 2.7.

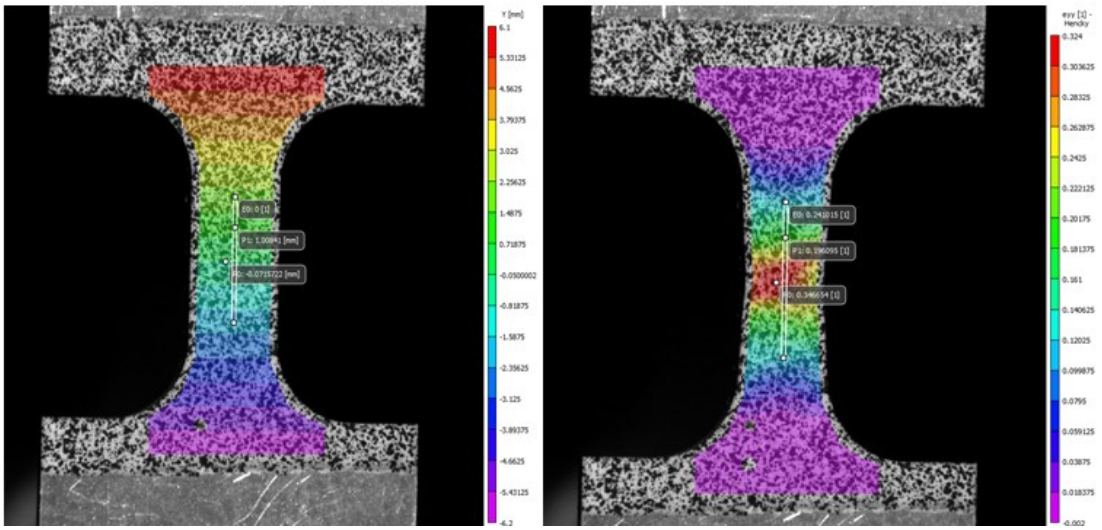

Figure 2.7 Placement of 4 mm-Ext and Point at Failure (left) in Y mm before Deformation (right) before Failure for an Aluminum 2024-T351 test

The 3D-DIC test setup for the low strain rate tests shown in Figure 2.2 utilizes two Photron MC2 cameras to record synchronized images at rates from 0.2-2000 frames per second (fps) at a pixel resolution of 512x512. Schnieder 35 mm lenses are used with the cameras. The cameras are placed 10-20 degrees from one another with nearly

identical focal lengths. 20-30 images are taken of a calibration grid of 81dots which equally spaced by a known distance to calibrate the cameras and determine a global 3D coordinate system. Displacements are measured in the global 3D coordinate system then transformed to the 3D coordinates of each camera which are then projected to the sensor coordinate plane of each using 2 consecutive transformations. On the sensor coordinate plane the deformations and strains are projected onto each individual pixel in the digital images from each camera.

Table 2.6. Overview of the Visual Camera Parameters used for DIC in each Experiment

Strain Rate (s^{-1})	Camera	Pixel Resolution	Frame Rate (fps)
1 E-4	2 x Photron MC2	512x512	0.2
0.1			200
1			2,000
500	Shimadzu HPV-X2	400x250	200,000
2000			625,000
6000			1,000,000

The high strain rate experiments utilize a Shimadzu HPV-X2 camera which operates at a constant 400x250 pixel resolution at frame rates from 200,000 to 1,000,000 fps to perform 2D-DIC. A 200 mm Nikon lens is used with the camera. 2D-DIC can introduce errors due to localization of the specimen material and out of plane motion. The error caused by these factors is estimated by the following equation[34]:

$$\in = \frac{100\times\left(\frac{w}{z}\right)}{\epsilon_{nn}} \qquad \textbf{(2-12)}$$

Where w is the out of plane motion, z is the distance from the camera and ϵ_{nn} is the observed maximum uniaxial strain in the localization. During the low rate experiments the maximum out of plane displacement measured with 3D-DIC was 0.155 mm and the maximum strain measured in the localization region during a high rate tension test was

measured as 0.475. The distance from the camera to each high strain rate specimen is 0.5-0.6 m resulting in a maximum 0.054-0.065% error in the strain measurement. An overview of the frame rates used for each strain rate experiment is shown in Table 2.6.

2.7 High Speed Infrared Camera Measurements

The Telops FAST-IR infrared camera [36] used in the experiments records the flux of the photons emitted from the surface of each test specimen. Each individual pixel on the camera sensor has its own radiometric calibration which allows for automatic compensation of ambient temperature drift and instrument self-radiance while implicitly controlling the exposure times and frame rate. The InSb sensor in the camera is sensitive to the 3-5 μm spectral range and consists of 320x256 pixels at a 30 μm pitch. The analog data collected by the camera sensor is digitized information in either photon counts, in-band radiance values $\left(\frac{W}{m^2-sr}\right)$, or radiometric temperatures (^{o}C). When making in-band radiance or radiometric calculations the computer software HYP-IR assumes that the target of the camera is a black body and its emissivity is 1. However, the book values of emissivity for Ti-6Al-4V, Aluminum 2024, and Inconel 718 can range from 0.03 to 0.8 depending on the level of polish or oxidation of the surface[37]–[39]. Because of this discrepancy, steps must be implemented to achieve accurate surface temperature measurements during each test. In previous works researchers applied a coating such as paint or soot to the surface to increase the emissivity and insure a uniform finish [14], [15], [22]. However, during high strain rate tests the added surface layer acts as an inhibitor to heat transfer and provides artificially low temperature readings. To calibrate

the samples used in these experiments thermocouples are attached to the surface of a sample of each material while the temperature is increased incrementally using a hot plate as shown in Figure 2.8.

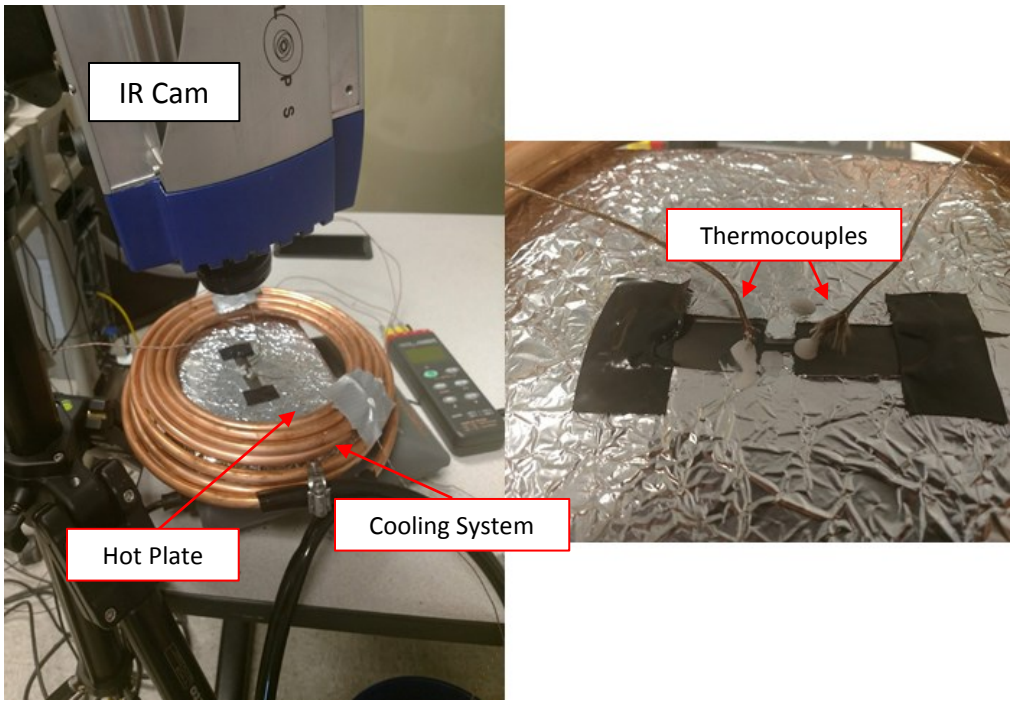

Figure 2.8 Hot Plate Calibration Setup

Raising the temperature in increments allows the temperature across the specimen to become uniform and provide accurate average in-band radiance values. Deformed specimens are known to have an increase in emissivity due to an increase in surface roughness [14]. However, in these calibrations the maximum temperature difference between the deformed gage section and a point in the transition zone between the tab and gage section is only 2.25% at a maximum temperature of 200ºC. The resulting temperatures along the centerline of a sample during a normal calibration is shown in Figure 2.9.

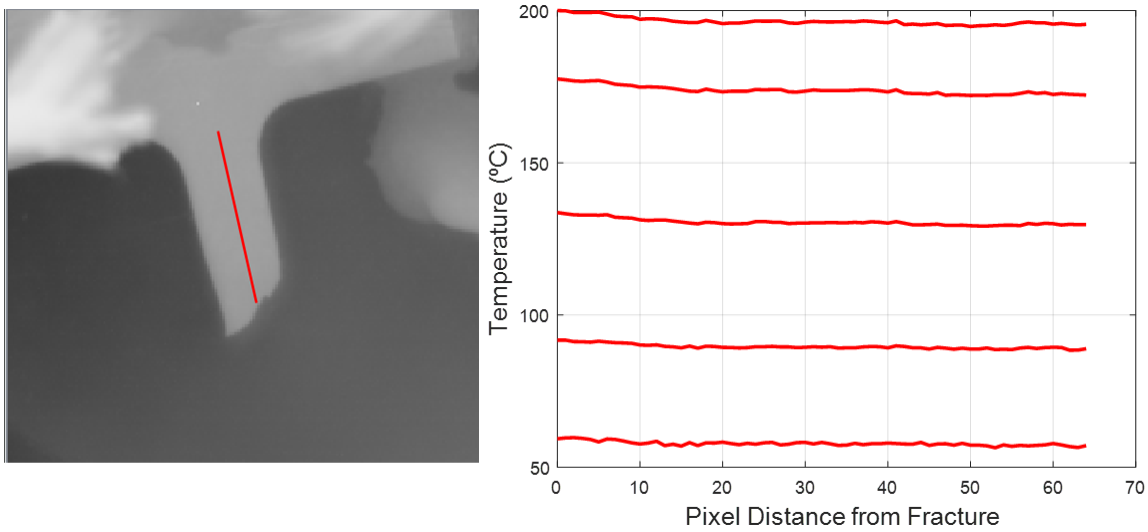

Figure 2.9 (left) Location of Centerline in Infrared Image (right) Temperature Along Centerline during Calibration

A blackout curtain is placed over the setup to reduce noise caused by outside sources of radiation. The surface of the hot plate surrounding the specimen is covered in wrinkled aluminum foil that reduces noise by reflecting ~99.97% of incident radiation and emitting ~0.03% of the radiation due to an increase in temperature. The infrared camera records the in-band radiance values of the entire gage section surface and is operated using the same parameters as the tension tests listed in Table 2.8. Average values over several pixels in the gage section are used to create a best fit power law calibration curve. The equation of each curve is given in equation 2-11. Using this curve the measured in-band radiance values can be converted into surface temperatures for each test. The calibration curves produced by the calibration method are shown in Figure 2.10-Figure 2.12 along with the raw calibration data.

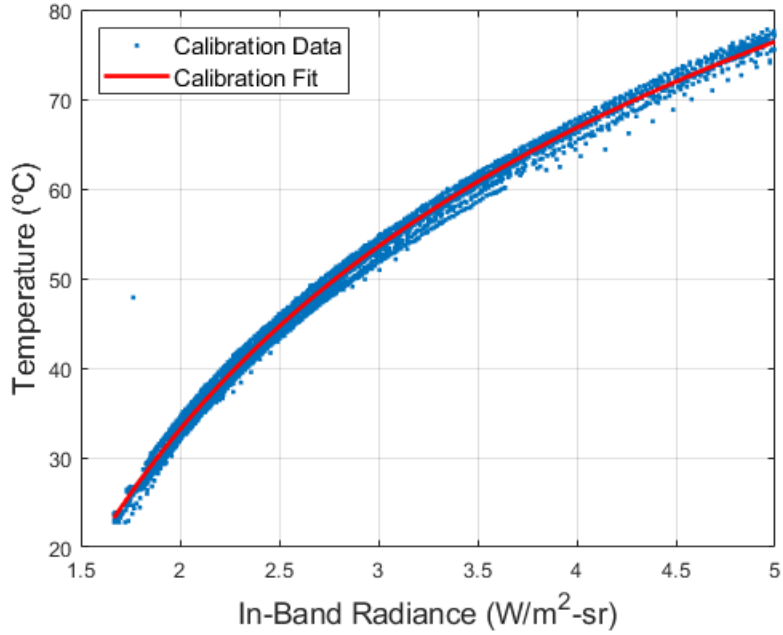

Figure 2.10 In-Band Radiance to Temperature Calibration Curve for Aluminum 2024

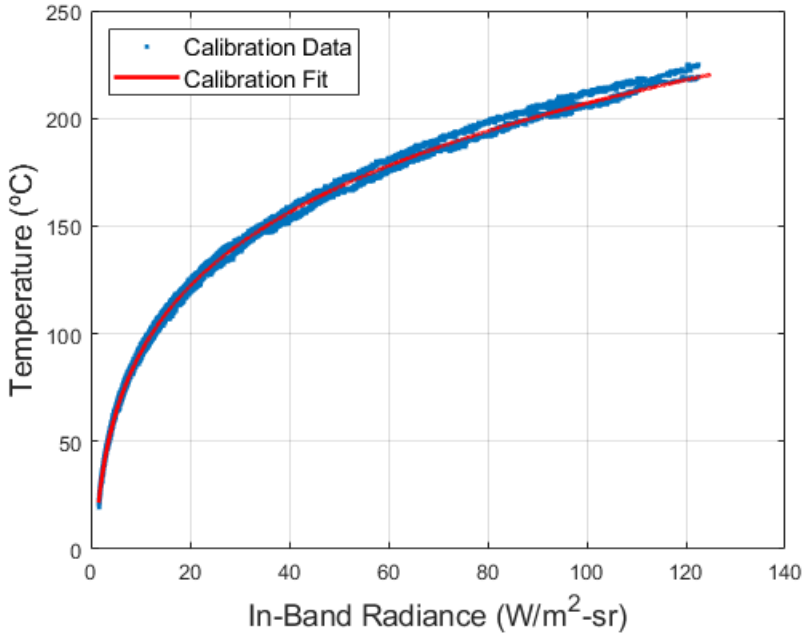

Figure 2.11 In-Band Radiance to Temperature Calibration Curve for Ti-6Al-4V

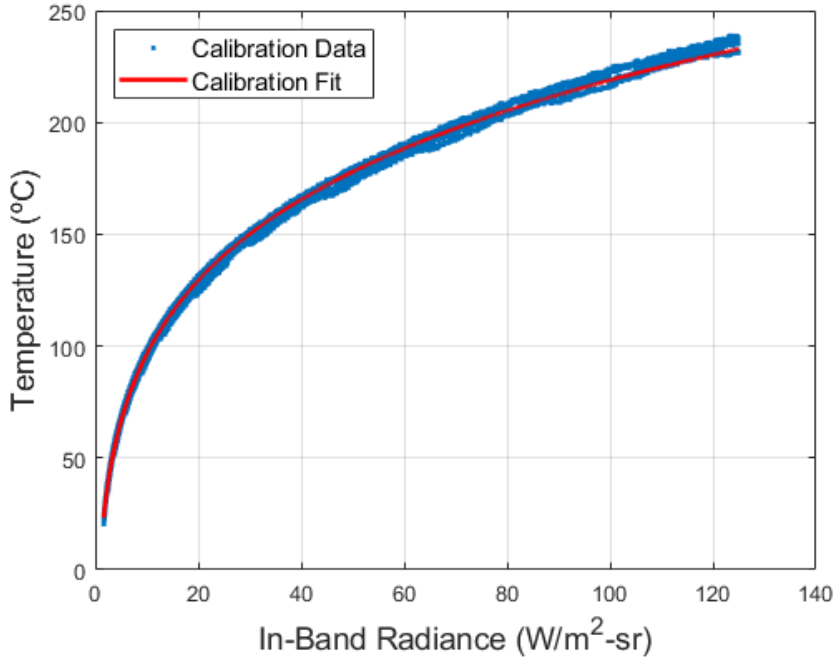

Figure 2.12 In-Band Radiance to Temperature Calibration Curve for Aluminum 2024

$$T = a * IBR^b + c \qquad \textbf{(2-11)}$$

Table 2.7 Coefficients for Calibration Curves for Each Material

Material	Fit Coefficients		
	a	b	c
Aluminum 2024-T351	-246.5	-0.2572	239.4
Ti-6Al-4V	223.3	0.139	-0.2165
Inconel 718	246.2	0.135	-239.5

In-band radiance values are measured on the surface of each specimen during the tension tests using the same Telops FAST-IR camera. The camera is placed 0.12 to 0.5 m from the specimen in each test. The IR camera records images at the same frame rate as the visual cameras in the low rate tests and at a frame rate that is a multiple of the visual cameras during the higher strain rate tests. To increase the frame rate of the camera for the higher rate tests the resolution of the image and the exposure time of the camera must

be greatly reduced. Reducing the resolution increases the average temperature measurement area for each individual infrared sensor pixel and increases the number of DIC measurements contained within each infrared pixel measurement. Shorter exposure times lead to noisier data at temperatures closer to room temperature while longer exposure times can oversaturate the sensor during the measurement period resulting in tests where the maximum temperature cannot be recorded. The frame rates, resolutions, and exposure times used in each test are reported in Table 2.8.

Table 2.8 Infrared Camera Optics for Each Strain Rate Test

Strain Rate (s^{-1})	Pixel Resolution	Exposure Time (μs)	Frame Rate (fps)
1 E-4	256x256	50-100	0.2
0.1		20-50	200
1		10	2,000
500	64x20	10	20,000
2000	64x16	5	62,500
6000	64x4	5	90,000

2.8 Measurement Synchronization Techniques

To evaluate the β_{int} of each material the DIC and IR camera measurements must be synced with the force data from the MTS load frame and split-Hopkinson bars. Accurate results depend on successfully integrating the simultaneous force measurements from the loading devices with the DIC strain measurements and IR temperature measurements. Special consideration has been taken to resolve several issues in aligning both the temporal and spatial coordinates of all measurements.

In each tension test the measurements are synchronized by triggering both cameras with a signal originating from the moment when loading is initiated. In the low

strain rate tests (1E-4 to 1 s^{-1}) the MTS controller runs a program that sends a 3.0V digital step output to a dual-channel Keysight 33,500 series waveform generator 0.05 seconds before the ramp displacement program is initiated. After receiving the digital output the waveform generator sends two 0.2-2000 Hz, 5.0 Vpp Square wave and 3.3 Vpp square wave signals to initiate image capture in both the DIC system andIR camera respectively. An output pulse is generated by each camera that indicates the exposure of each individual image and the length of the pulse designates the exposure time. The digital output from the frame, the trigger pulses to the IR camera, and the output exposure pulses from each of the cameras are recorded on an image sync oscilloscope to synchronize the cameras and load frame on a co mmon time base. A schematic of the timing structure is shown in Figure 2.13.

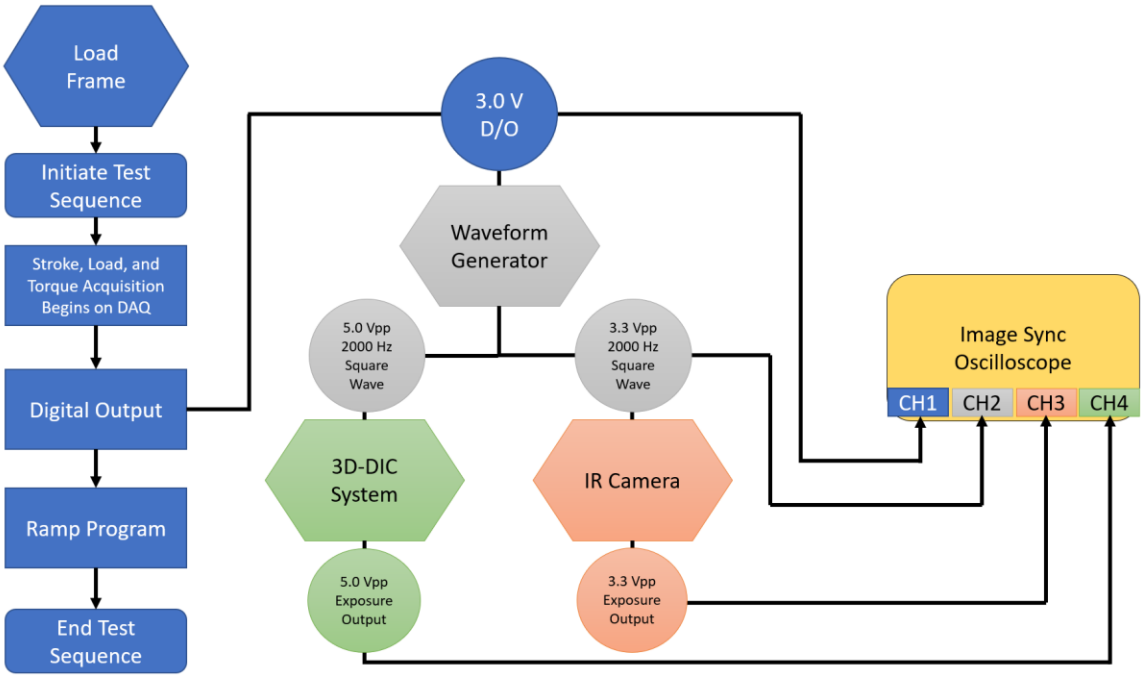

Figure 2.13 Visual Representation of the Loading Sequence and Output Timing Signals for the Low Strain Rate Tests

The signals collected on the image sync oscilloscope from the first 1.8 ms of a 1 s^{-1} strain rate test on aluminum 2024-T351 are shown in Figure 2.14. At time 0, the digital output from the load frame initiates an IR trigger from the waveform generator and an IR exposure pulse from the IR camera lasting 80 µs. During each IR exposure the active pixels on the IR sensor collect photons emanating from the surface of the specimen and the software records an average in-band radiance value for each pixel over that period. To account for this phenomenon, the time stamp given to each IR image is the midpoint of its exposure. Due to the shorter exposure time of the visual cameras, the DIC time stamps are given to the initial rise of the DIC exposure signal. The shared time stamps determined from the exposure signals for both the IR and DIC images are shown in Figure 2.14.

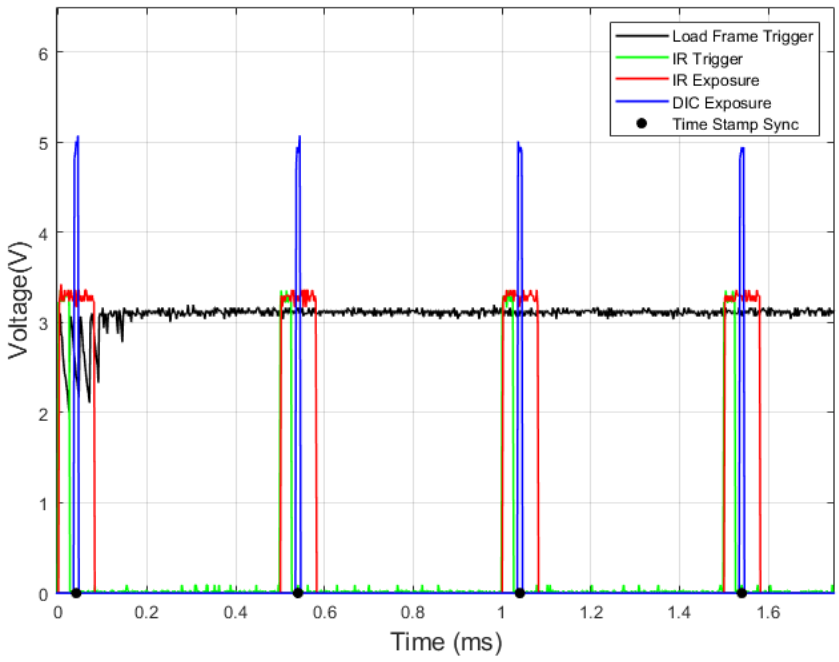

Figure 2.14 Timing Signals Collected on the Image Sync Oscilloscope during a 1 s^{-1} Strain Rate Test on Aluminum 2024-T351

Figure 2.15 overlays the load frame LVDT stroke measurement from the load frame with the exposure signals from the image sync oscilloscope during the first 100ms of the tension test. The stroke and load for each of the IR and DIC images is found by interpolating the data from the load frame at the previously determined time stamps. Typical synchronized data of the load and the temperature and failure strain measured at a failure point is shown in Figure 2.16. Each dot in the graph represents 20 data points synchronized in time.

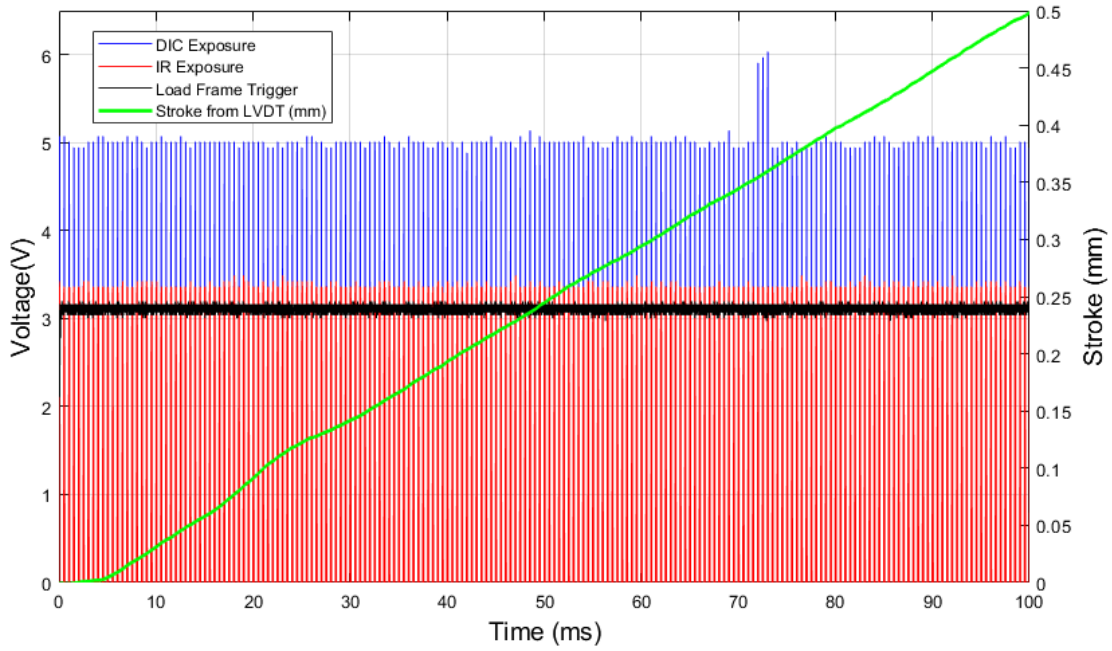

Figure 2.15 Signals from the Timing Oscilloscope and Load Frame on a Shared Time Base

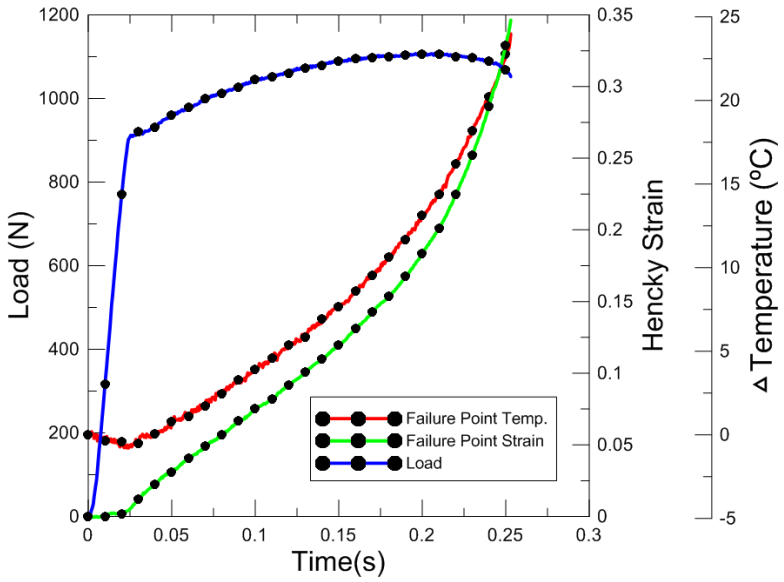

Figure 2.16 Combined Load, Temperature, and Strain Data from a 1 s^{-1} Strain Rate test on Aluminum 2024-T351

In high rate tension tests (500-6000 s^{-1}) the oscilloscope recording the force in the strain gages on the SHB is triggered when the force in Gage A reaches 100N. When the oscilloscope is triggered the voltage outputs from each Wheatstone bridges on the bar are recorded and an output signal is sent to the waveform generator. The waveform generator then sends trigger signals to both the IR camera and Shimadzu HPV-X2 to initiate recording. The outputs from the cameras and waveform generator collected on the image sync oscilloscope are the same as in the low rate tests. The Shimadzu HPV-X2 has a limited memory and can only take 128 images for a single recording event so the image capture is delayed by 350µs, insuring the tensile wave has reached the specimen. Because the cameras are aligned in space with the specimen, the tensile waves measured by the gages in the transmitted bar can be shifted to match the strain and temperature measurements from the cameras by the time shift parameter t_c, where $t_c = \frac{L_C}{c_b}$ (2-11), L_c

is the distance from the specimen to gage on the transmitted bar and c_b is the wave speed of the bar. Once shifted in time, the images from each camera align with the measured force in both gages of the transmitted bar as shown in Figure 2.17. The time stamps for the IR and DIC cameras are determined in the same manner as the low strain rate tests. However, in the higher strain rate tests the IR camera has a significantly lower frame rate than the DIC camera and an exposure that comprises several individual DIC images. A typical timing sequence of the DIC and IR images is shown in Figure 2.18. To account for the discrepancy in time between the IR time stamps and the DIC time stamps, the synchronized DIC and IR measurements are taken at the DIC image closest to the midpoint of each IR exposure. The result of this synchronization is shown in Figure 2.19.

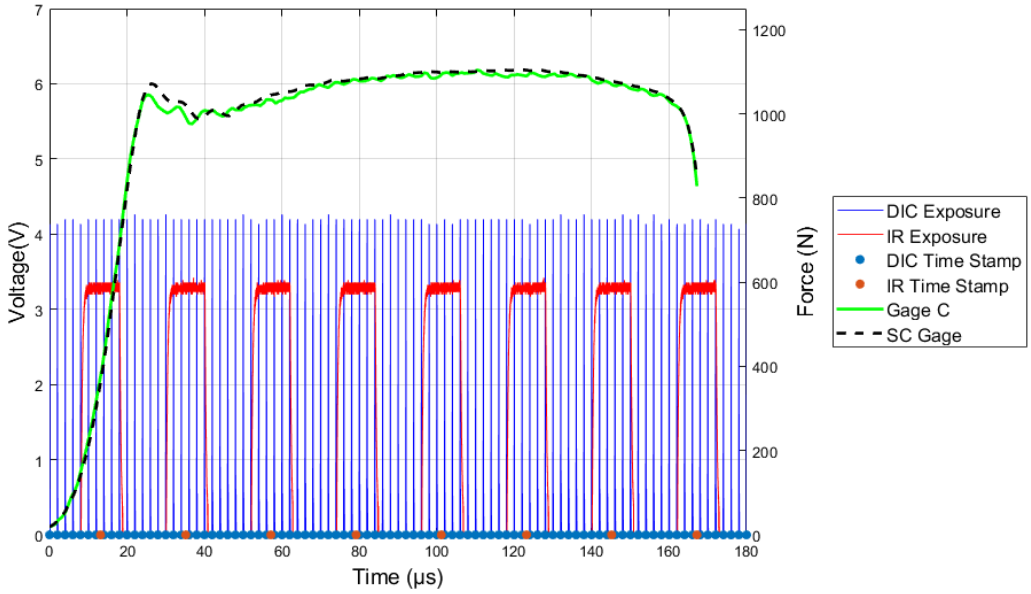

Figure 2.17 Resulting Transmitted Waves with Infrared and DIC Exposures after Time Synchronization

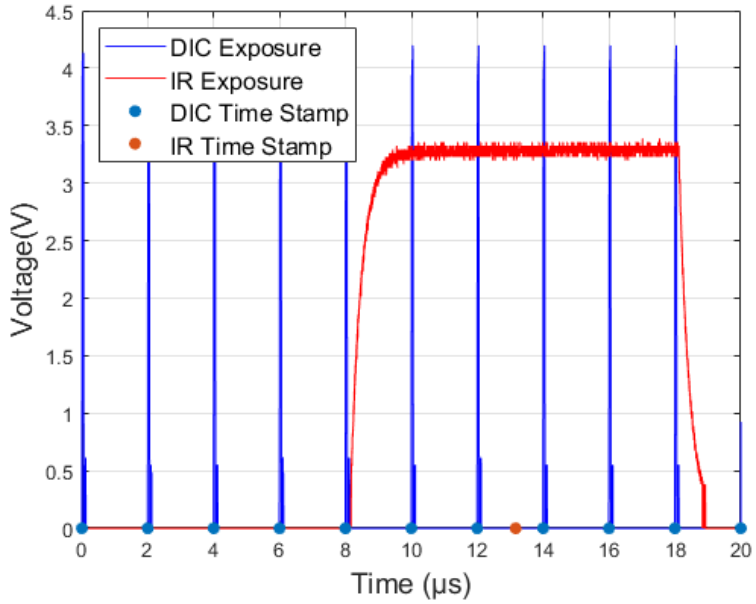

Figure 2.18 Characteristic Timing Sequence for Infrared and DIC Measurements During a 2000 s^{-1} Strain Rate Test on Aluminum 2024-T351

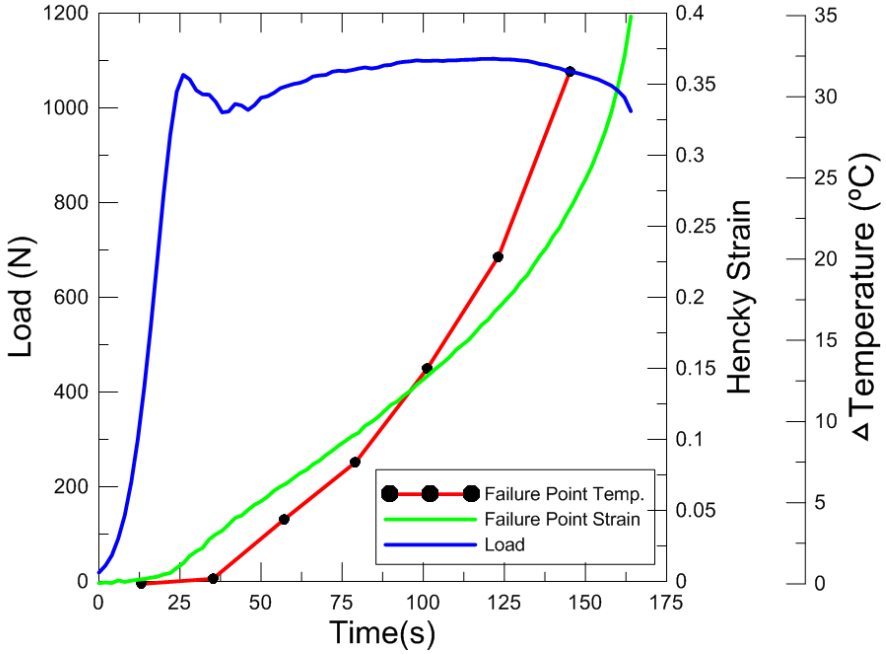

Figure 2.19 Combined Load, Temperature, and Strain Data from a 2000 s^{-1} Strain Rate Test on Aluminum 2024-T351

To determine the β_{int} at each DIC data point on the surface of the specimen, the temperature, true plastic strain, and true plastic stress of the specimen at that point in space must be known. During each test the DIC cameras are placed on one side of the tension specimen and the IR camera is placed on the opposite side as shown in Figure 2.2, Figure 2.4, and Figure 2.6. The IR camera is slightly offset from perpendicular to the specimen because the sensor of the IR camera is kept at -191.41ºC and the camera can "see" the temperature of the sensor due to irradiance on the specimen. It is assumed that the temperature and deformation through the thickness of the specimen are uniform due to the thin geometry of each sample. The temperature and deformation fields calculated from the IR and DIC measurements are aligned by recording both visible and infrared images of a glass DIC alignment grid as shown in Figure 2.20. The resulting images after rotating the IR image 180º are shown in Figure 2.21. In each image the center of the calibration circles are determined using a Hough transform in MATLAB. The coordinates of the IR calibration circle centers are then transformed using a 2D projective transformation to map the IR image on the DIC image. Because the resolutions of the images are different the transform matrix scales, skews, rotates and translates the IR coordinates to match the DIC coordinates. The result of the transformation along with the transformed IR coordinates are shown in Figure 2.22.

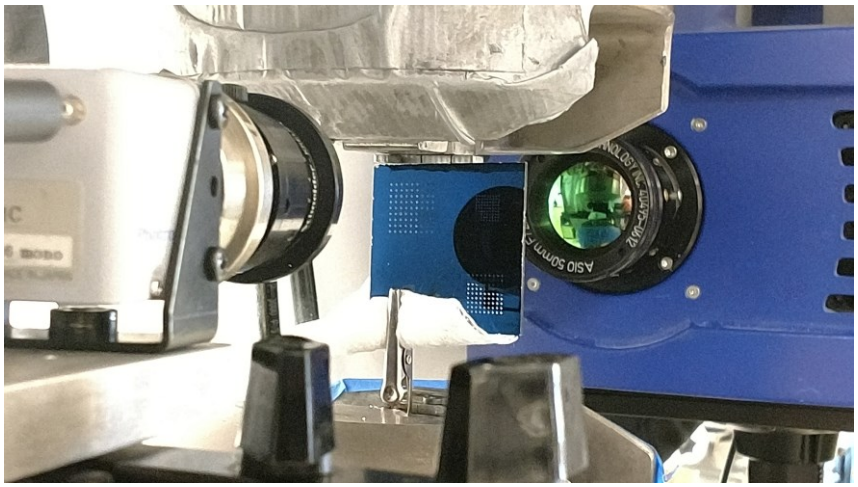

Figure 2.20 Image Capture for Alignment Procedure of DIC and Infrared Measurements

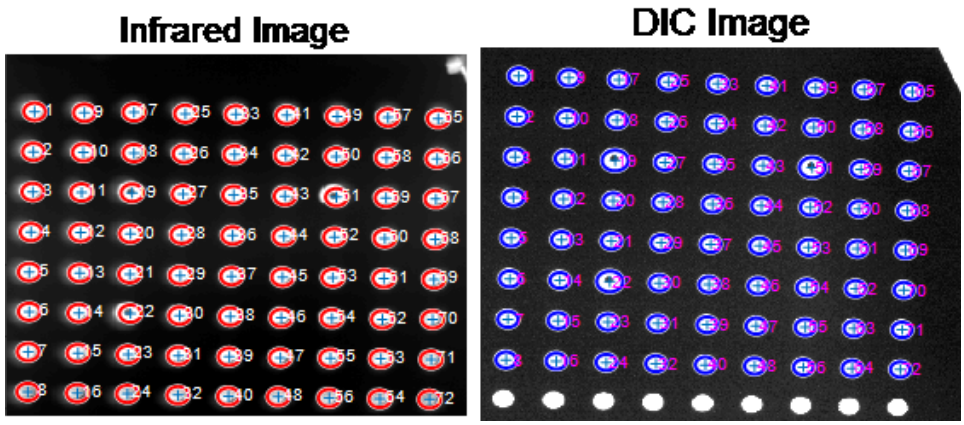

Figure 2.21 IR and DIC Images Captured during Alignment Procedure

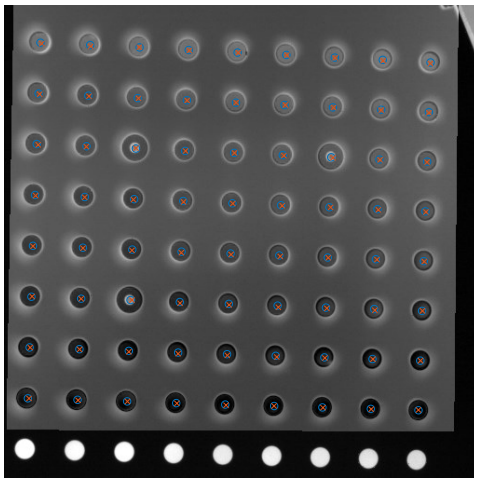

Figure 2.22 Overlay of the IR Image and Coordinates on the DIC Image following the Projective Transformation Procedure

The DIC measurements determined at each individual pixel of the DIC image are tracked throughout each tension test using Lagrangian coordinates while the IR temperature measurements are fixed in space using Eulerian coordinates. As each tension test is carried out the individual DIC measurements pass through multiple IR pixels as shown in Figure 2.23. The temperature at each of these DIC measurement points is then determined using a 2D interpolation for the synchronized DIC and IR images and is completed in MATLAB.

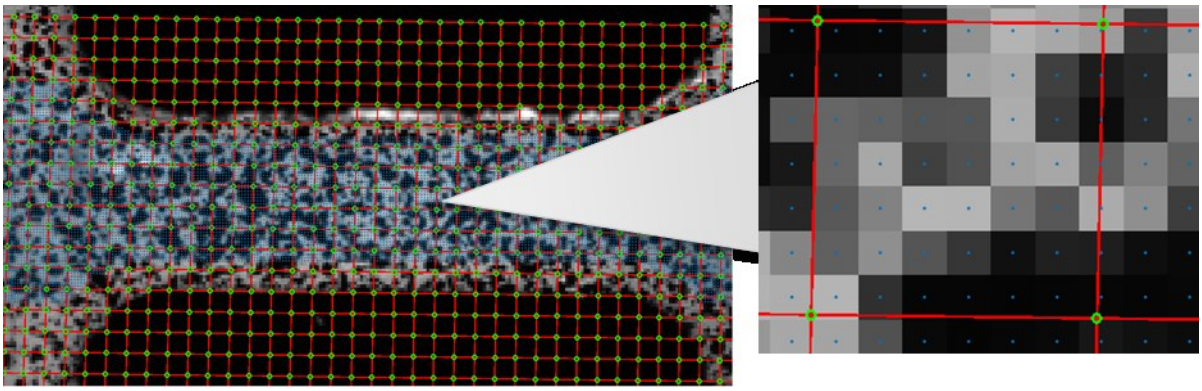

Figure 2.23 Overlay of IR Pixel Grid on DIC Measurement Locations for a Typical Tension Test

The strain measured with DIC at each point is the axial Hencky strain which is considered as the true strain at each point. The true strain is converted to equivalent axial engineering strain by equation 2-13:

$$\epsilon_e = \exp(\epsilon_H) - 1 \qquad (2\text{-}13)$$

where ϵ_H is the axial Hencky strain.

The true stress is determined at each DIC point by the following:

$$\sigma_t = \sigma_e(1 + \epsilon_e) \qquad (2\text{-}14)$$

where σ_e is the engineering stress determined in equations 2-1, 2-6, and 2-10, and ϵ_e is the engineering strain at each point. The true plastic strain at each individual point is determined by subtracting the elastic strain ($\epsilon_{elastic}$) from the total engineering strain and converting back to true strain as shown in equation 2-15.

$$\epsilon_p = \ln(1 + (\epsilon_e - \epsilon_{elastic})) \qquad (2\text{-}15)$$

The elastic strain is determined for each material using the 2% offset method as show in Figure 2.24.

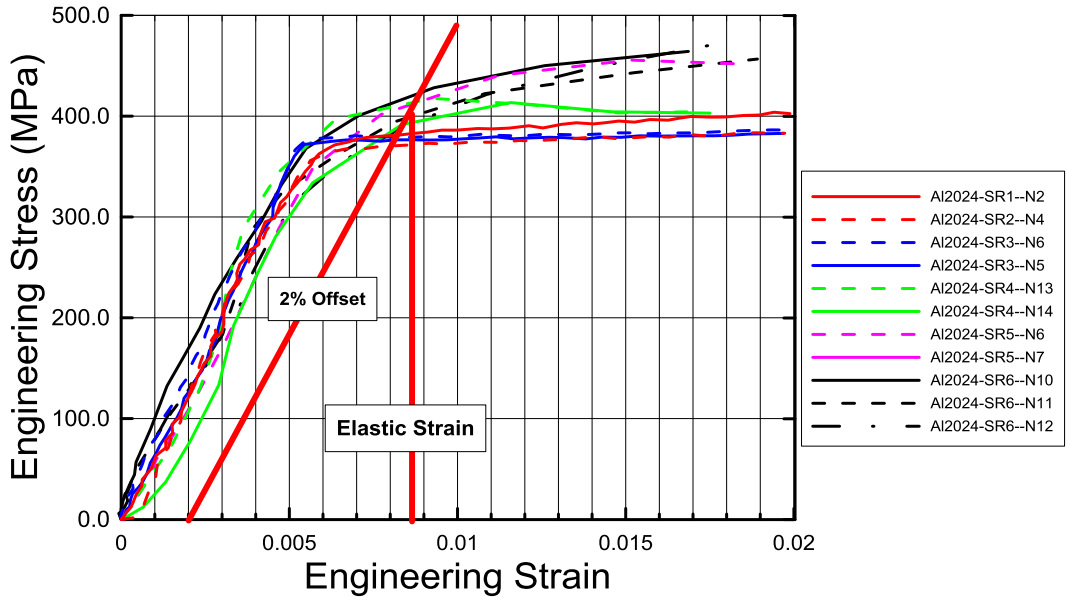

Figure 2.24 2% Offset Method for Determining Yield Stress in Aluminum 2024-T351

The $\beta_{int}(t)$ is calculated using the temperature $T(t)$, true plastic stress $\sigma_t(t)$, and true plastic strain $\epsilon_p(t)$ determined for each DIC measurement point in time by the following equation:

$$\beta_{int}(t) = \frac{\rho c_p (T(t) - T_0)}{\int_0^t \sigma_t(t)\epsilon_p(t)} \qquad (2\text{-}16)$$

Chapter 3 Measurement of the Taylor-Quinney Coefficient Experimental Results

3.1 Experimental Results from Ti-6Al-4V

Representative experimental data from the tension experiments on Ti-6Al-4V is shown in Figure 3.1. The yield stress increases from approximately 900MPa at the lowest strain rate to 1350MPa at a strain rate of 6000 s^{-1}. The flow stress increases with increasing strain rate while the failure strains decrease from 19% to 16-17% for strain rates above 1 s^{-1}. Strain hardening behavior is more evident in the tests at and below a strain rate of 1 s^{-1} when compared to the higher strain rate tests.

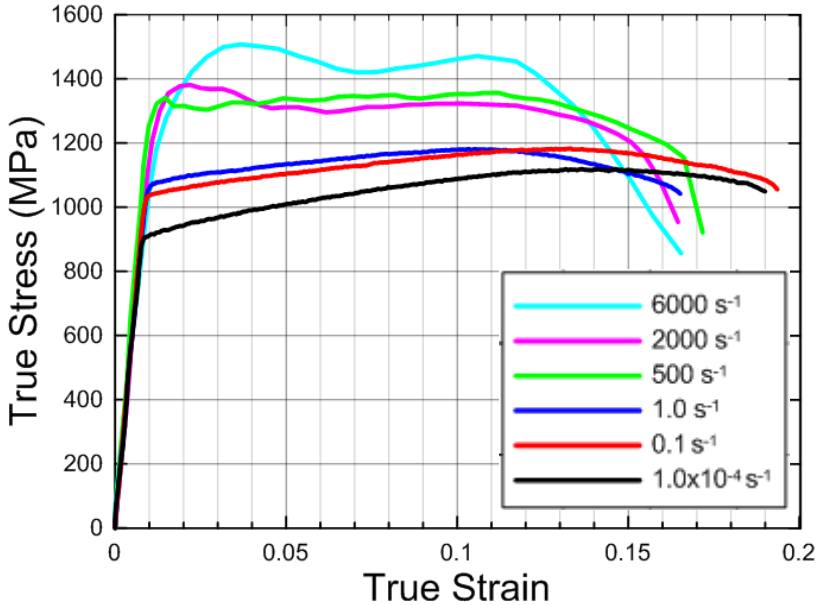

Figure 3.1 Stress vs. Strain Data from Tension Tests on Ti-6Al-4V at Various Strain Rates

The histories of the Hencky strain and temperature for the point of maximum strain at failure with the average axial strain are shown in Figure 3.2 (a)-(f), In each test the strain at the failure point rises at the same rate of the extensometer strain until a strain of 0.03-0.05 is reached and necking occurs. The measured temperature change in each test is close to 0 before necking is initiated. Significant changes in temperature are measured in each test above a strain rate of 1E-4 s^{-1} where the test is nearly isothermal. For tests at strain rates of 500-6000 s^{-1} the time stamps where simultaneous temperature and deformation measurements were recorded are designated by a red dot in the temperature curve. In each test the maximum strain measured at the point of failure was 2-3x's the strain measured by the extensometer across the gage section of the specimen.

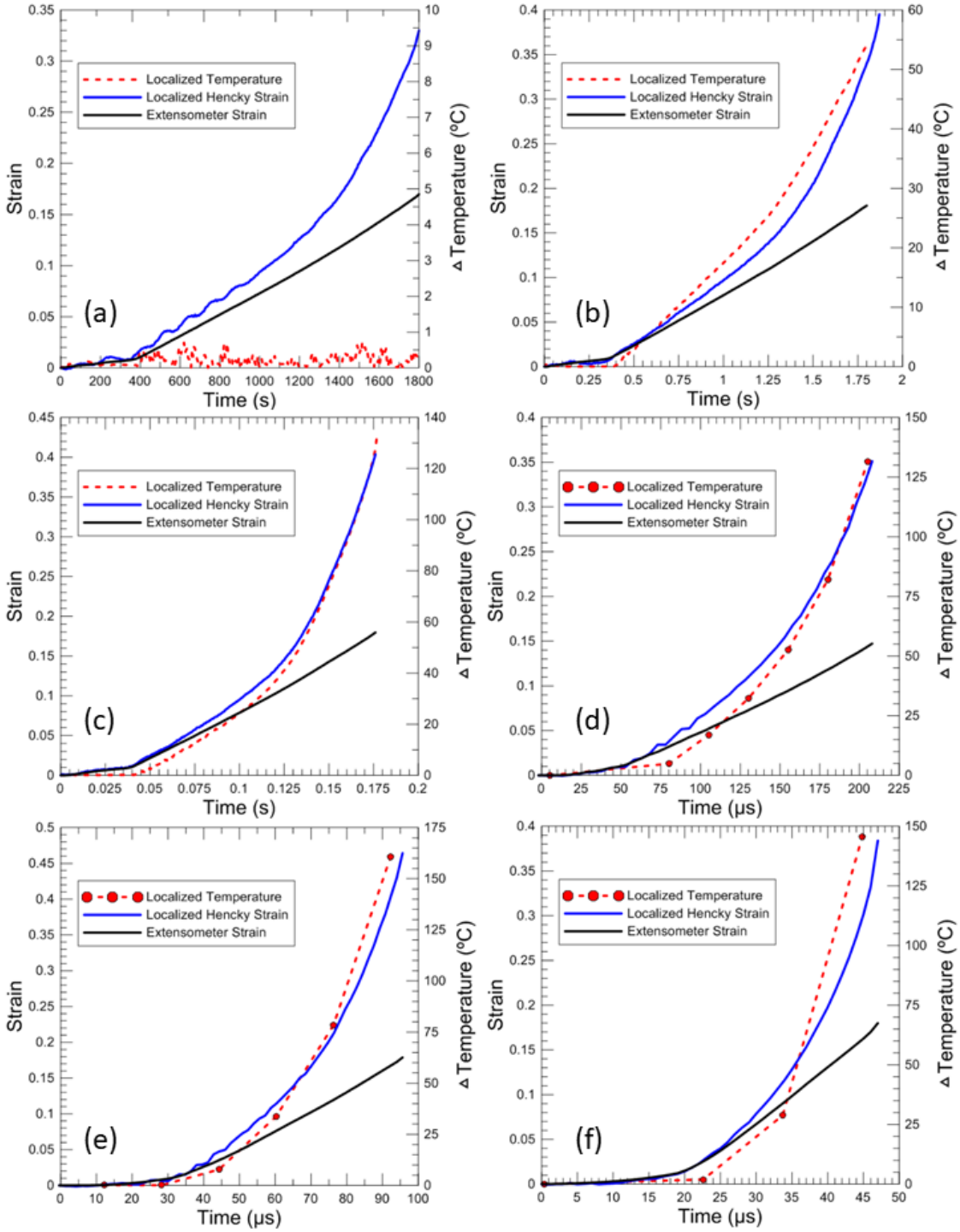

Figure 3.2. Strain and Temperature History for the Failure Point during Tension Tests of Ti-6Al-4V at Strain Rates of (a) 1E-4 s^{-1} (b) 0.1 s^{-1} (c) 1 s^{-1} (d) 500 s^{-1} (e) 2000 s^{-1} (f) 6000 s^{-1}

Figure 3.3 displays the temperature versus Hencky strain the data point located at the point of failure during each tension test. The curves presented represent the maximum temperature change and strain that could be measured simultaneously, thus the localized strains measured at the higher strain rates are underrepresented due to the limitations of the infrared camera speed. At a nominal strain of 0.3 the change in temperature increased from 0 at a strain rate of 1E-4 s^{-1} to 155ºC at a stra in rate of 6000 s^{-1}. The change in strain rate shows the change in the thermodynamic conditions from isothermal at a strain rate of 1E-4 s^{-1} to nearly adiabatic in strain rates at 1 s^{-1} and above.

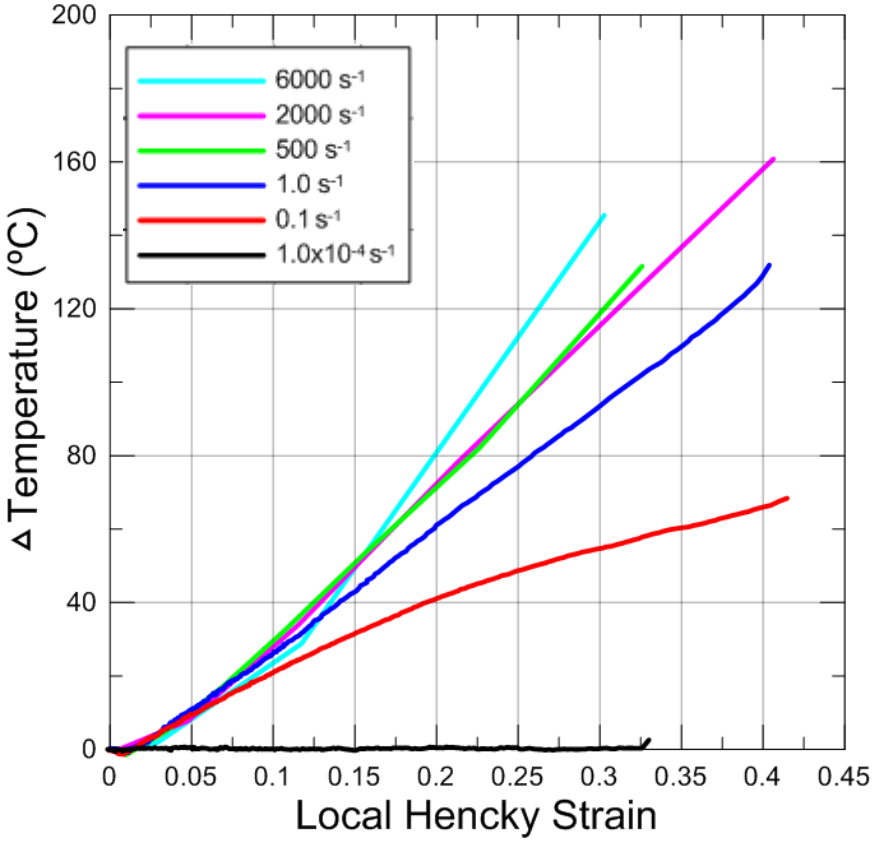

Figure 3.3. Change in Temperature versus Local Axial Hencky Strain for the Data Points Located at the Point of Failure for each Strain Rate Test

Full-field measurements of the plastic strain, temperature, and Taylor-Quinney coefficient are displayed for a tension test at a strain rate of 1 s^{-1} in Figure 3.4. Images from 42-57ms of the test show that plastic strain levels below 0.03 and below lead to very small changes in temperature and a small Taylor-Quinney coefficient. As the necking region begins to develop from 74.5-160.2ms a band of constant β is measured as 0.5-0.6 in the same region. During this time the plastic strain measured outside the necking region remains at 0.05-0.1, however, the temperature continues rise due to the conduction of heat away from the localization region. This rise in temperature without cooresponding plastic work leads to an artifical β being measured as 0.7-0.9 outside the localization.

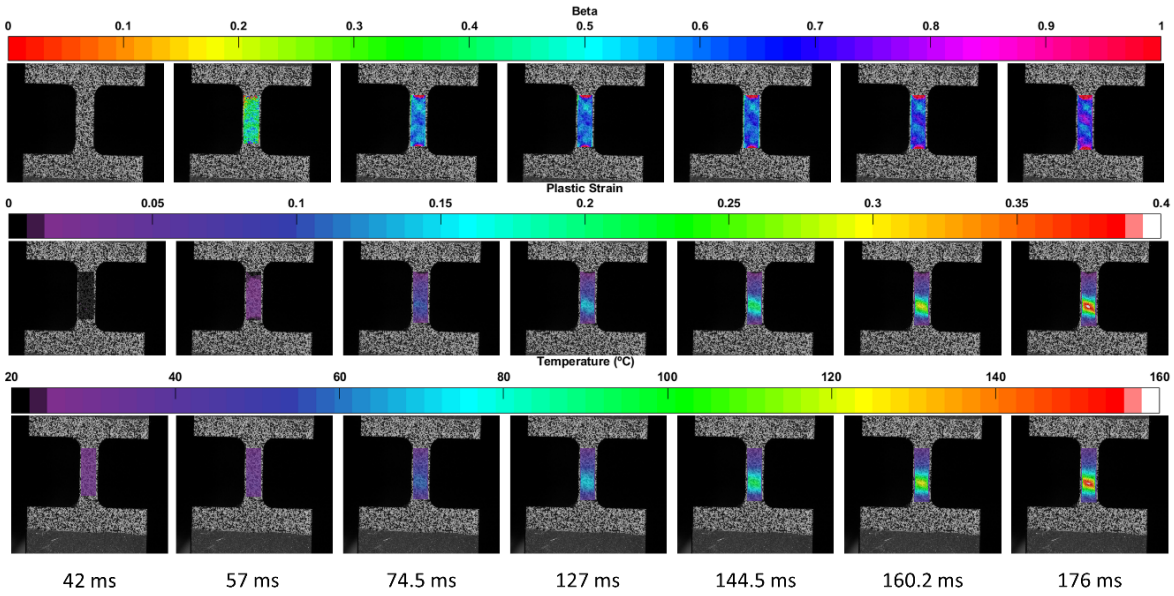

Figure 3.4. Full-Field Taylor-Quinney, Plastic Strain, and Temperature Measurements for a Ti-6Al-4V Tension Test at 1 s^{-1}

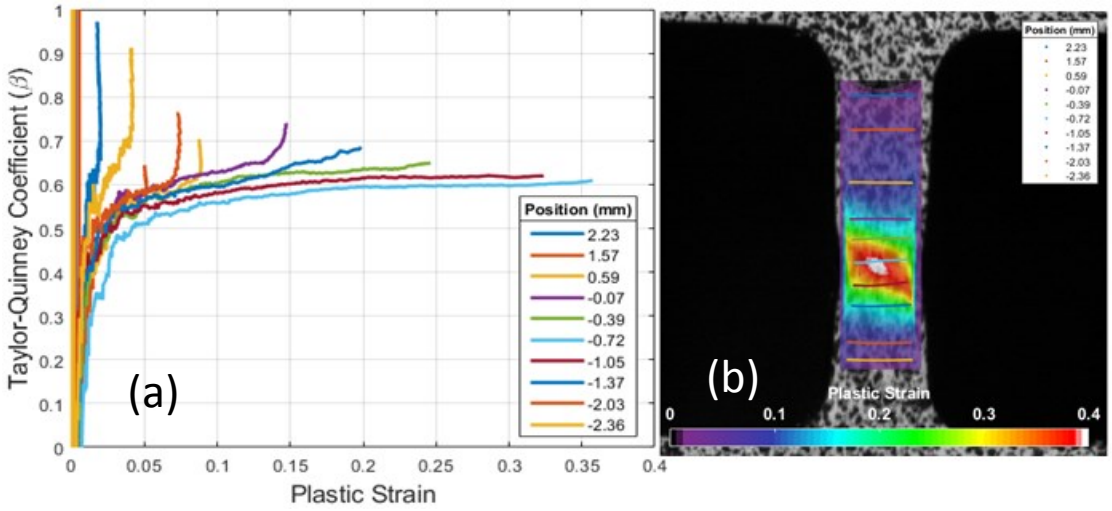

Figure 3.5. (a) Average Taylor-Quinney Coefficient of Cross-Sectional Lines on Gage Section (b) Location of Cross-Sectional Lines at Failure

The average Taylor-Quinney coefficient calculated from multiple data points across the gage section of the specimen are shown in Figure 3.5. The lines located nearest the strain localization each have maximum strains between 0.25-0.35 and an average β between 0.6-0.65. Lines located between 0.65 to 2.9 mm away from the maximum localization strain each have a β that increase from 0.6 up to 0.95 due to the heat conduction away from the localization. The influence of the heat conduction can also be seen in Figure 3.6 and Figure 3.7. In Figure 3.6 the temperature increases along the entire gage length during the entire test although the plastic strain outside of the localization region stopped increasing after 160.5ms of the test. In Figure 3.7 the β remains relatively constant in localization region from -1.25 mm to -0.5 mm over the test period from 127ms to 176ms but is increasing outside of this region. These results show that the 1 s^{-1} test is not adiabatic and thus the conditions for equation 1.1 are not satisfied. However, the material models we are developing can use an "effective β" which will determine the temperature rise in the material at different strain rates assuming the tests

are adiabatic. This will allow for the maximum temperatures to be recreated in the material which are important for determining failure caused by thermal softening at high strain rates.

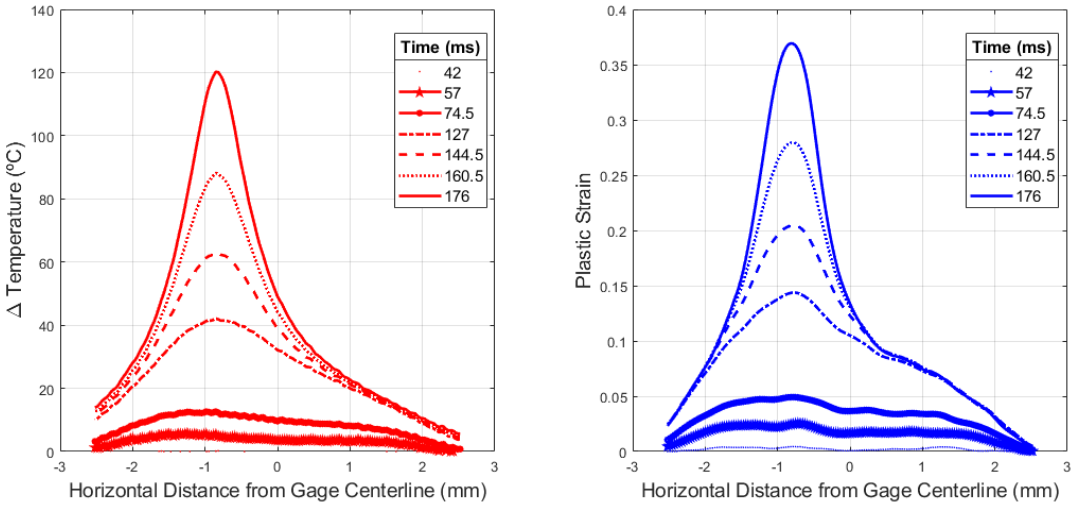

Figure 3.6. Temperature and Plastic Strain along the Gage Section for a Ti-6Al-4V Tension Test at 1 s^{-1}

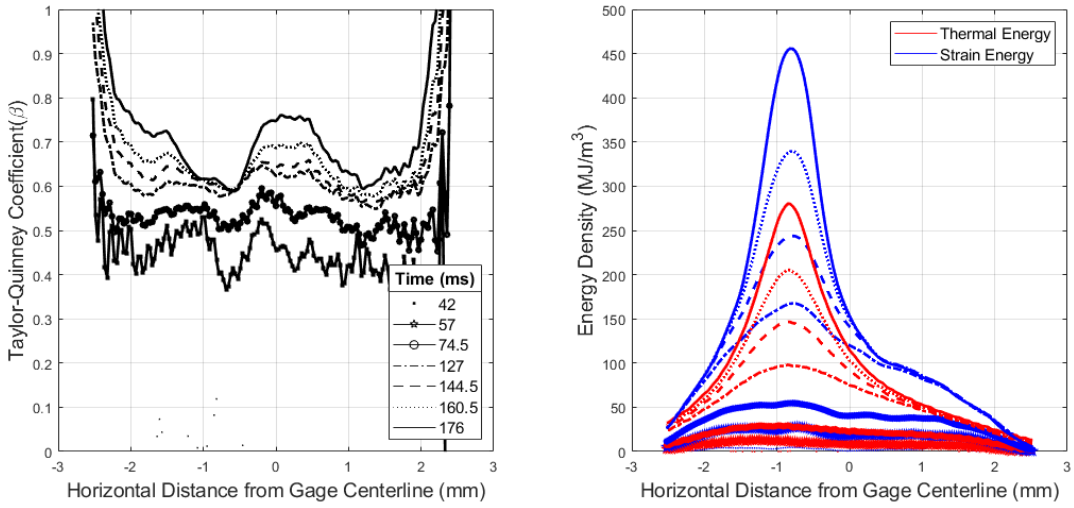

Figure 3.7. Taylor-Quinney Coefficient and Energy Density Comparison along the Gage Section for a Ti-6Al-4V Tension Test at 1 s^{-1}

The effective β is measured in Figure 3.8 as an average of the lines of data across the gage section only in the localization region. A single moving average is then

calculated using these points in Figure 3.9. The β increases from 0 to 0.6 for a plastic strain of 0 to 0.1 and then remains constant near a value of 0.6 up to a plastic strain of 0.35.

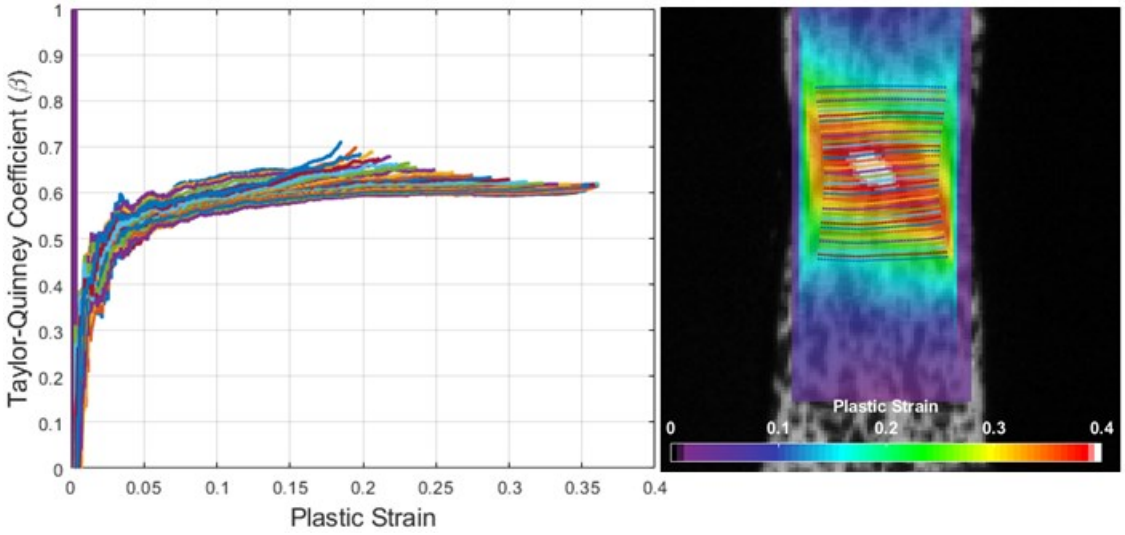

Figure 3.8. Calculation of the Taylor-Quinney Coefficient for each Line of Data in the Localization Region for a Ti-6Al-4V Tension Test at 1 s^{-1}

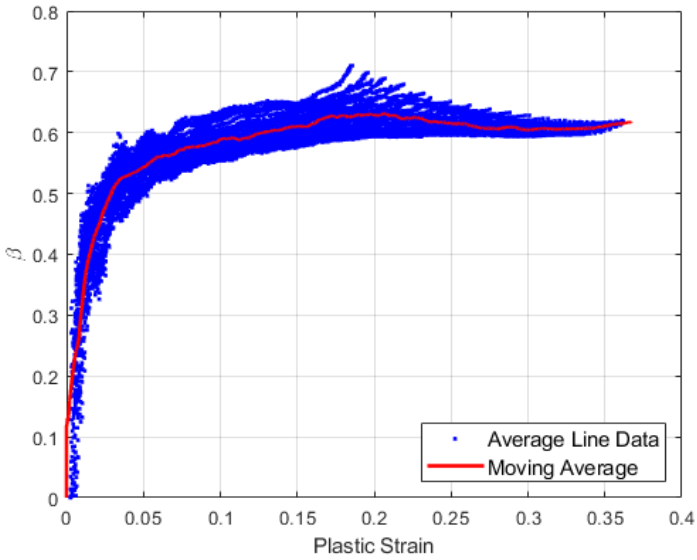

Figure 3.9 Calculation of the Moving Average for each Line of Data in the Localization Region for a Ti-6Al-4V Tension Test at 1 s^{-1}

Images of the full-field Taylor-Quinney coefficient, plastic strain, and temperature measurements for the tension tests at 500, 2000, and 6000 s^{-1} are displayed in Figure 3.10-Figure 3.12. The dependence of the β on plastic strain is shown in each of the figures as β increases from 0.3-0.6 as the plastic strain increases from 0.05-0.1 across the entire gage section. In these tests the temperatures increase only with a corresponding increase in plastic strain and it can be assumed these tests are nearly adiabatic.

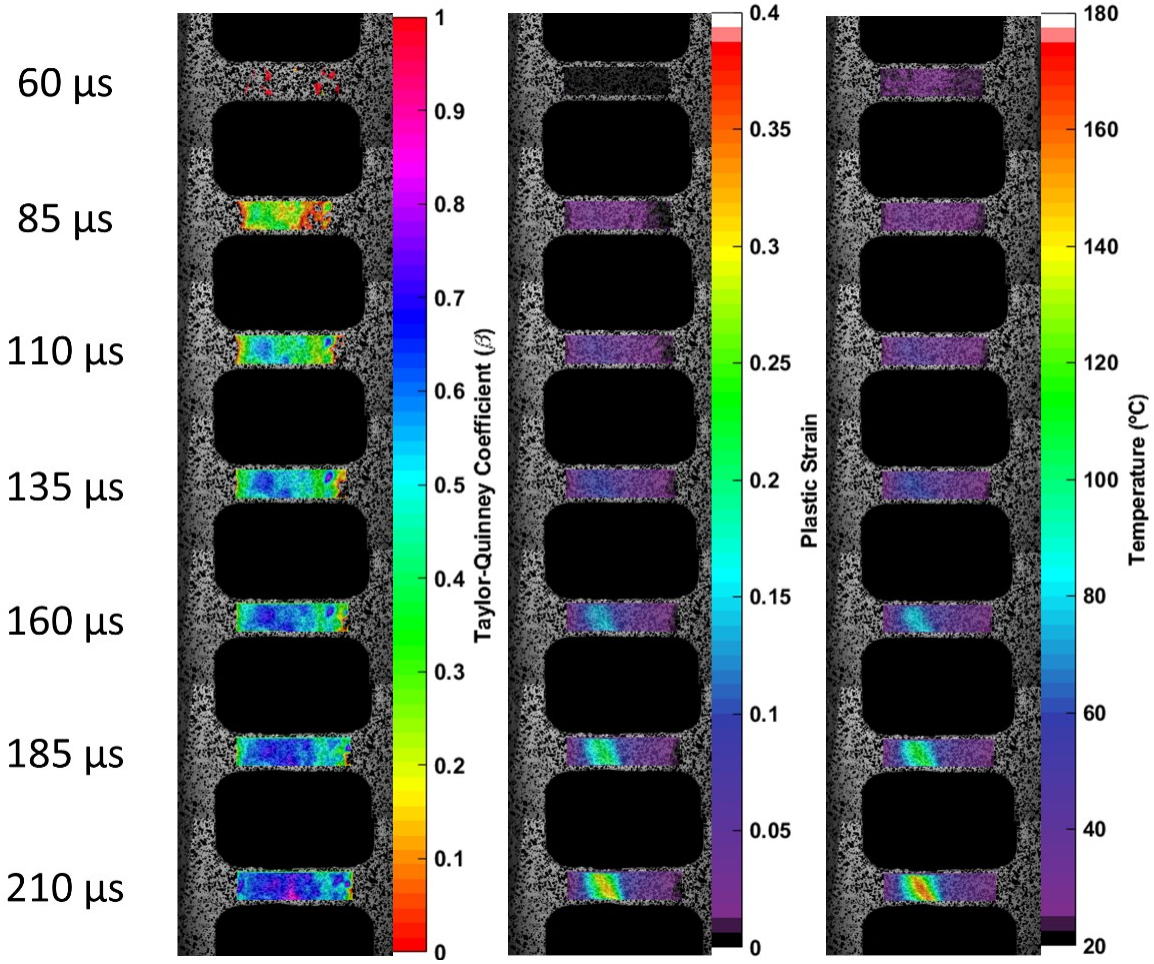

Figure 3.10 Full-Field Taylor-Quinney, Plastic Strain, and Temperature Measurements for a Ti-6Al-4V Tension Test at 500 s^{-1}

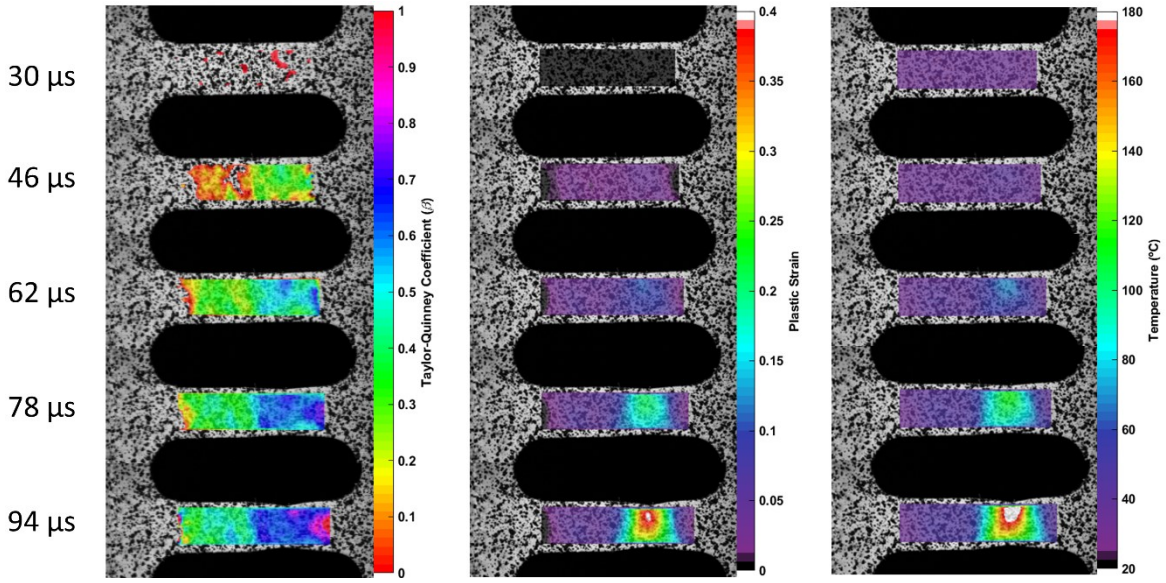

Figure 3.11 Full-Field Taylor-Quinney, Plastic Strain, and Temperature Measurements for a Ti-6Al-4V Tension Test at 2000 s^{-1}

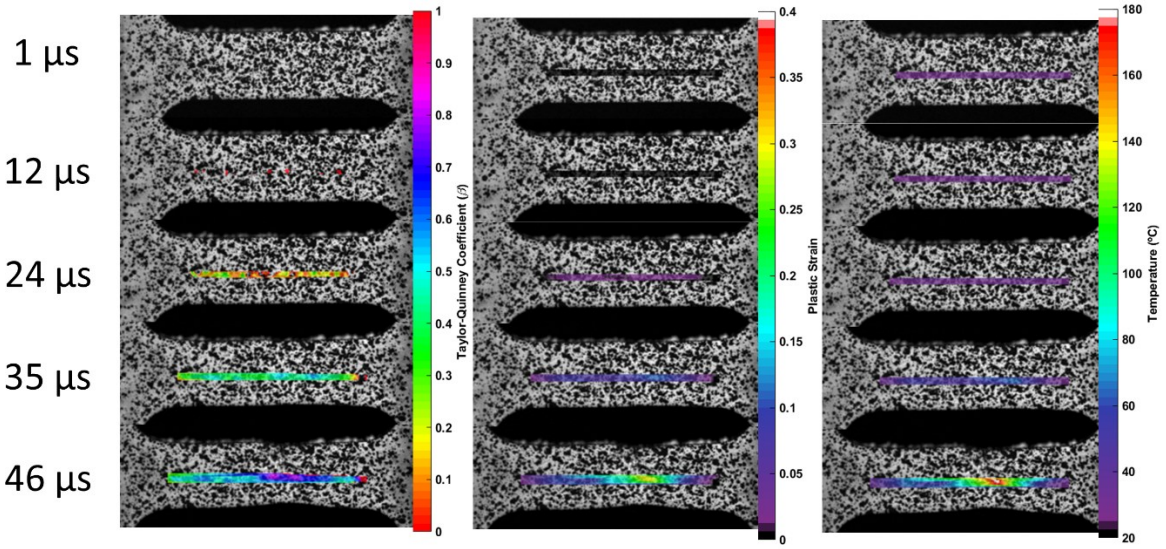

Figure 3.12. Full-Field Taylor-Quinney, Plastic Strain, and Temperature Measurements for a Ti-6Al-4V Tension Test at 6000 s^{-1}

The temperature and plastic strain along the centerline of the gage section for each high strain rate test is shown in Figure 3.13-Figure 3.15. In the 500 and 2000 s^{-1} strain rate tests the localization region is identified by strains that increase over 0.05 and a

change in temperature over 20ºC. In the 6000 s^{-1} test the localization region is identified by a plastic strain increase over 0.1 and temperature increase over 40ºC.

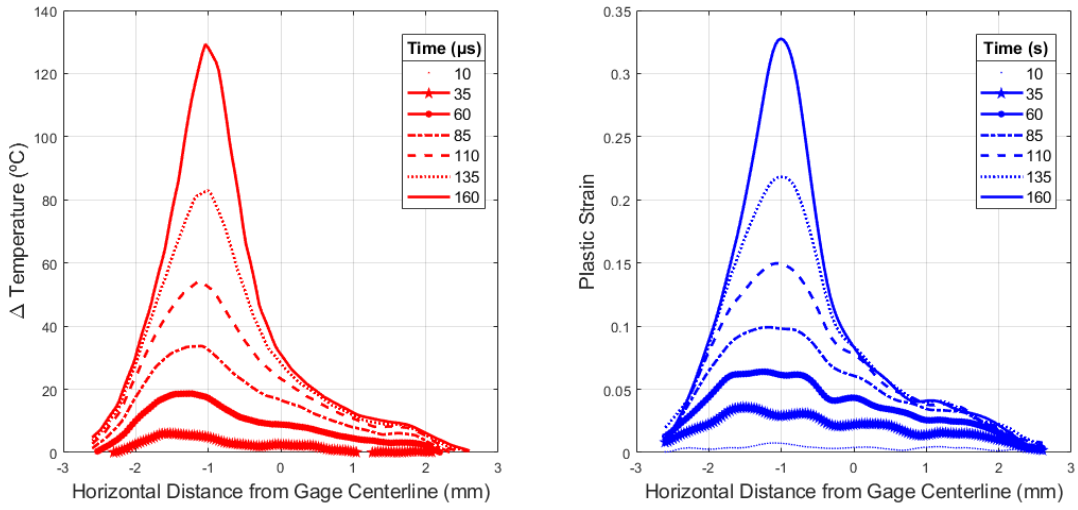

Figure 3.13.Temperature and Plastic Strain along the Gage Section for a Ti-6Al-4V Tension Test at 500 s^{-1}

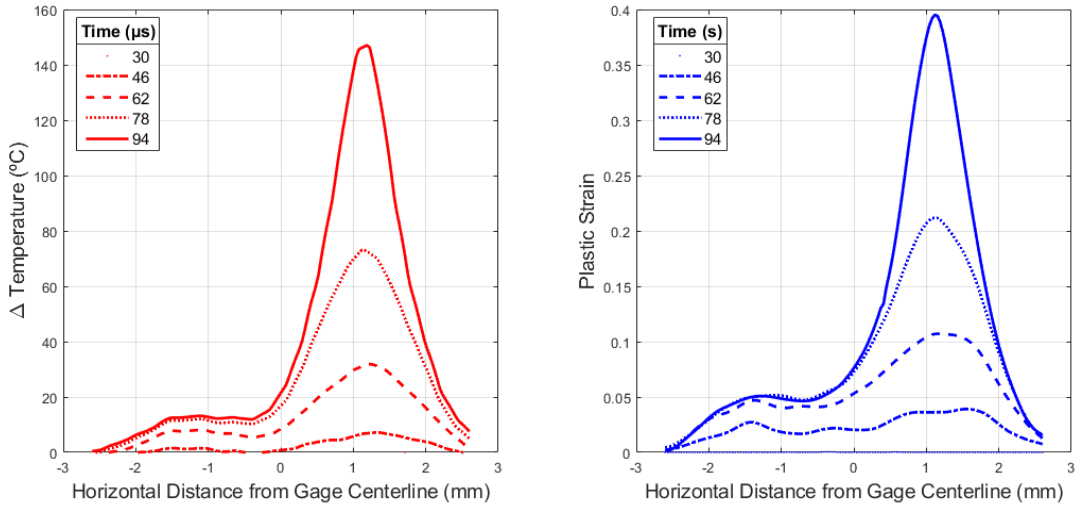

Figure 3.14 Temperature and Plastic Strain along the Gage Section for a Ti-6Al-4V Tension Test at 2000 s^{-1}

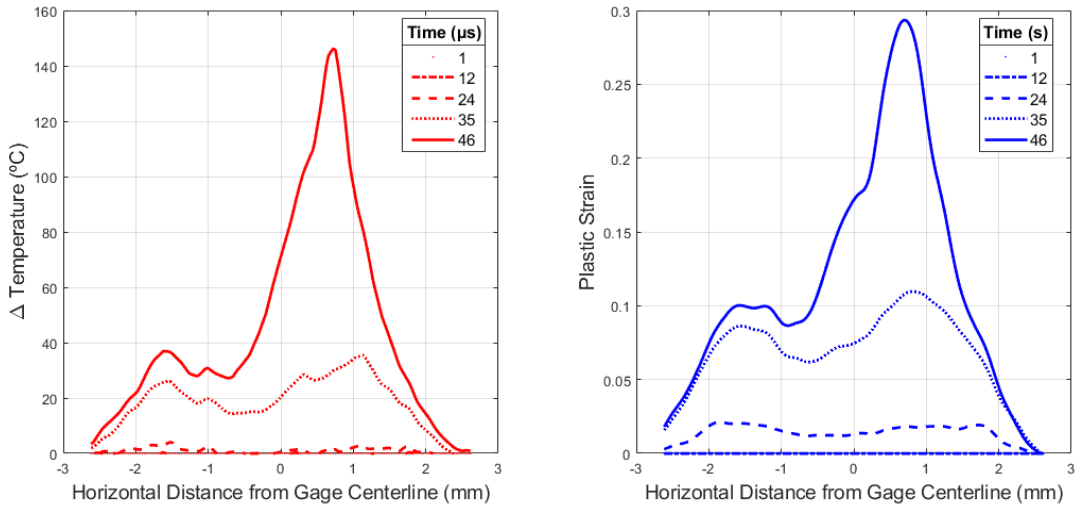

Figure 3.15 Temperature and Plastic Strain along the Gage Section for a Strain Rate of 6000 s^{-1}

In Figure 3.16-Figure 3.18 the β calculated along the centerline in the left image is the proportion of the strain energy to the thermal energy shown in the right image. Line types of each plot designate the time stamps of the infrared measurements in Figure 3.2 (d-f). The β remained below 0.8 for each test except in regions where the plastic deformation and temperature measurements were small and easily influenced by noise in the data.

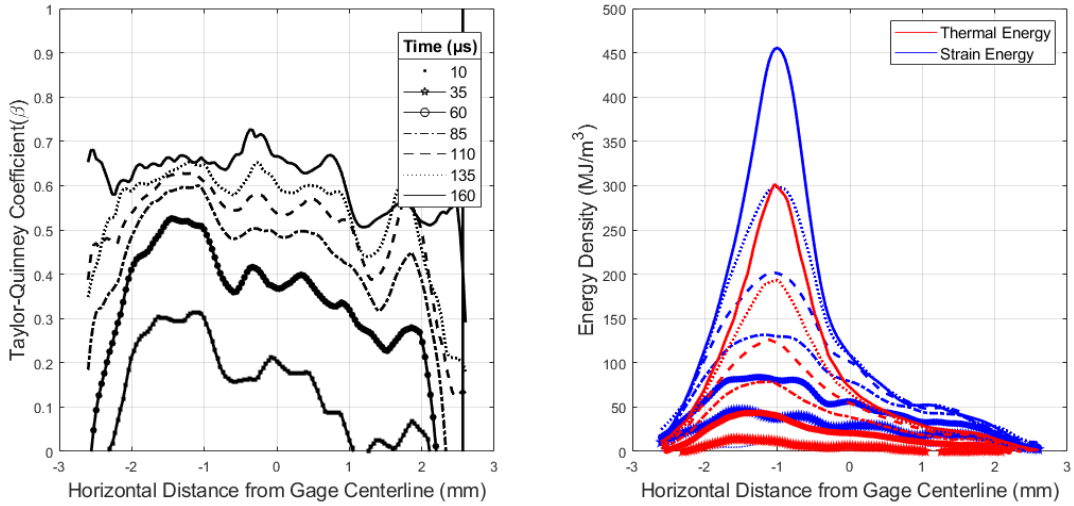

Figure 3.16 Taylor-Quinney Coefficient and Energy Density Comparison along the Gage Section for a Ti-6Al-4V Tension Test at 500 s^{-1}

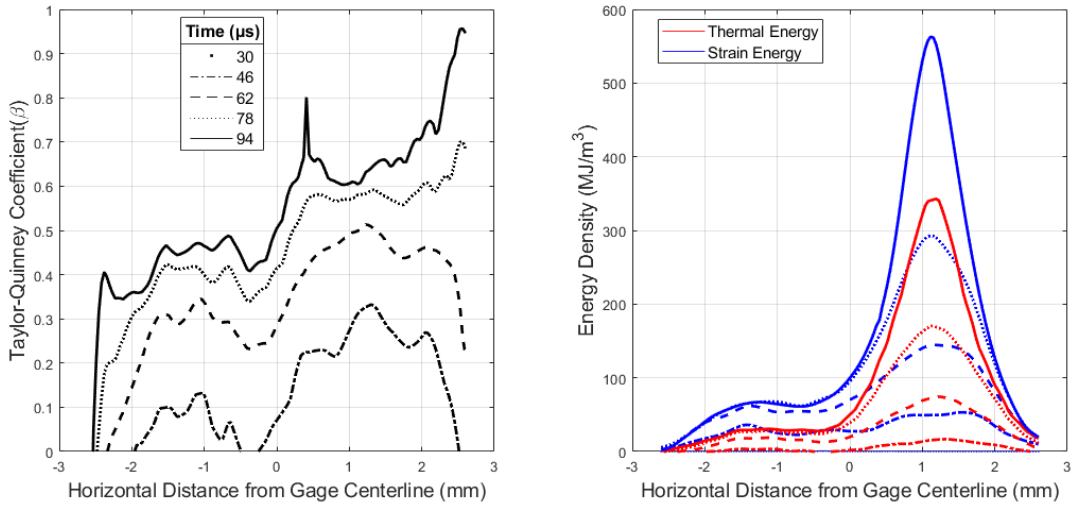

Figure 3.17 Taylor-Quinney Coefficient and Energy Density Comparison along the Gage Section for a Ti-6Al-4V Tension Test at 2000 s^{-1}

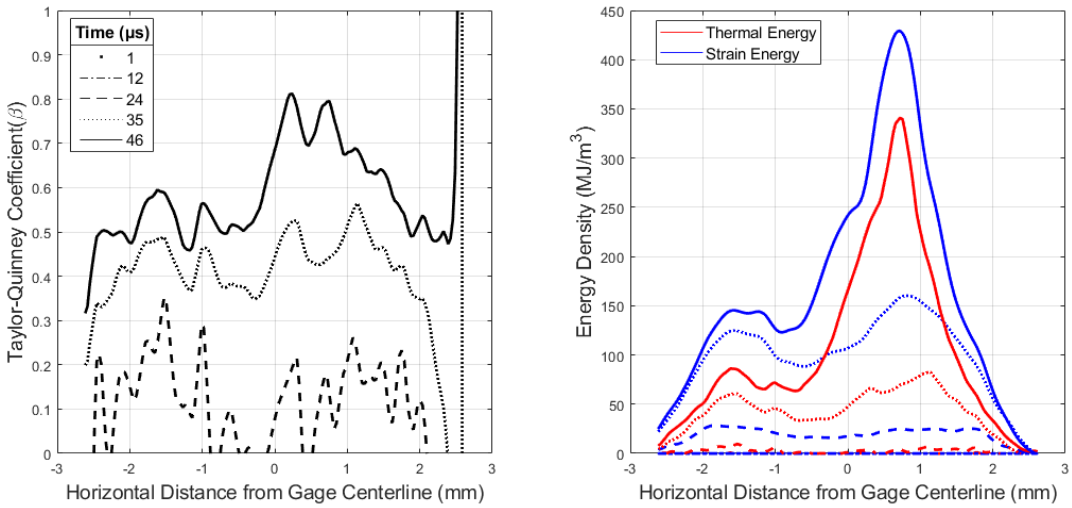

Figure 3.18 Taylor-Quinney Coefficient and Energy Density Comparison along the Gage Section for a Ti-6Al-4V Tension Test at 6000 s^{-1}

The moving average of the β versus plastic strain for the average lines across the localization region for each of the high rate tension tests is shown in Figure 3.19. The spread in the data at the strain rates of 2000 and 6000 s^{-1} is greater than that of the 500 s^{-1} due to the reduction in the number of available temperature data points. The comparison of the β moving averages for each strain rate test are displayed in Figure 3.20. The initial slope of the 1.0 s^{-1} and 0.1 s^{-1} test is comparable up to a plastic strain of 0.025 and a β of 0.425. Past this point the conduction affects the 0.1 strain rate test and the β decreases from 0.45 to 0.35 over the strains of 0.05 to 0.35. At 0.1 plastic strain the strain rate tests of 1 and above have β values that all lie between 0.5-0.6. These tests remain relatively constant up to local plastic strains of 0.25-0.35 except for the 6000 s^{-1} test in which β increases to 0.7-0.8 between local plastic strains of 0.2-0.25. The differences in the slope of β in strains between 0-0.1 for the MTS tests versus the SHB tests is mainly due to the lack of available temperature data during the shorter SHB tests.

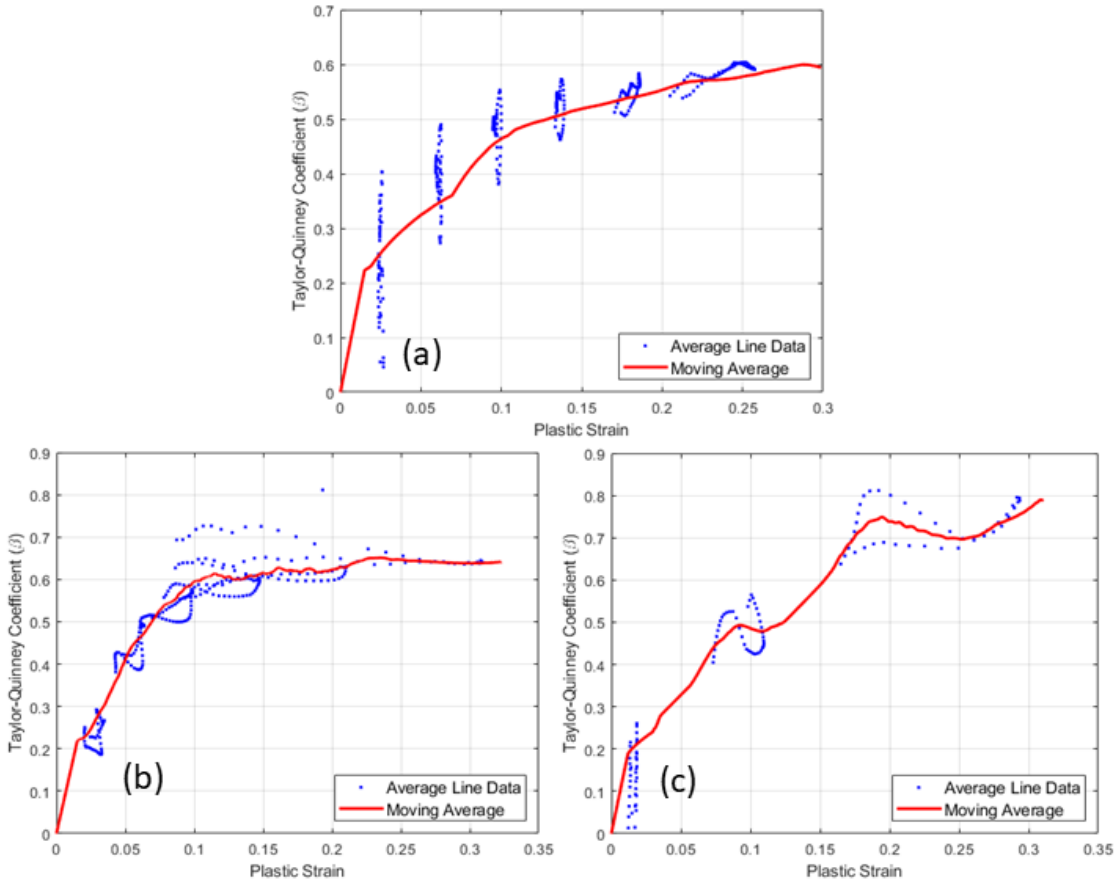

Figure 3.19 Moving Average of Taylor-Quinney Coefficient vs. Plastic Strain for Tension Tests of Ti-6Al-4V at Strain Rates of (a) 500 s^{-1}, (b) 2000 s^{-1}, and (c)6000 s^{-1}

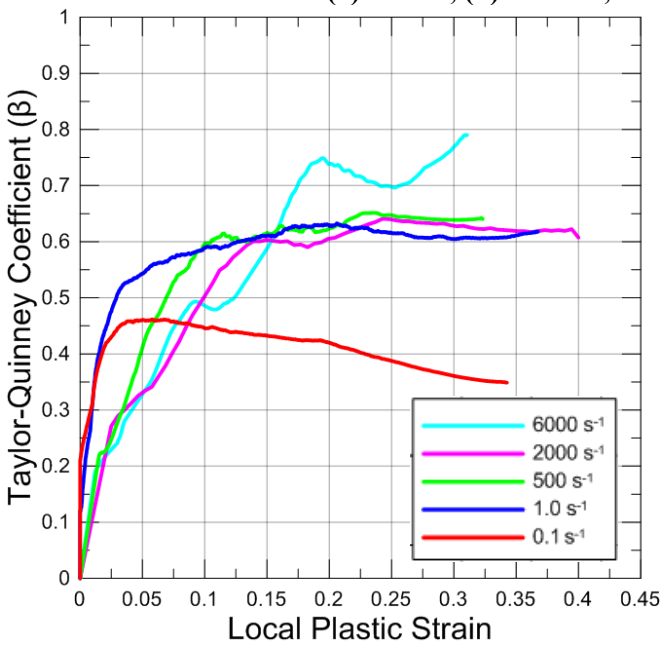

Figure 3.20. Moving Average of β vs. Plastic Strain for each Ti-6Al-4V Tension Test

The average thermal energy densities are plotted against the strain energy densities for each of the lines located in the localization regions in Figure 3.21. The linear slopes of these data points are calculated and presented in Table 3.1. The average β values will be used as the values of β in the LS-DYNA material model.

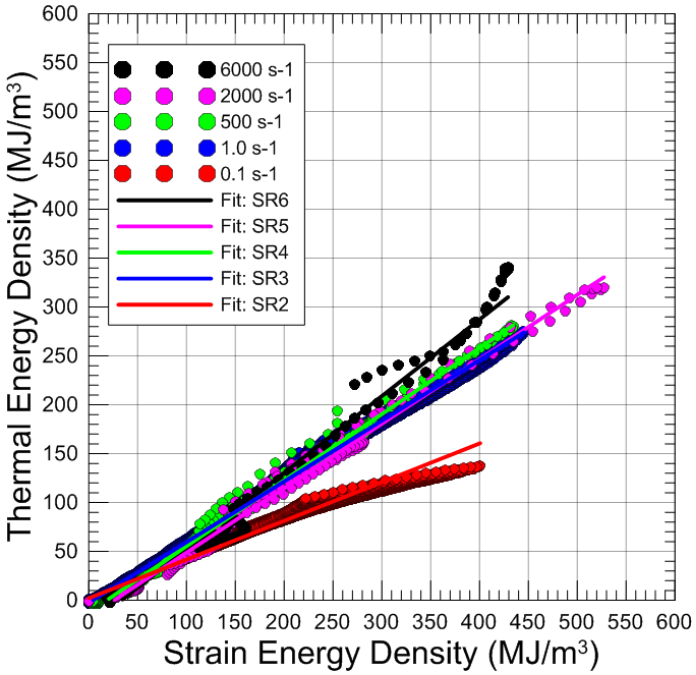

Figure 3.21. Thermal Energy Density Comparison with Strain Energy Density to Calculate Average β Values for Ti-6Al-4V

Table 3.1. Average Taylor-Quinney Coefficients for Ti-6Al-4V based on Energy Density Comparisons

Strain Rate (s^{-1})	Average β from Slope
0.1	0.396
1	0.621
500	0.675
2000	0.659
6000	0.784

3.2 Experimental Results from Aluminum 2024-T351 Tension Tests

Representative true stress versus true strain for the Aluminum 2024-T351 tension tests at various strain rates are presented in Figure 3.22. The representative data shows that the material is nearly strain rate insensitive at all strain rates.

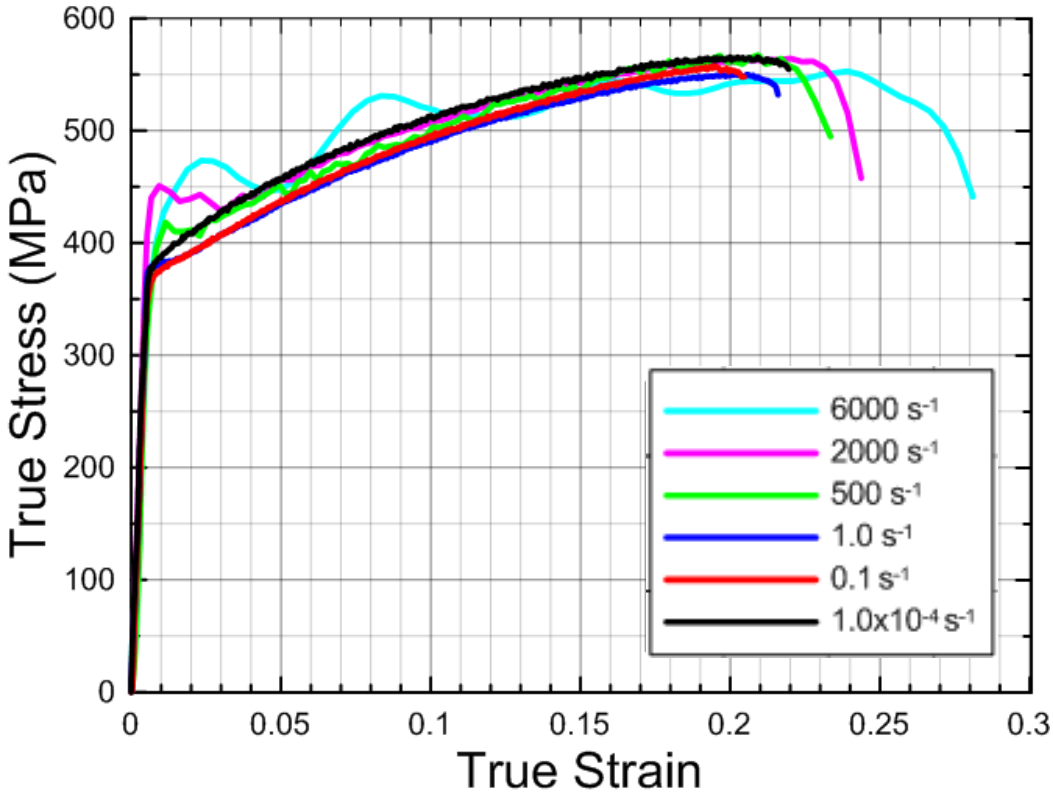

Figure 3.22 True Stress vs. True Strain Data from Aluminum 2024-T351 Tension Tests at Various Strain Rates

The change in temperature and Hencky strain measured at the point of failure for a representative tension test at each strain rate is shown in Figure 3.23. The displayed data points are from time stamps where the infrared and strain measurements were synchronized. The rate of temperature change in the SHB tests is comparable across the measured Hencky Strain values. The 1 s^{-1} has a similar behavior to the SHB tests up to a

strain of 0.15 before it diverges due to non-adiabatic behavior. The 1E-4 s^{-1} test exhibits isothermal properties.

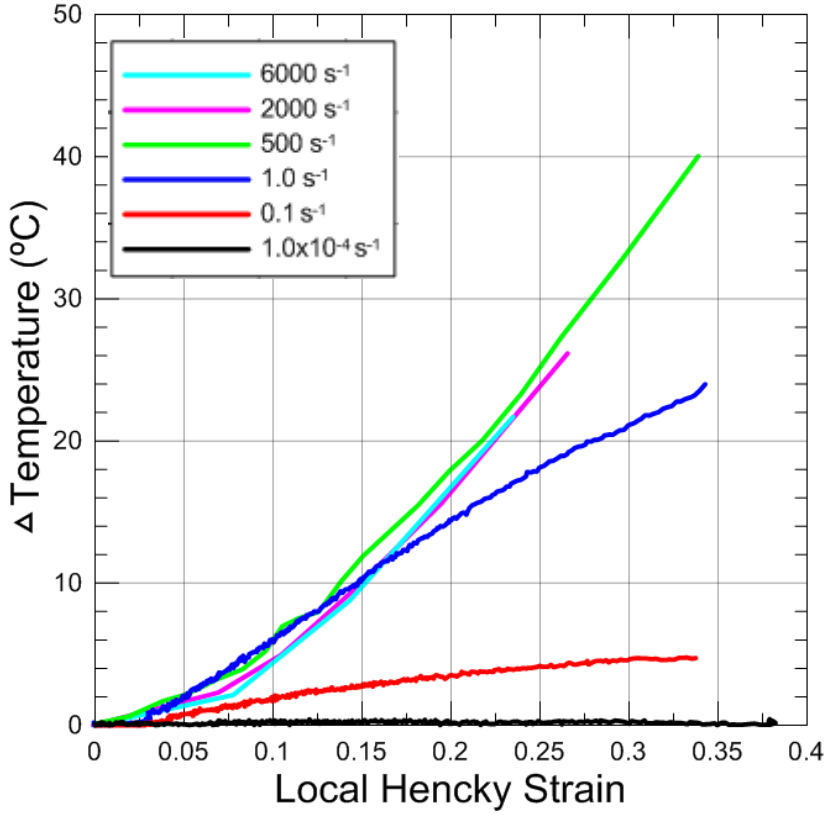

Figure 3.23 Change in Temperature versus Local Axial Hencky Strain at the Point of Failure for each Al2024-T351 Tension Test

Strain history of a 4 mm extensometer across the gage section is plotted with the strain and temperature history of the failure point in Figure 3.24. A change in temperature is first measured at approximately a strain of 0.03 in each non-isothermal strain rate test. The localized strain of the failure point aligns with the strain measured by the 4 mm extensometer up to a strain of 0.15 where necking occurs. In the 6000 s^{-1} test necking does not occur until a strain of 0.25. The rate of the change in temperature increases for each test once necking is initiated.

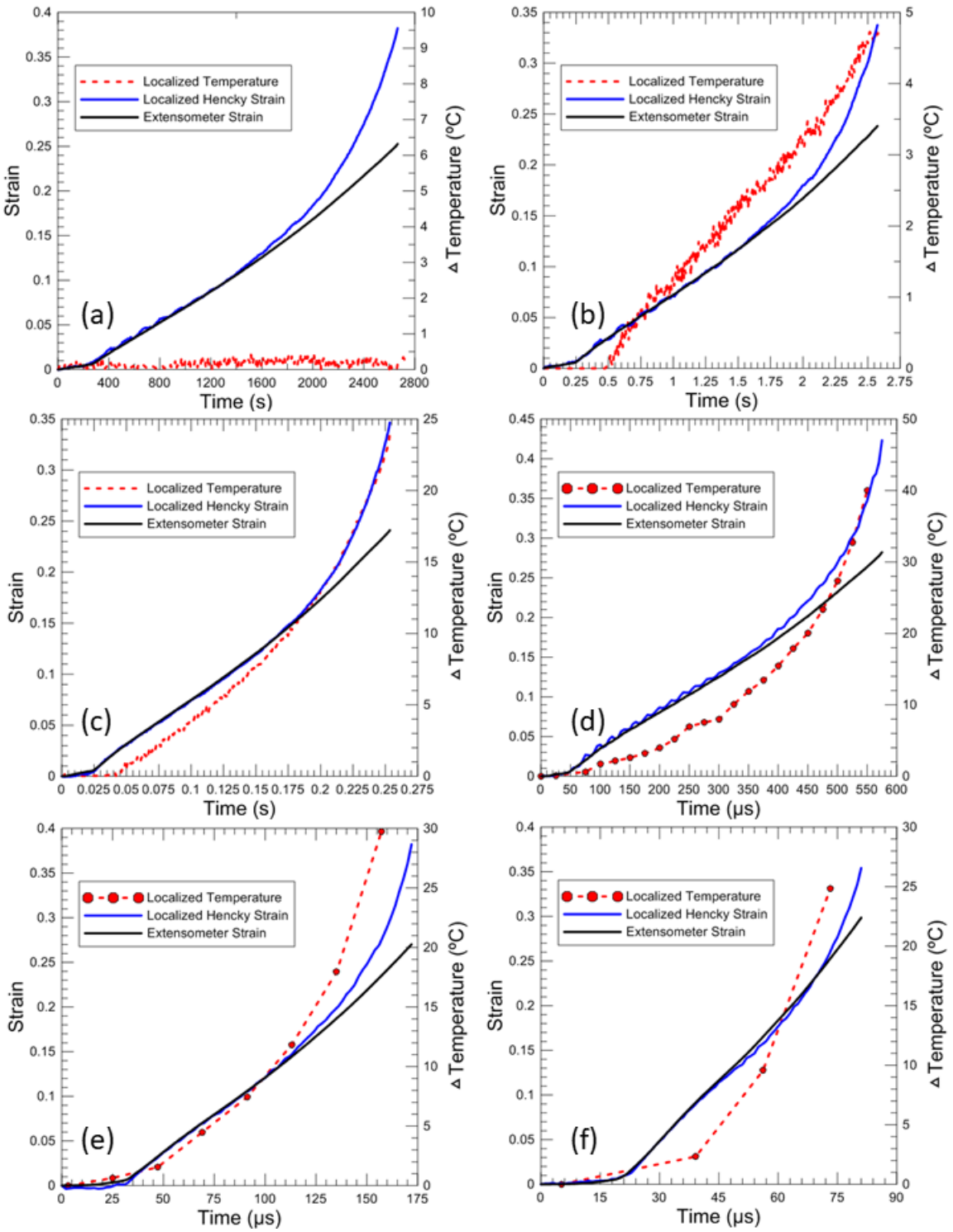

Figure 3.24 Strain and Temperature History for the Failure Point during Tension Tests of Aluminum 2024-T351 at Strain Rates of (a) 1E-4 s^{-1} (b) 0.1 s^{-1} (c) 1 s^{-1} (d) 500 s^{-1} (e) 2000 s^{-1} (f) 6000 s^{-1}

Full-field images of β, temperature, and plastic strain are displayed for the strain rates of 1 s^{-1} to 6000 s^{-1} in Figure 3.25Figure 3.28. The Taylor-Quinney coefficient for the 1 s^{-1} test remains constant across the entirety of the gage section between 0.35-0.45 once a plastic strain >0.05 is developed. In the SHB tests the β remains constant across the gage section until a localized region of plastic strain >0.2 is initiated. This localized region causes a larger rise in temperature than the 1 s^{-1} test and results in a β between 0.55-0.65.

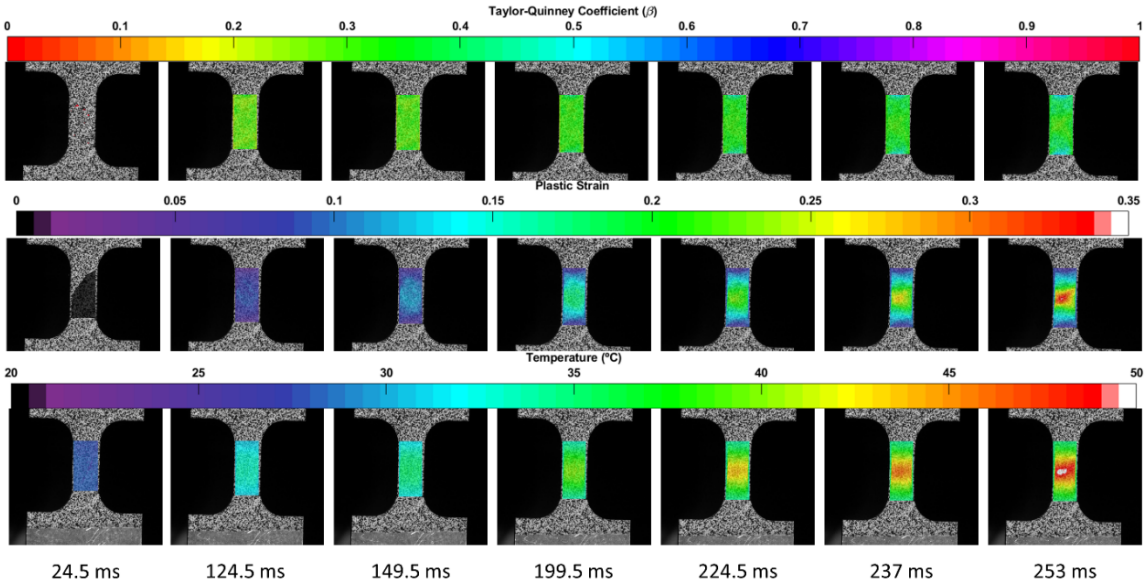

Figure 3.25 Full-Field Taylor-Quinney, Plastic Strain, and Temperature Measurements for an Aluminum 2024-T351 Tension Test at 1 s^{-1}

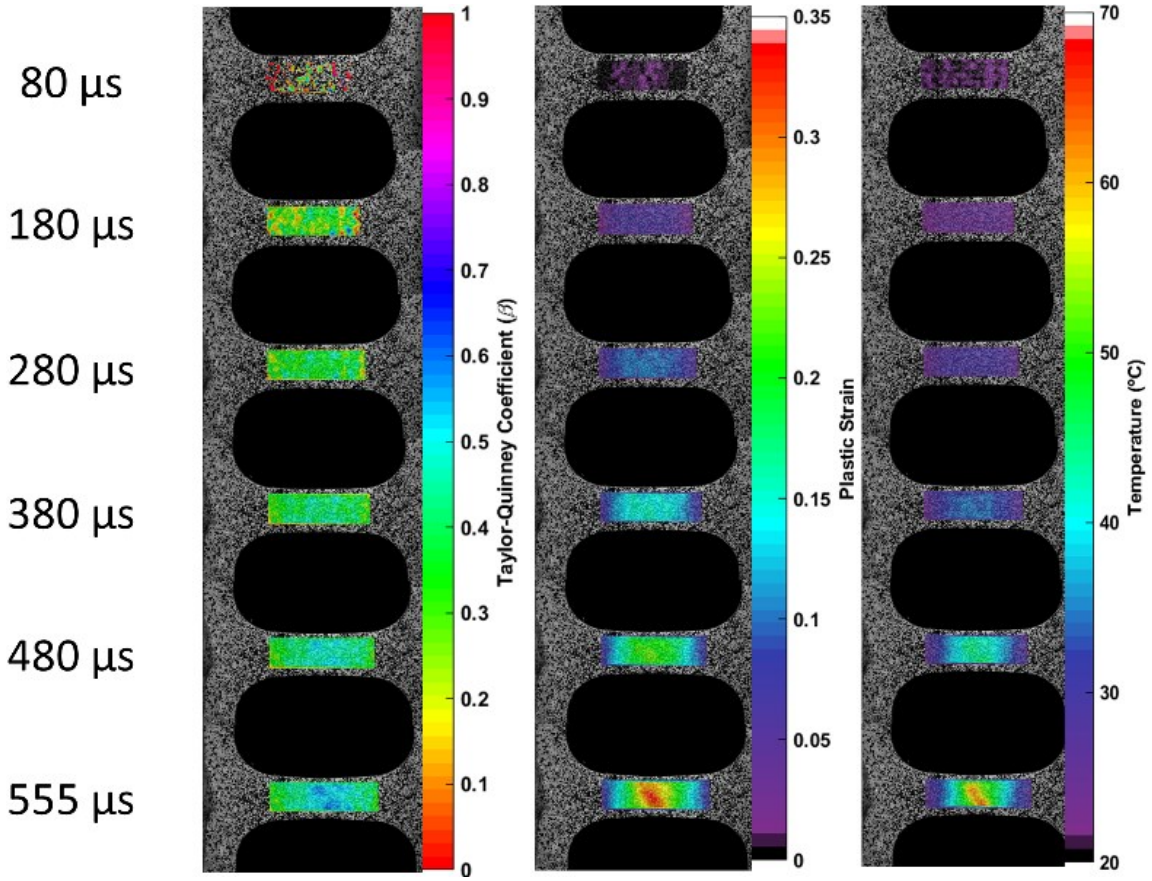

Figure 3.26 Full-Field Taylor-Quinney, Plastic Strain, and Temperature Measurements for an Aluminum 2024-T351 Tension Test at 500 s^{-1}

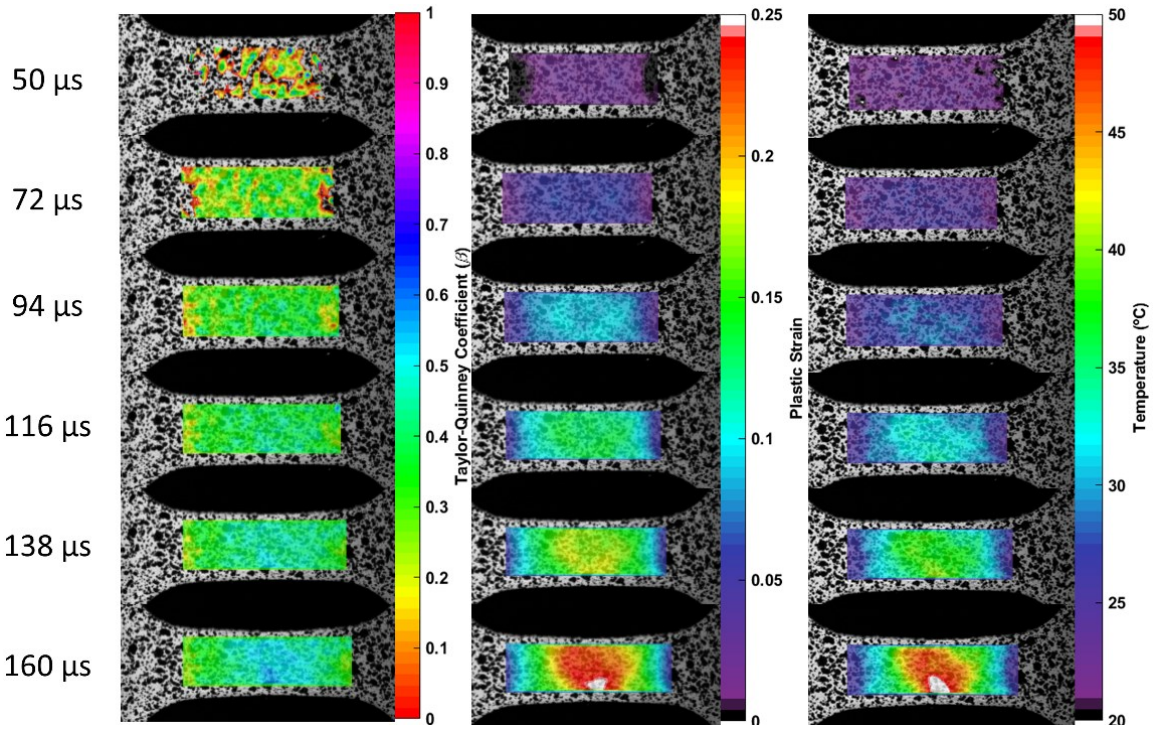

Figure 3.27 Full-Field Taylor-Quinney, Plastic Strain, and Temperature Measurements for an Aluminum 2024-T351 Tension Test at 2000 s^{-1}

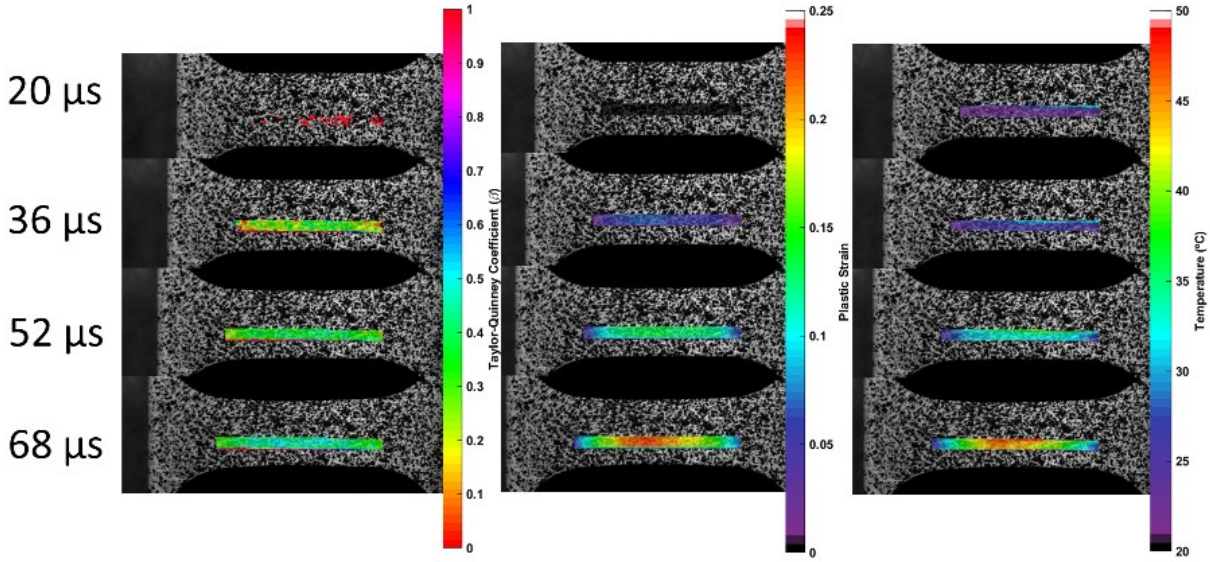

Figure 3.28 Full-Field Taylor-Quinney, Plastic Strain, and Temperature Measurements for an Aluminum 2024-T351 Tension Test at 6000 s^{-1}

Measurements of plastic strain and temperature along the centerline of each strain rate test are shown in Figure 3.29Figure 3.32. In Figure 3.29 the non-adiabatic conditions

of the 1 s^{-1} test are evident as the temperature increases as the strain remains constant in regions outside the localization. The localization region in these experiments are not as pronounced as in Ti-6Al-4V and Inconel 718. When a maximum strain of 0.15 is reached in each strain rate the difference between the center point and the edges of the 4 mm region centered at the localization is 0.05. At the final synchronized measurements temperature and strain values in the 4 mm gage region reach approximately 50% of the maximum values of temperature and strain.

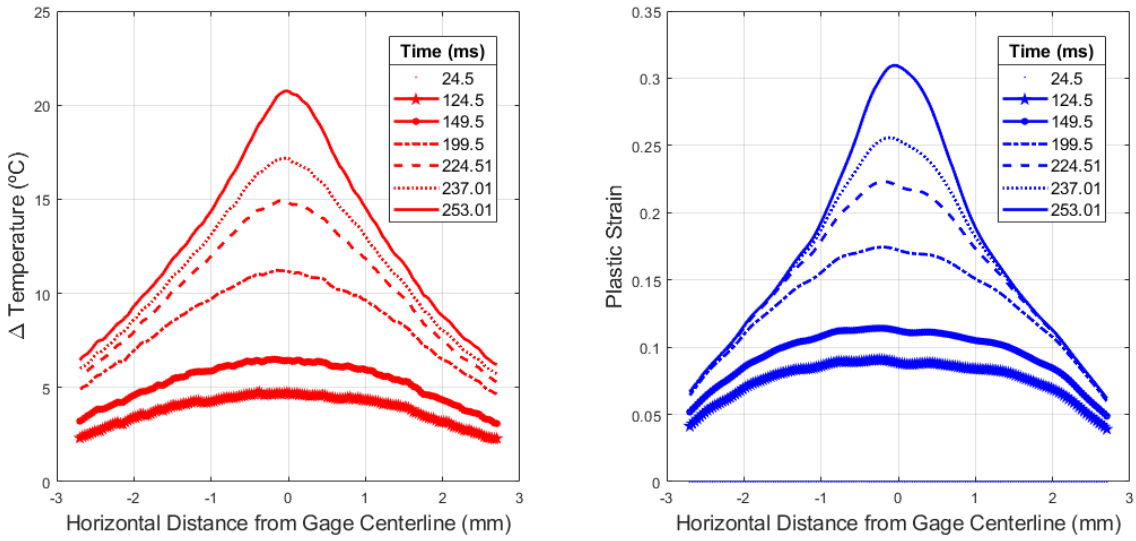

Figure 3.29 Temperature and Plastic Strain along the Gage Section for an Aluminum 2024-T351 Tension Test at 1 s^{-1}

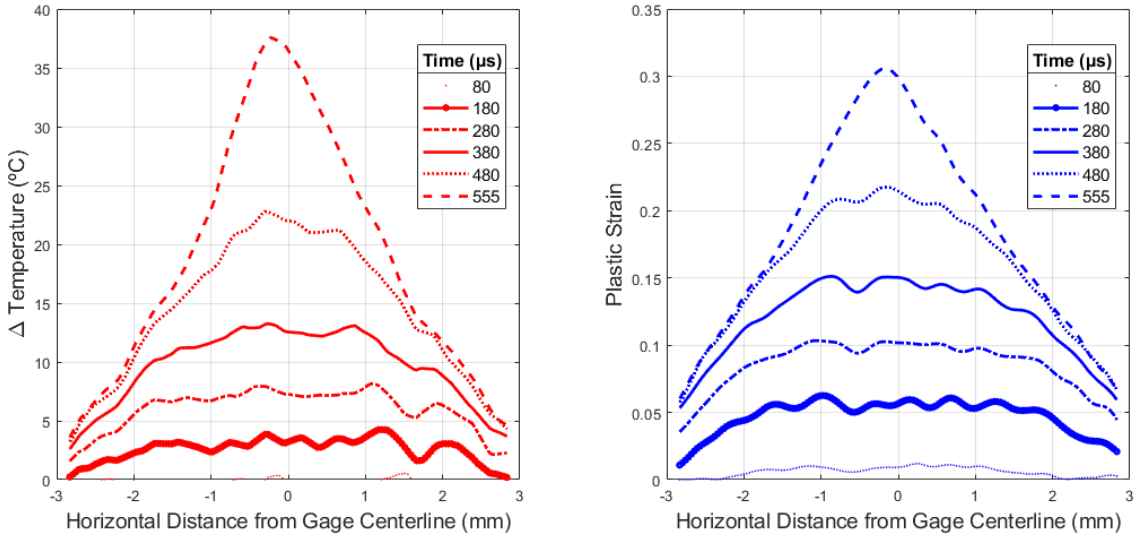

Figure 3.30 Temperature and Plastic Strain along the Gage Section for an Aluminum 2024-T351 Tension Test at 500 s^{-1}

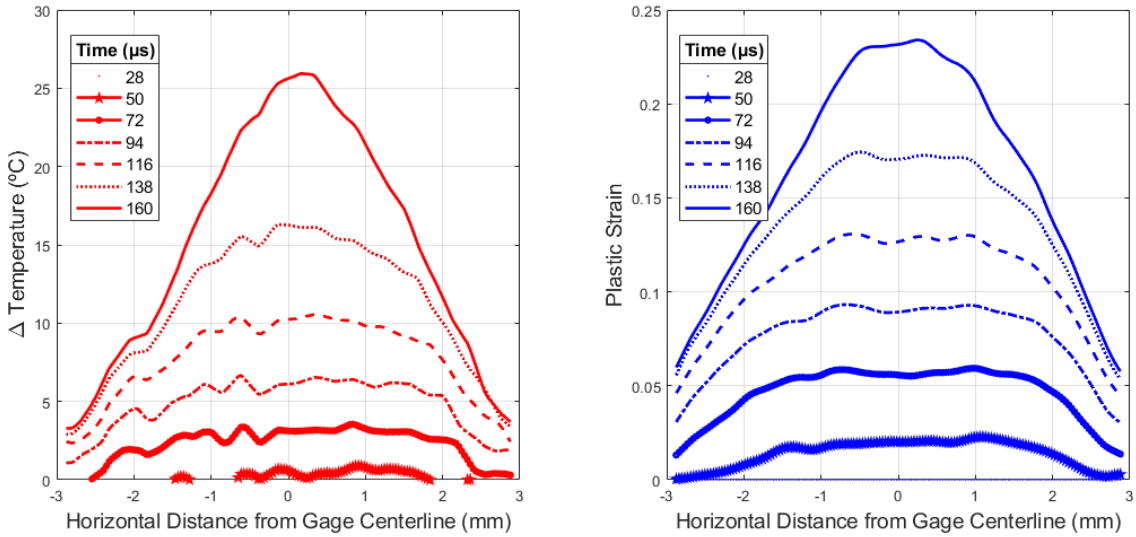

Figure 3.31 Temperature and Plastic Strain along the Gage Section for an Aluminum 2024-T351 Tension Test at 2000 s^{-1}

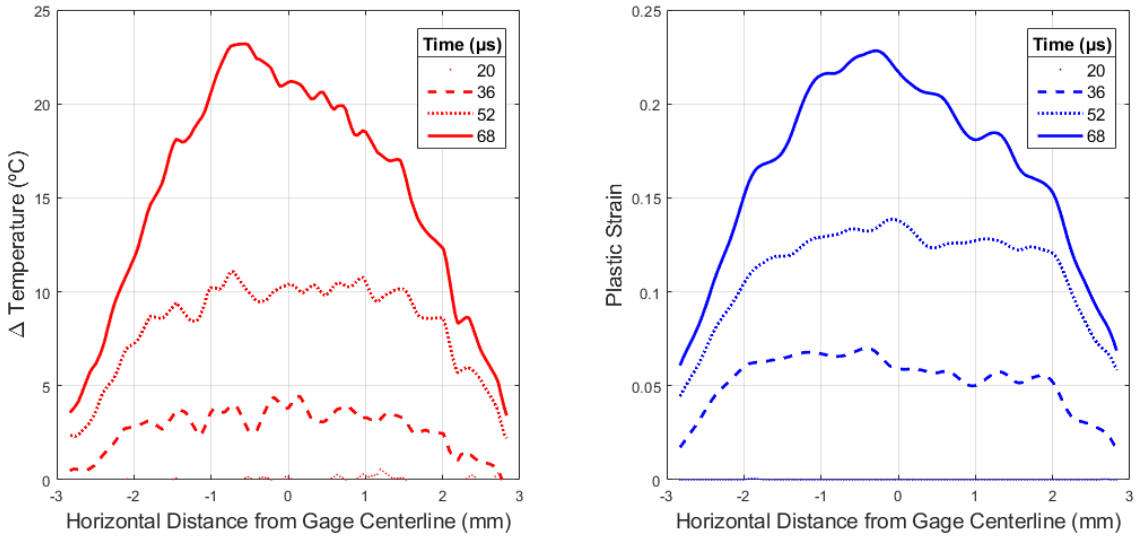

Figure 3.32 Temperature and Plastic Strain along the Gage Section for an Aluminum 2024-T351 Tension Test at 6000 s^{-1}

The β and corresponding energy density measurements along the same centerline are displayed in Figure 3.33-Figure 3.36. The non-adiabatic behavior of the 1 s^{-1} test is shown by the increasing β outside the localization while the β remains constant with increasing strain and temperature at the center of localization. In each of the SHB tests β increases with increasing strain energy and therefore increasing strain. Areas with the highest strains in Figure 3.30-Figure 3.32 have the highest β s in corresponding Figure 3.34-Figure 3.36.

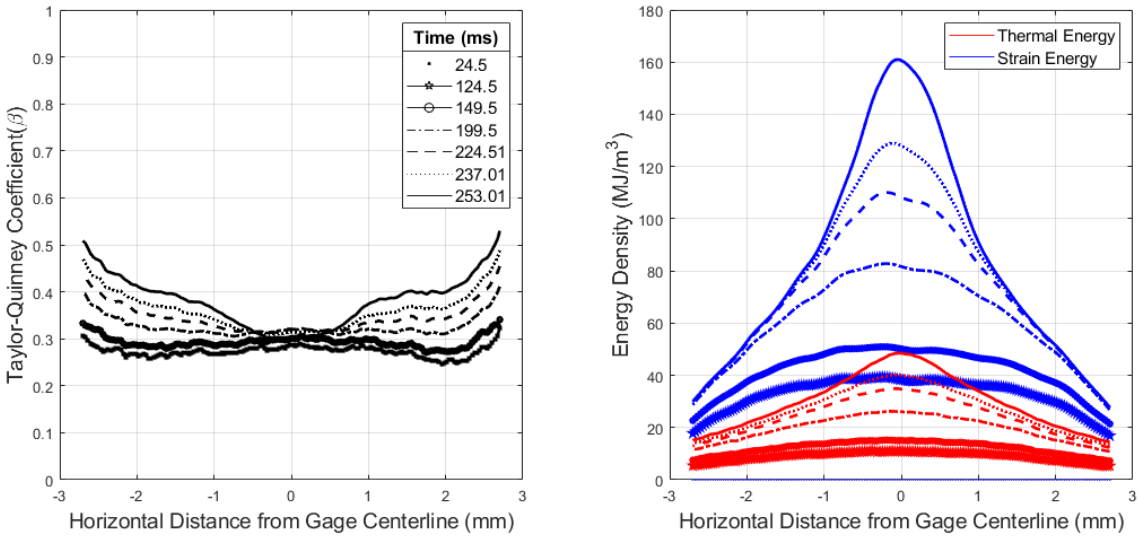

Figure 3.33 Taylor-Quinney Coefficient and Energy Density Comparison along the Gage Section for an Aluminum 2024-T351 Tension Test at 1 s^{-1}

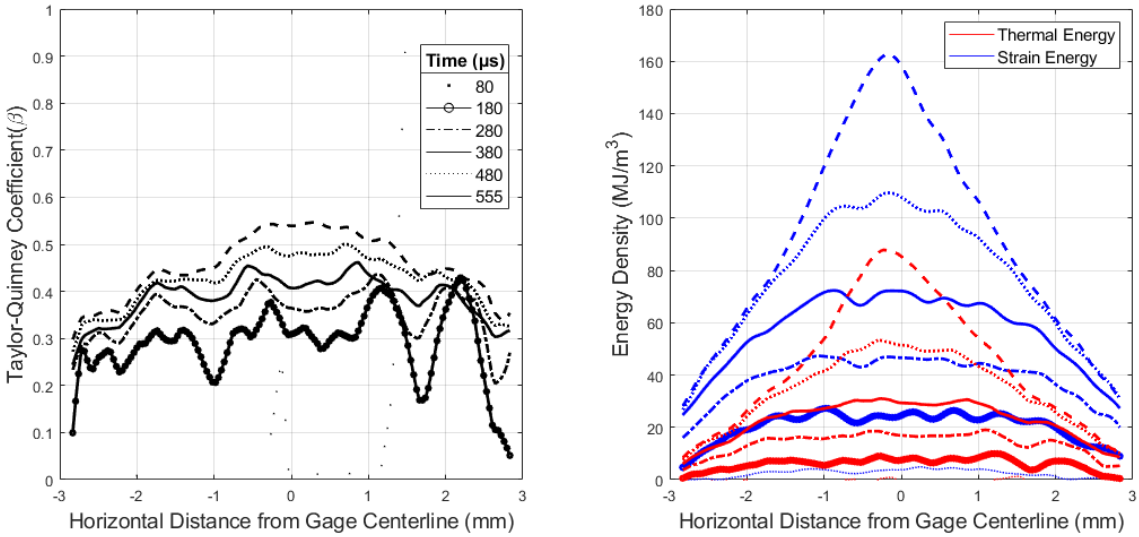

Figure 3.34 Taylor-Quinney Coefficient and Energy Density Comparison along the Gage Section for an Aluminum 2024-T351 Tension Test at 500 s^{-1}

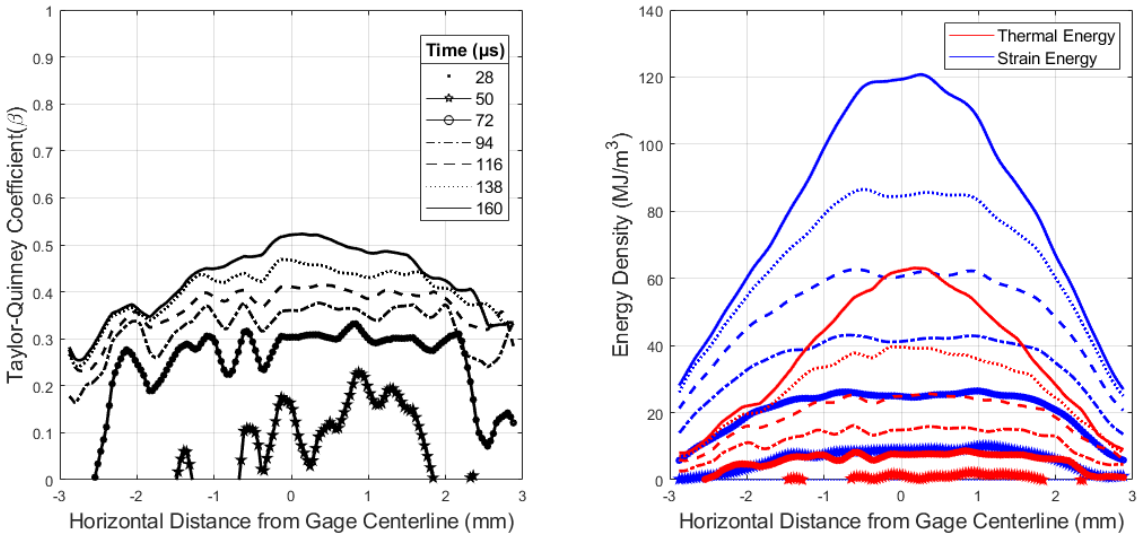

Figure 3.35 Taylor-Quinney Coefficient and Energy Density Comparison along the Gage Section for an Aluminum 2024-T351 Tension Test at 2000 s^{-1}

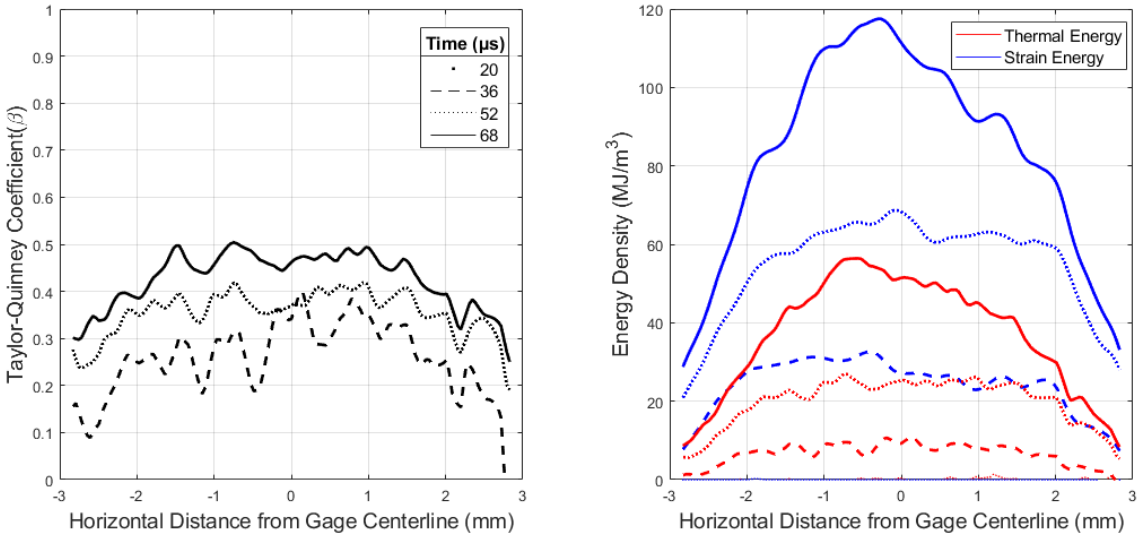

Figure 3.36 Taylor-Quinney Coefficient and Energy Density Comparison along the Gage Section for an Aluminum 2024-T351 Tension Test at 6000 s^{-1}

The average Taylor-Quinney coefficient versus local plastic strain for the points located in the localization region of each Aluminum 2024-T351 tension test at various strain rates is shown in Figure 3.37. At a strain rate of 0.1 s^{-1} the β increased from 0 to 0.15 as the strain increases from 0-0.05. Then β steadily decreases to 0.1 at a plastic strain

of 0.3. In the 1 s^{-1} test β increases from 0 to 0.3 as the plastic strain increases from 0 to 0.1 and remains constant at 0.3 up to a plastic strain of 0.3. The trend for the tests from 500 to 6000 s^{-1} is nearly identical. The β increases from 0 to 0.3 as the plastic strain increases from 0 to 0.05 then steadily increases from 0.3 to 0.5 as the plastic strain increases from 0.1 to 0.3. The increase of β with increasing strain is likely due to the inability of the material to store energy as plastic work as the strain increases so the extra energy is released as heat.

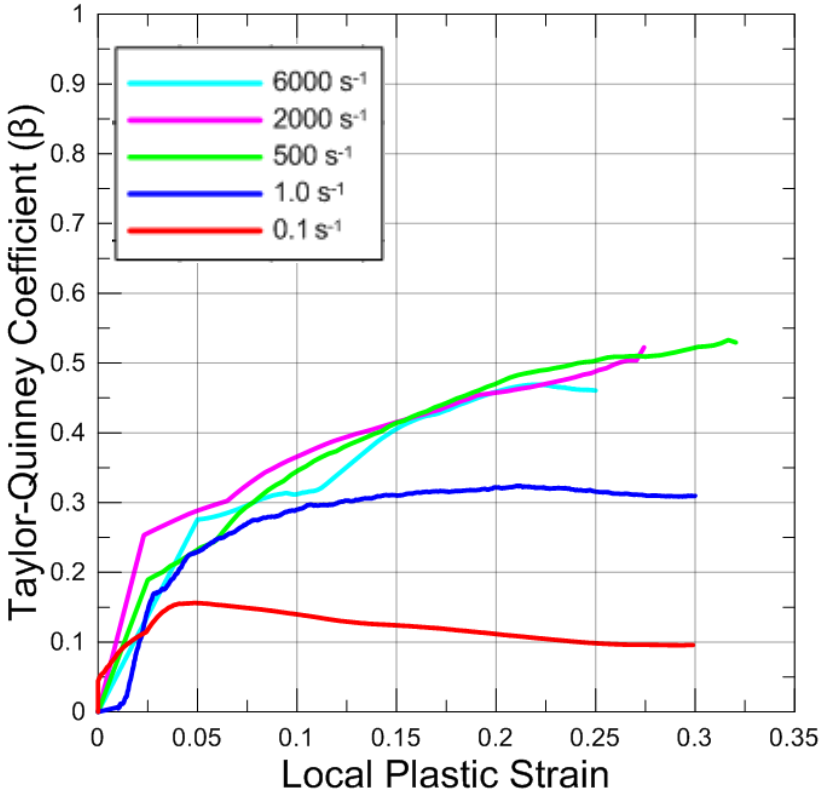

Figure 3.37 Taylor-Quinney Coefficient versus Local Axial Plastic Strain for the Localization Region of Aluminum 2024-T351 Tension Tests at Various Strain Rates

The average thermal energy densities are plotted against the strain energy densities for each of the data points in the localization regions in Figure 3.38. The linear

slopes of these data points are calculated and presented in Table 3.2. The average β values will be used as the values in the LS-DYNA material model. The differences in β in Figure 3.37 can also be seen in Figure 3.38 as the slopes of the SHB tests have similar values while the slopes of the MTS tests are lower.

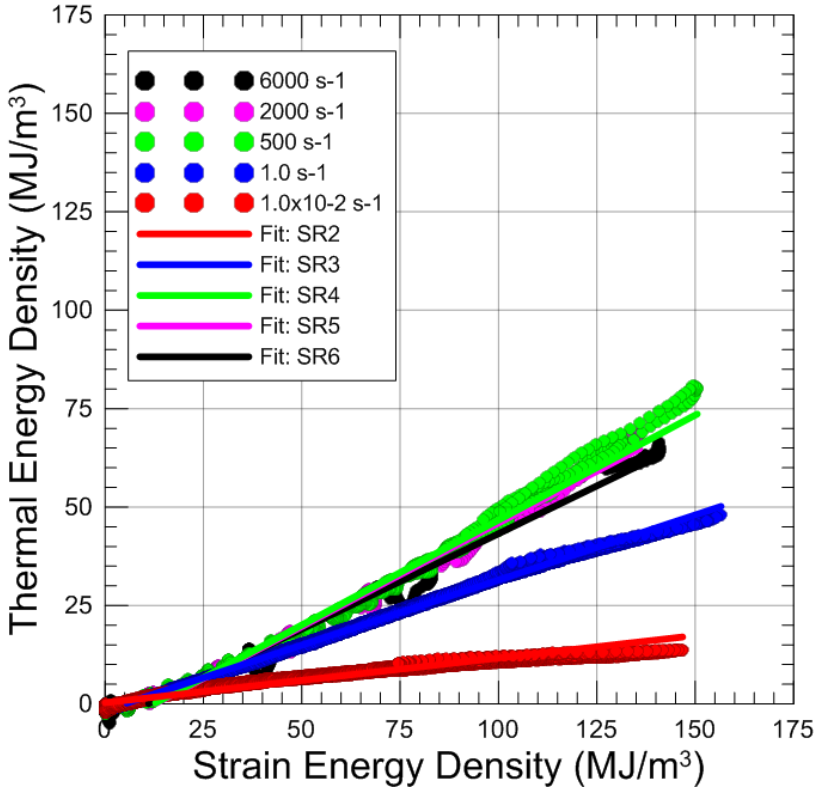

Figure 3.38 Thermal Energy Density Comparison with Strain Energy Density to Calculate Average β Values for Aluminum 2024-T351

Table 3.2 . Average Taylor-Quinney Coefficients for Aluminum 2024-T351 based on Energy Density Comparisons

Strain Rate (s^{-1})	Average β from Slope
0.1	0.114
1	0.331
500	0.533
2000	0.526
6000	0.485

3.3 Experimental Results from Inconel 718

Respresentative true stress versurs true strain data for the tension tests of Inconel 718 at various strain rates is shown in Figure 3.39. The yield point for the 1E-4 s^{-1} to 1 s^{-1} tests is ~1100 MPa with a slight increase in yield stress for the tests at 500-6000 s^{-1}. The material exhibits significat strain hardening with an increase of approximately 600 MPa between yield and ultimate stress for each striain rate. The type of strain hardening may be changing between the strain rates as the slope of the flow stress is different between the 1.0E-4 and 0.1 s^{-1} strain rate curves and the 1.0 s^{-1} curve. The 500-6000 s^{-1} curves shown here are cut in the transverse direction as opposed to the tests at lower strain rates which are cut in the rolling direction. The results from the transverse tests show similar behavior to those conducted by [9]. The directionality of the test is not expected to affect the calculation of the Taylor-Quinney coefficient.

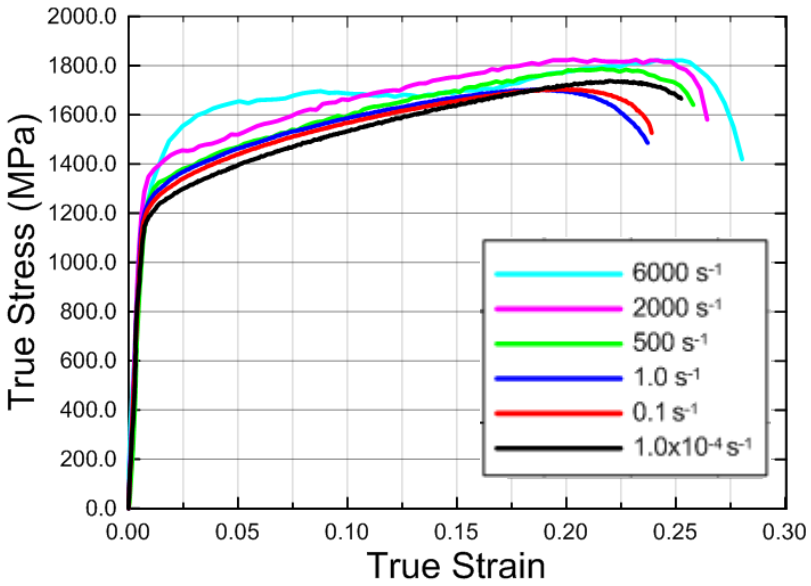

Figure 3.39 True Stress vs. True Strain Data from Tension Tests on Inconel 718 at Various Strain Rates

The change in temperature versus the local axial Hencky strain for the failure point at each strain rate is shown in Figure 3.40. The rate of change in temperature is similar for the tests at strain rates from 1-6000 s^{-1}. At a local Hencky strain of 0.35 the temperature for all 4 strain rates is between 105-110ºC. The 0.1 s^{-1} test again shows non-adiabatic effects due to the timescale of the test and the 1E-4 s^{-1} test is nearly isothermal.

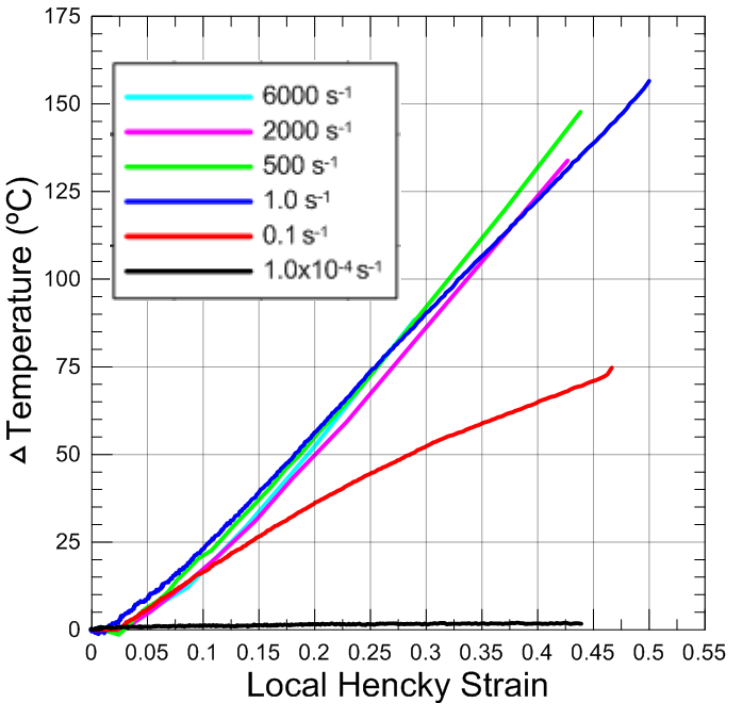

Figure 3.40 Change in Temperature versus Local Axial Hencky Strain for the Data Points Located at the Point of Failure for each Strain Rate Test

The strain history of the 4 mm extensometer across the gage section is plotted with the strain and temperature history of the failure point in Figure 3.41. In the 0.1 and 1.0 s^{-1} tests the necking is initiated at a strain of 0.15. In the remaining tests the necking occurs at a strain of 0.2-0.225 and could explain the differences in strain hardening behavior. The rate of the change in temperature increases for each test once necking is initiated.

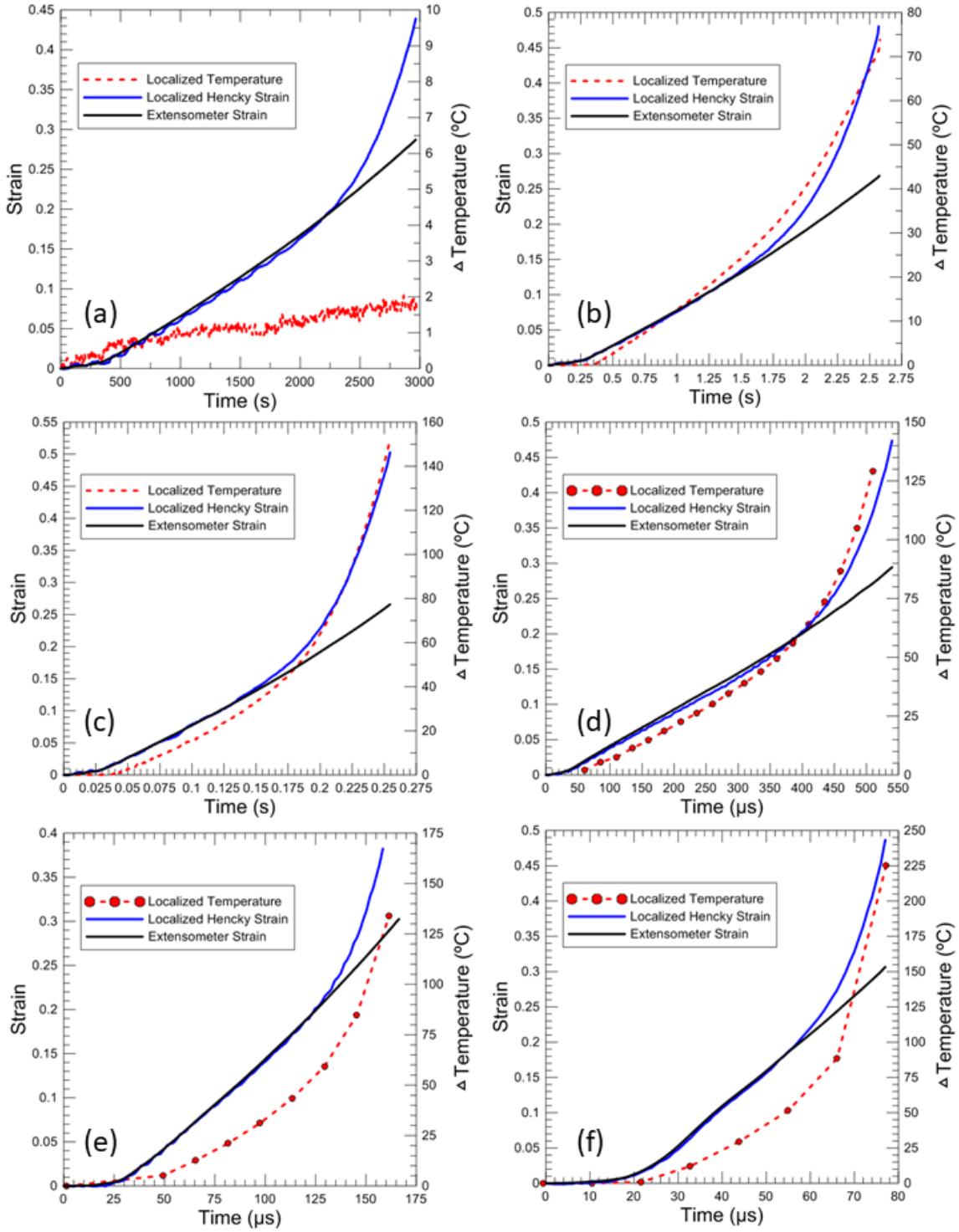

Figure 3.41 Strain and Temperature History for the Failure Point during Tension Tests of Inconel 718 at Strain Rates of (a) 1E-4 s^{-1} (b) 0.1 s^{-1} (c) 1 s^{-1} (d) 500 s^{-1} (e) 2000 s^{-1} (f) 6000 s^{-1}

Figure 3.42-Figure 3.45 display full-field images of the Taylor-Quinney coefficient, plastic strain, and temperature measurements for the Inconel 718 tests at strain rates from 1-6000 s^{-1}. In the 1 s^{-1} test non-adiabatic behavior can be seen as β increases in the region outside the localized strain and temperature due to the conduction of heat from the localization. In the strain rate tests from 500-6000 s^{-1} the β remains constant across the entire length of the gage once a strain of 0.125 is reached within the gage section.

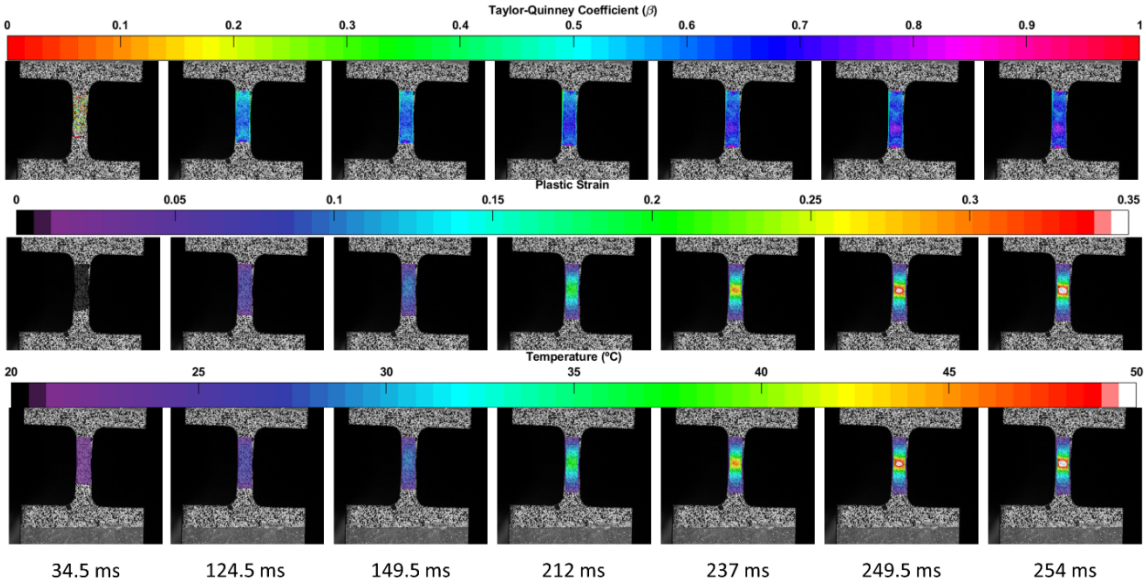

Figure 3.42 Full-Field Taylor-Quinney, Plastic Strain, and Temperature Measurements for an Inconel Tension Test at 1 s^{-1}

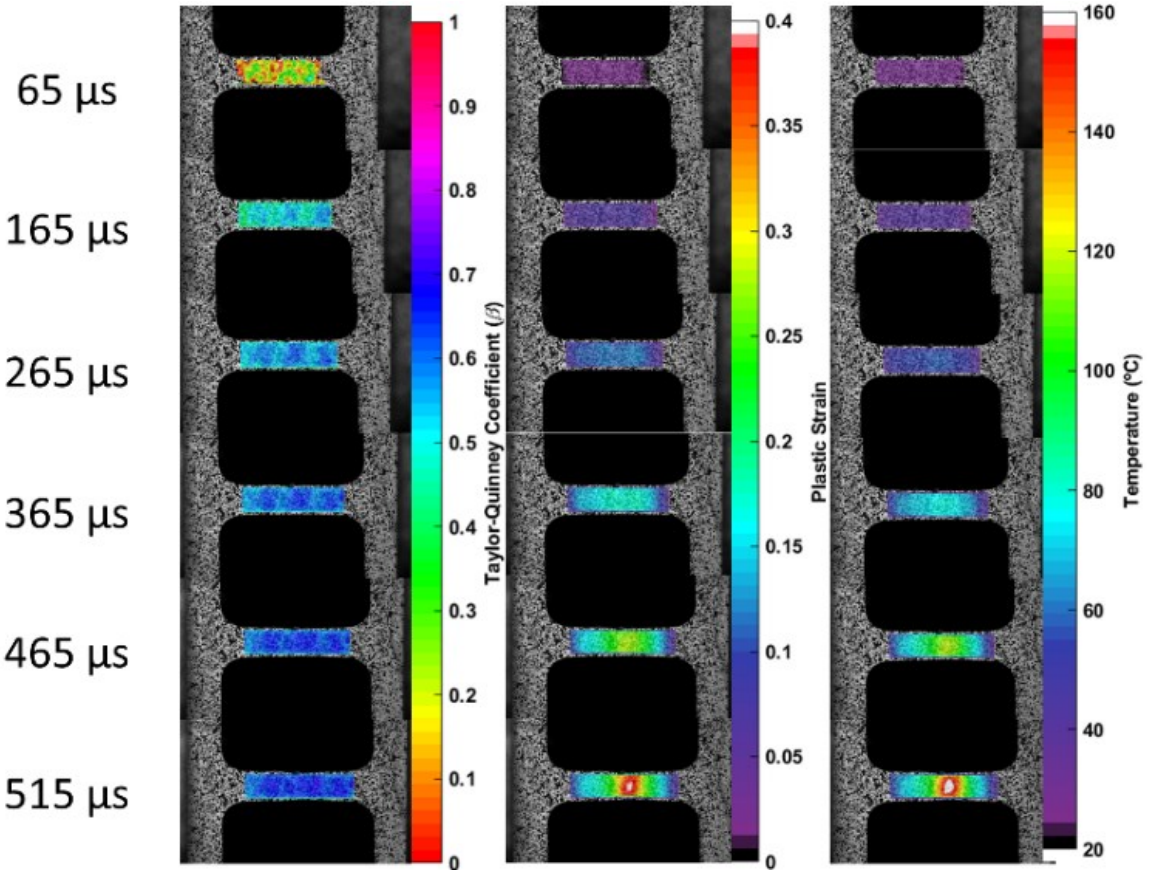

Figure 3.43 Full-Field Taylor-Quinney, Plastic Strain, and Temperature Measurements for an Inconel Tension Test at 500 s^{-1}

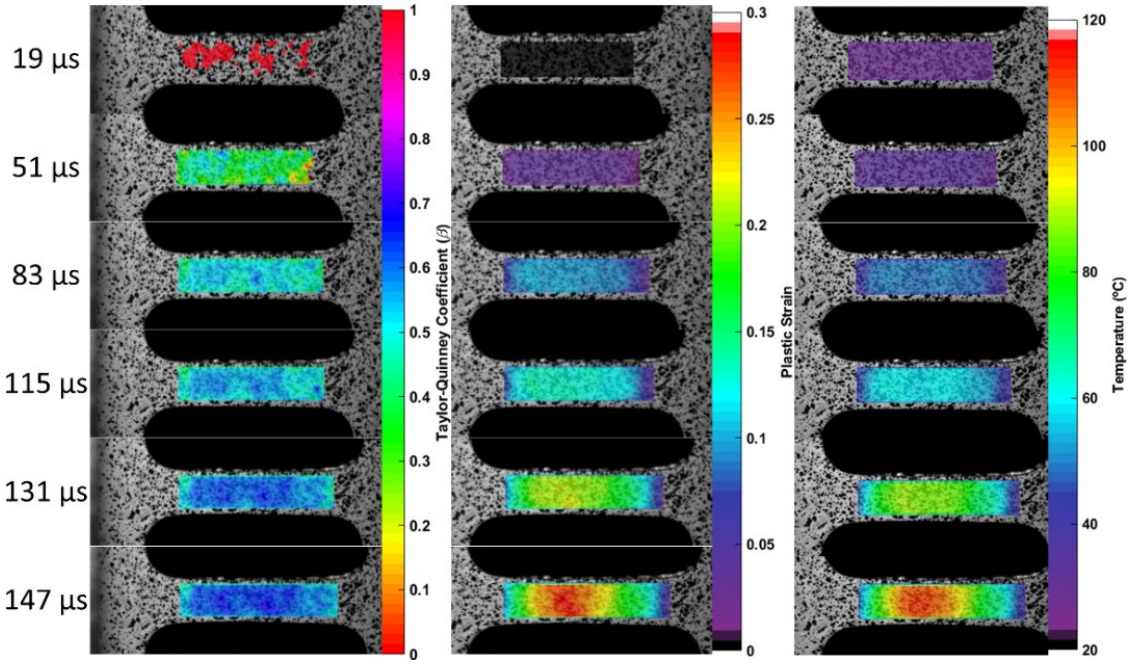

Figure 3.44 Full-Field Taylor-Quinney, Plastic Strain, and Temperature Measurements for an Inconel Tension Test at 2000 s^{-1}

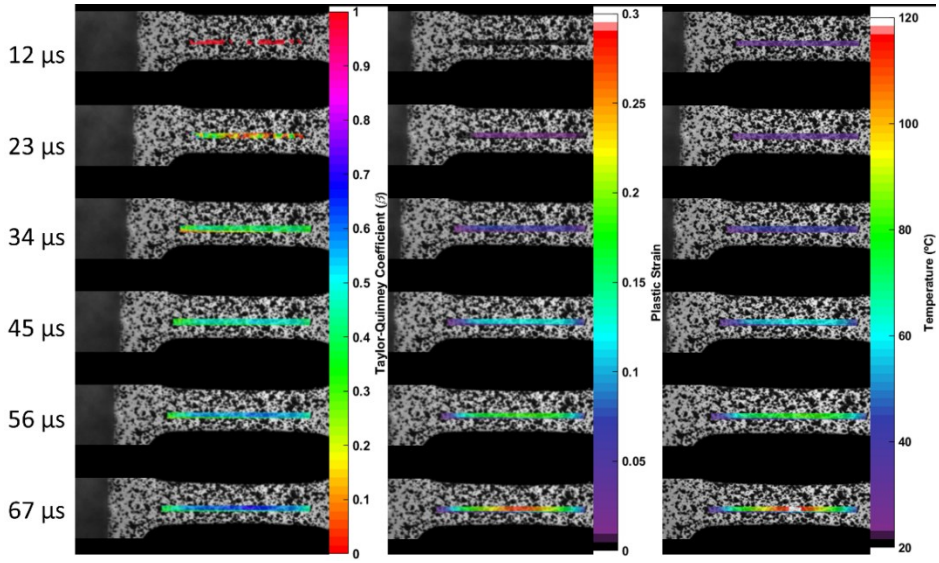

Figure 3.45 Full-Field Taylor-Quinney, Plastic Strain, and Temperature Measurements for an Inconel Tension Test at 6000 s^{-1}

Measurements of plastic strain and temperature along the centerline of each strain rate test are shown in Figure 3.46-Figure 3.50. In Figure 3.47 the non-adiabatic conditions of the 1 s^{-1} test are evident as the temperature increases as the strain

remains constant in regions outside the localization. The localization region in these experiments are not as pronounced as in other metals. When a maximum strain of 0.15 is reached in each strain rate the difference between the center point and the edges of the 4 mm region centered at the localization is 0.05. In the 2000 and 6000 s^{-1} tests the final synchronized measurements temperature and strain values in the 4 mm gage region reach approximately 50% of the maximum values of temperature and strain measured at the failure point in Figure 3.41.

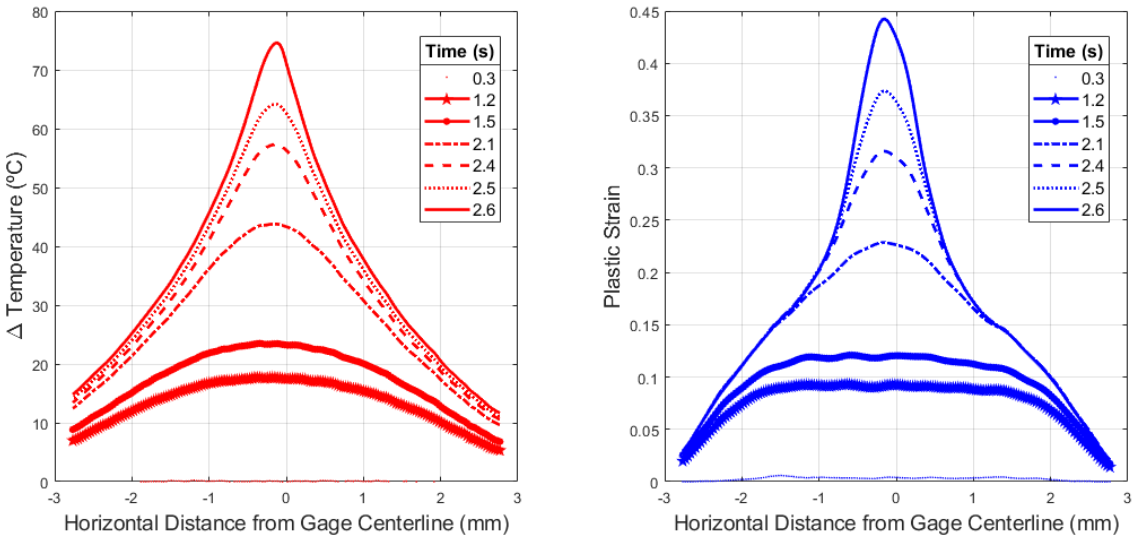

Figure 3.46 Temperature and Plastic Strain along the Gage Section for an Inconel 718 Tension Test at 0.1 s^{-1}

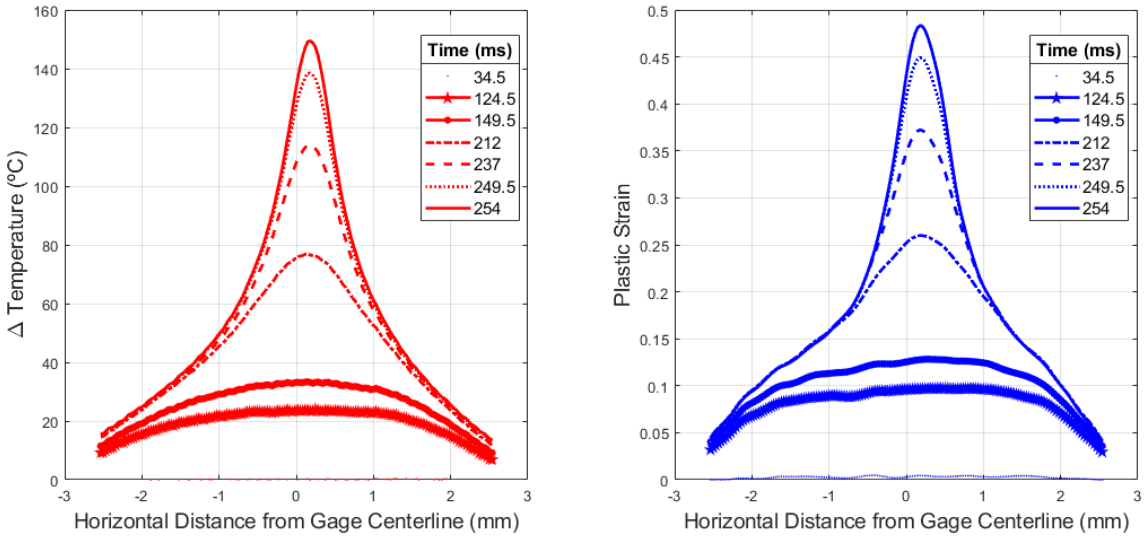

Figure 3.47 Temperature and Plastic Strain along the Gage Section for an Inconel 718 Tension Test at 1 s^{-1}

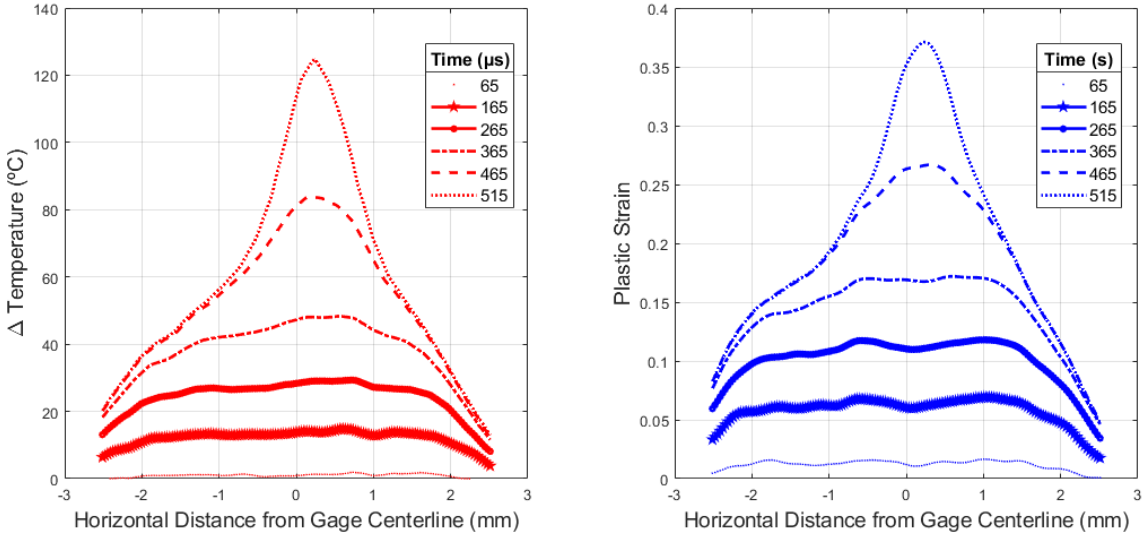

Figure 3.48 Temperature and Plastic Strain along the Gage Section for an Inconel 718 Tension Test at 500 s^{-1}

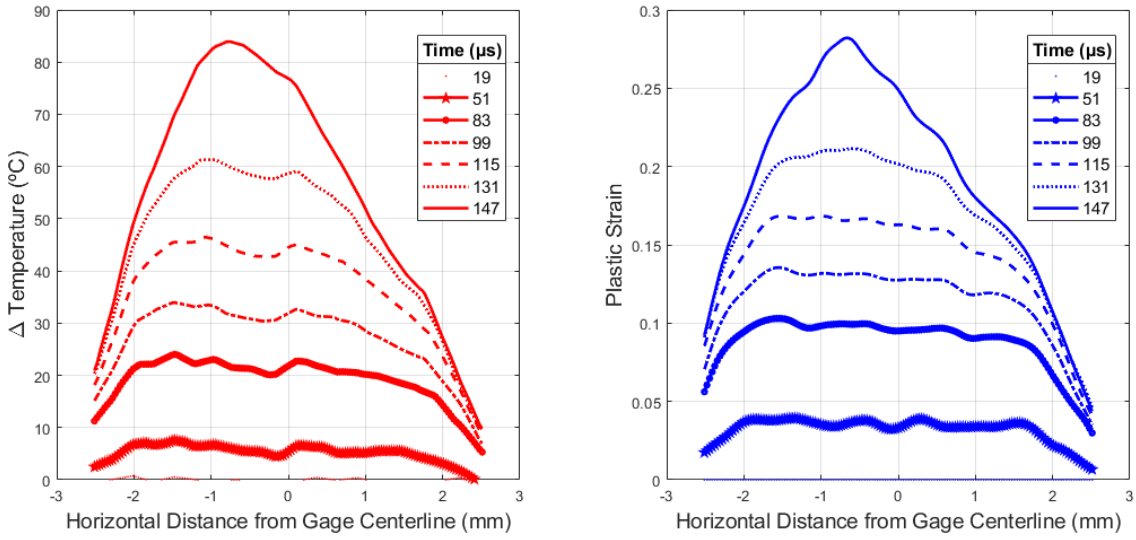

Figure 3.49 Temperature and Plastic Strain along the Gage Section for an Inconel 718 Tension Test at 2000 s^{-1}

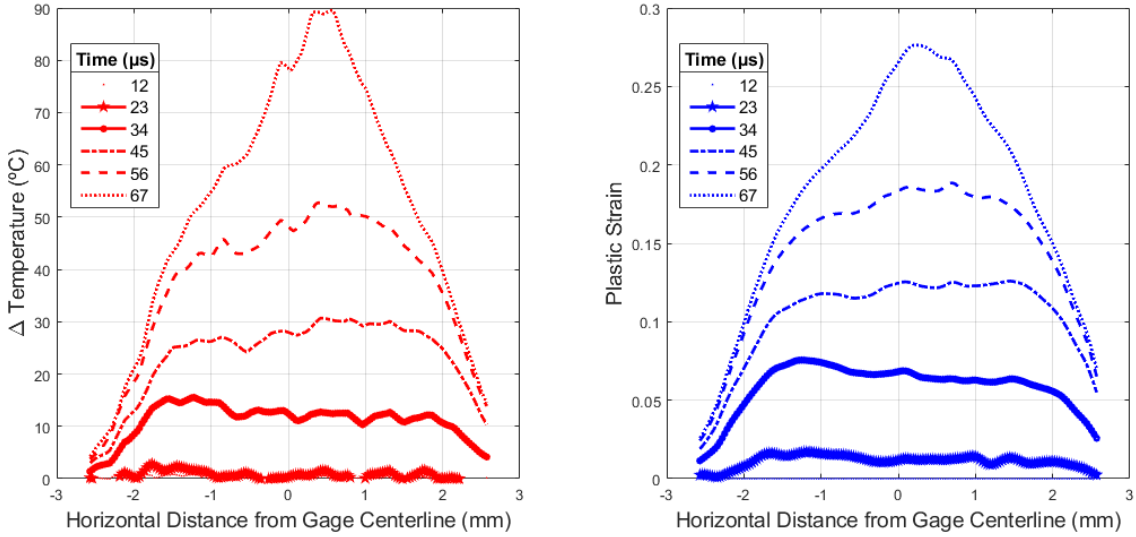

Figure 3.50 Temperature and Plastic Strain along the Gage Section for an Inconel 718 Tension Test at 6000 s^{-1}

The β and corresponding energy density measurements along the same centerline are displayed in Figure 3.51Figure 3.55. The non-adiabatic behavior of the 0.1 and 1 s^{-1} tests is shown by the increasing β outside the localization while the β remains constant with increasing strain and temperature at the center of localization. In each of the SHB tests

the β increases with increasing strain energy and therefore increasing strain. Areas with the highest strains in Figure 3.46-Figure 3.50 have the highest β s in corresponding Figure 3.51-Figure 3.55.

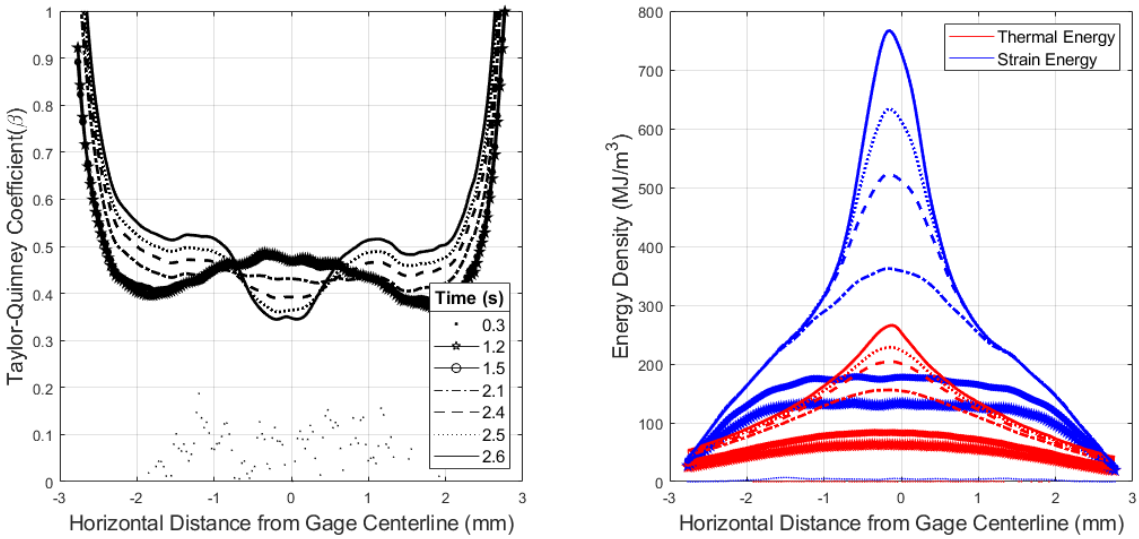

Figure 3.51 Taylor-Quinney Coefficient and Energy Density Comparison along the Gage Section for an Inconel 718 Tension Test at 0.1 s^{-1}

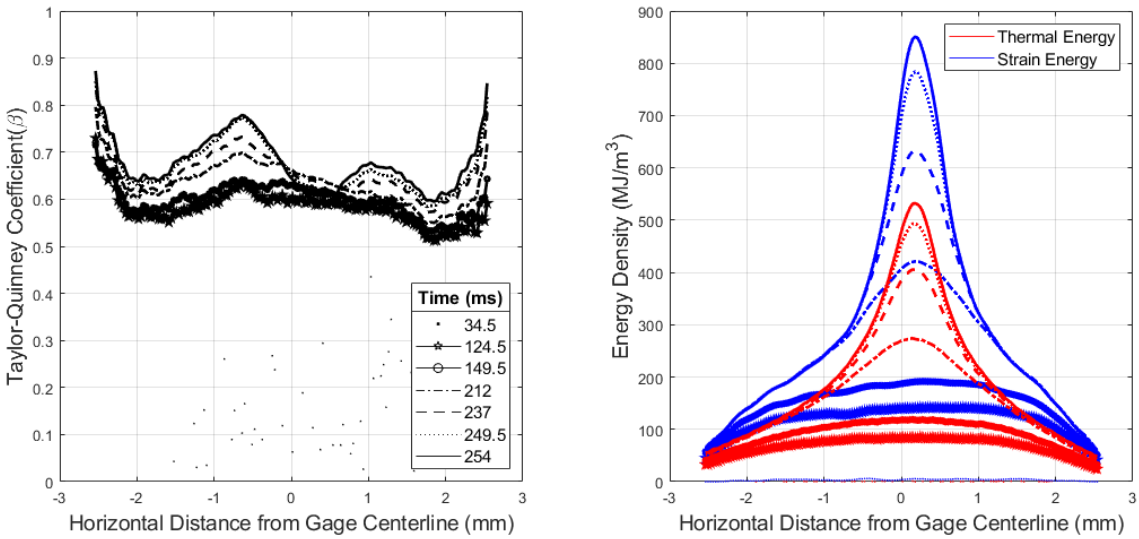

Figure 3.52 Taylor-Quinney Coefficient and Energy Density Comparison along the Gage Section for an Inconel 718 Tension Test at 1 s^{-1}

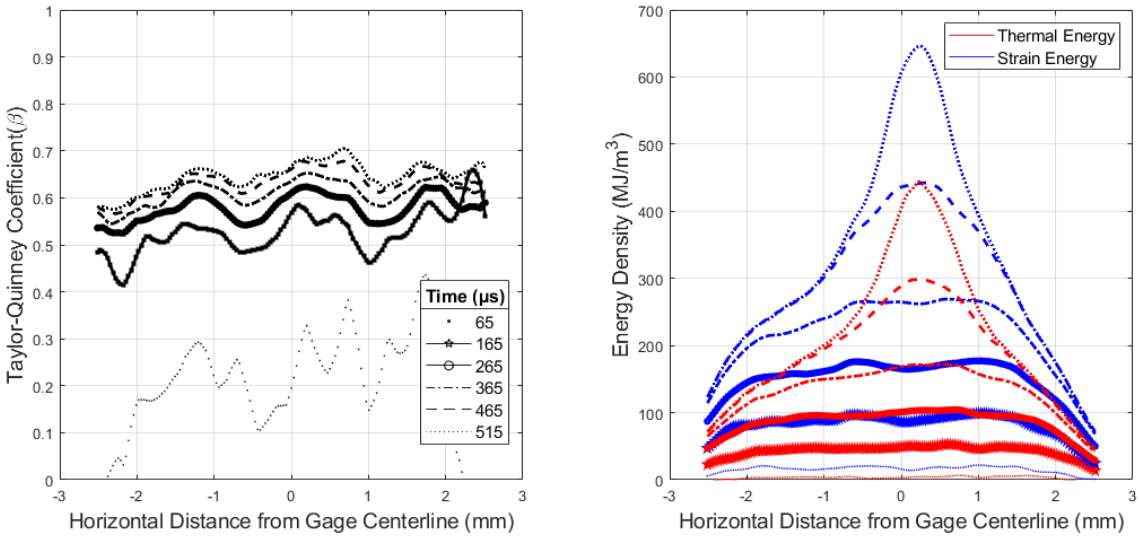

Figure 3.53 Taylor-Quinney Coefficient and Energy Density Comparison along the Gage Section for an Inconel 718 Tension Test at 500 s^{-1}

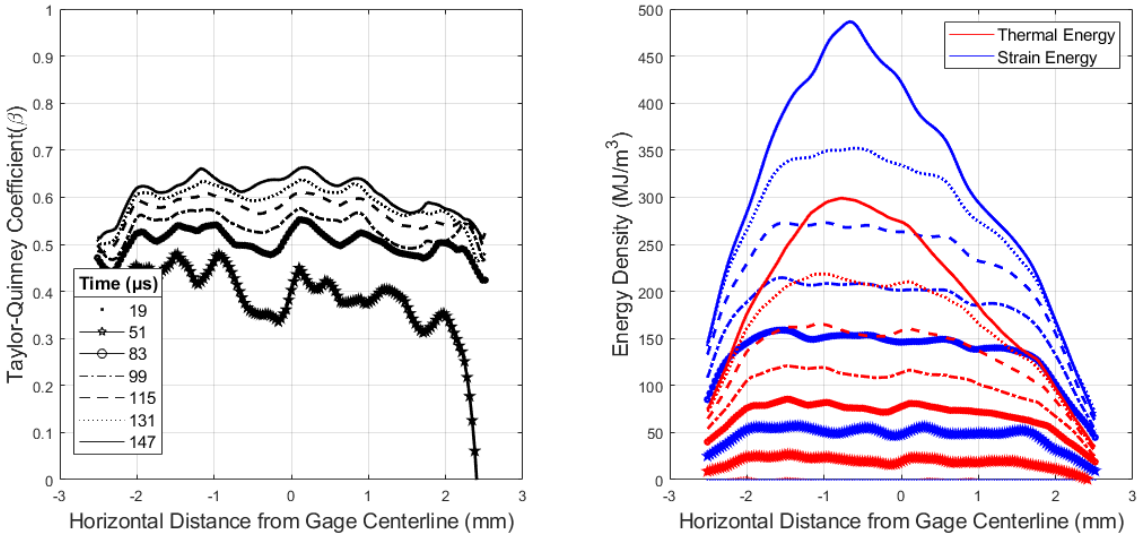

Figure 3.54 Taylor-Quinney Coefficient and Energy Density Comparison along the Gage Section for an Inconel 718 Tension Test at 2000 s^{-1}

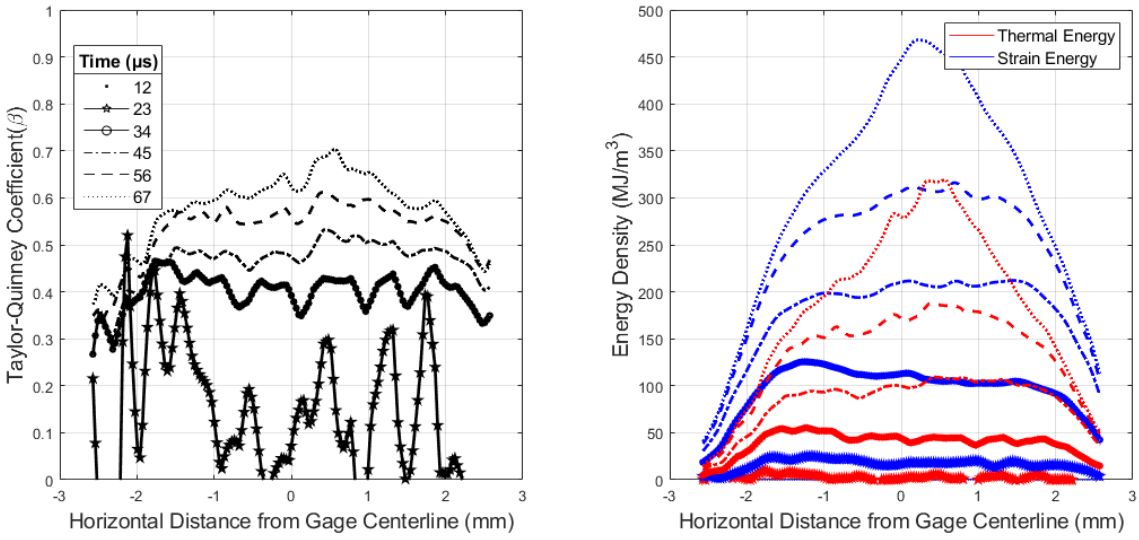

Figure 3.55 Taylor-Quinney Coefficient and Energy Density Comparison along the Gage Section for an Inconel 718 Tension Test at 6000 s^{-1}

The average Taylor-Quinney coefficient versus local plastic strain for the points located in the localization region of each Inconel 718 tension test at various strain rates is shown in Figure 3.56. At a strain rate of 0.1 s^{-1} the β increases from 0 to 0.45 as the strain increases from 0 to 0.05. Then β steadily decreases to 0.35 at a plastic strain of 0.4. In the 1 s^{-1} test the β increases from 0 to 0.6 as the plastic strain increases from 0 to 0.1 and remains constant at 0.65 up to a plastic strain of 0.475. The trend for the tests from 500-6000 s^{-1} is nearly identical. The β increases from 0 to 0.65 as the plastic strain increases from 0 to 0.15 then remains β constant up to strains of 0.35. The increase of β with increasing strain is likely due to the inability of the material to store energy as plastic work as the strain increases so the extra energy is released as heat.

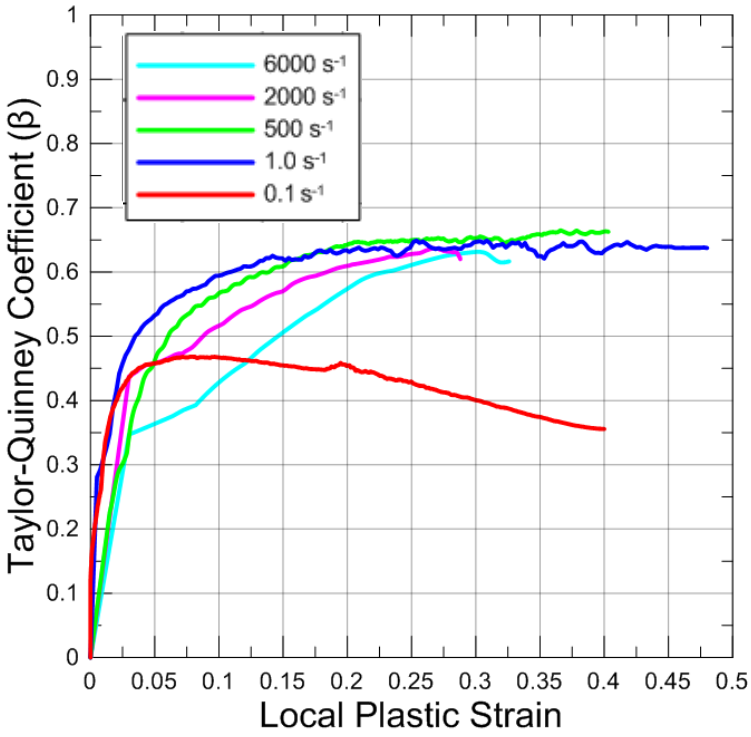

Figure 3.56 Moving Average of β vs. Plastic Strain for each Inconel 718 Tension Test

The average thermal energy densities are plotted against the strain energy densities for each of the data points in the localization regions in Figure 3.57. The linear slopes of these data points are calculated and presented in Table 3.3. The average β values will be used as the values in the LS-DYNA material model. The differences in β in Figure 3.56 can also be seen in Figure 3.57 as the slopes of the SHB tests have similar values while the slopes of the MTS tests are lower.

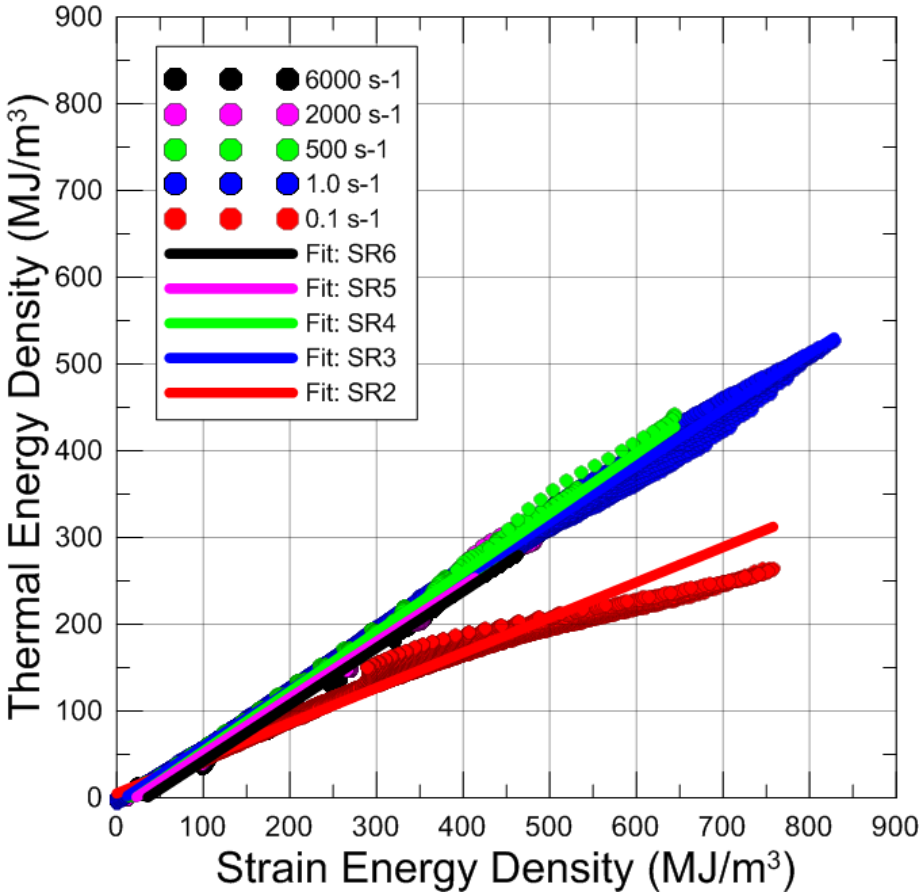

Figure 3.57 Thermal Energy Density Comparison with Strain Energy Density to Calculate Average β Values for Inconel 718

Table 3.3 Average Taylor-Quinney Coefficients for Inconel 718 based on Energy Density Comparisons

Strain Rate (s^{-1})	Average β from Slope
1.00E-02	0.406
1	0.661
500	0.686
2000	0.646
6000	0.651

Chapter 4 : Summary and Conclusions

The Taylor-Quinney coefficient is measured in tension tests of Ti-6Al-4V, aluminum 2024-T351, and Inconel 718 at strain rates from 1E-4 s^{-1} to 6000 s^{-1} using synchronized strain and temperature measurements from optical techniques. The thin, flat tension specimens of each material were cut from 12.7 mm thick plates described in Chapter 2. The experimental techniques used to determine the full-field Taylor-Quinney coefficient in each material are described at length in Chapter 2 while the results from the testing are presented in Chapter 3. Results from tests at a strain rate of 1E-4 s^{-1} were considered isothermal for all materials. The research was funded by the FAA's Aircraft Catastrophic Failure Prevention Program with the goal of developing material models to more accurately model uncontained jet engine failures. The data generated will be used by LS-DYNA Aerospace Working Group to calibrate the MAT_224, MAT_224_GYS, and MAT_264 material models.

4.1 Ti-6Al-4V Experimental Conclusions

Ti-6Al-4V exhibits significant rate dependence over the entire range of strain rates. The material exhibits increasing yield and flow stress and reduced ductility with increasing strain rate. The temperature and strain measured on the surface of the specimen is uniform during uniform deformation. The material localizes at strains between 0.03-0.05 and produces a necking region with increased local strains and temperature. At strain rates below 500 s^{-1} the test cannot be considered adiabatic as significant temperature increases are measured in regions outside the necking region

where deformation has ceased. The measured Taylor-Quinney coefficient is dependent on the level of local plastic strain. As the plastic strain increases from 0 to 0.15 β increases from 0 to 0.6 for all strain rates. Outside the localization region the measured plastic strains are less than 0.15 and thus β is not uniform across the gage section. β exhibits strain rate dependence in the 6000 s^{-1} test as the highest recorded temperature and β is measured in this test. An effective β is calculated for the 0.1 strain rate test as significant conduction takes place, reducing the thermal energy generated in the material. The average beta in the necking region is mainly uniform for the 1 s^{-1} to 2000 s^{-1} strain rate tests as the average β varies between 0.621-0.675.

4.2 Aluminum 2024-T351 Experimental Conclusions

Aluminum 2024-T351 exhibits insignificant strain rate dependence in tension as the yield stress only slightly increases while the flow stress is similar across all strain rates. The temperature and strain measured on the surface of the specimen is uniform during uniform deformation. The material localizes at a strain of 0.15 and produces a necking region with increased local strains and temperature. The measured temperature increases and β are similar for each of the 500-6000 s^{-1} tests. Aluminum has a higher thermal conductivity and exhibits lower β values for the 0.01 and 1 s^{-1} tests due to a reduction in thermal energy. β exhibits bilinear plastic strain dependence in the 500-6000 s^{-1} tests as β increases from 0 to 0.3 over a plastic strain of 0 to 0.05 and then from 0.3 to 0.5 over a plastic strain from 0.05 to 0.3. The average β is calculated from the slopes of the plot of the thermal energy generated in each tension test to the measured strain energy in each test. The average β for the 500 s^{-1} to 6000 s^{-1} tests varies between 0.485-0.533.

4.3 Inconel 718 Experimental Conclusions

The measured yield and flow stresses of Inconel 718 in tension increased with increasing strain rate. The material strain hardening rate at 0.1 and 1.0 s^{-1} is lower than that at 1E-4 s^{-1} likely due to thermal softening. The increase in temperature measured at the failure point for each tension test is within 10ºC for the tests at strain rates between 1-6000 s^{-1}. The material localization point is at strains between 0.15-0.25 and increases with increasing strain rate. The β for the strain rate tests between 1-6000 s^{-1} are constant between 0.6 and 0.625 for local plastic strains above 0.2. The average β is mainly uniform for the 1 s^{-1} to 6000 s^{-1} tests and varies between 0.651 and 0.686.

4.4 Final Comments and Future Works

The experimental results presented in this work are just a small fraction of the amount of data produced by the multiple experiments. In previous works a single value of β_{int} was calculated using an average strain and temperature increase. With the large amount of data generated in these experiments one could develop a new field method to better describe the behavior of the specimen during deformation. As this is the first set of Taylor-Quinney coefficient experiments carried out on materials with a high degree of localization these methods could be extrapolated to study other types of deformation such as shear or punch tests. It would also be prudent to study the differences in β_{int} and β_{diff} on strain, strain rate, and deformation type for different materials. The current LS-DYNA material models only calculate temperature increase using β_{int} and total plastic work where β_{diff} may be better suited to describe the temperature increases experienced by materials in with large amounts of plastic strain.

Furthermore, infrared technology is currently limited because of the pixel resolution that must be sacrificed to increase the frame rate of the cameras. By utilizing technologies that have higher frame rates but lower sensor resolutions in tandem with the infrared camera a more complete picture of the temperature rise could be realized during the high strain rate tests. Utilizing multiple infrared cameras simultaneously would also increase the data points recorded during the experiments at the highest strain rates.

References

[1] G. R. Johnson and W. H. Cook, “A constitutive model and data for metals subjected to large strains, high strain rates and high temperatures,” in *Seventh International Symposium on Ballistics*, 1983, pp. 541–547.

[2] G. R. Johnson and W. H. Cook, “Fracture characteristics of three metals subjected to various strains, strain rates, temperatures and pressures,” *Eng. Fract. Mech.*, vol. 21, no. 1, pp. 31–48, 1985.

[3] “Aircraft Accident Report-- Jnited Airlines Flight 232, McDonnell Douglas DC-10-10, Sioux Gateway Airport, Sioux City, Iowa, July 19, 1989,” 1990.

[4] J. Gaps III, “Photos: Flight 232 crash and recovery | Flight232 | siouxcityjournal.com,” *Sioux City Journal*. [Online]. Available: https://siouxcityjournal.com/flight232/photos-flight-crash-and-recovery/collection_be2438a8-6880-5380-8c6c-afb54493c019.html#4. [Accessed: 27-Nov-2018].

[5] *Omnibus Budget Reconciliation Act of 1990*. 101st Unite States Congress, 1990.

[6] J. T. Ha mmer, “Plastic Deformation and Ductile Fracture of Ti-6Al-4V under Various Loading Conditions.” 2012.

[7] A. Ressa, “Plastic Deformation and Ductile Fracture Behavior of Inconel 718.” 2015.

[8] J. D. Seidt, “Plastic Deformation and Ductile Fracture of 2024-T351 Aluminum under Various Loading Conditions.” 2010.

[9] T. J. Liutkus, “Digital Image Correlation in Dynamic Punch Testing and Plastic Deformation Behavior of Inconel 718,” The Ohio State University, The Ohio State University, 2014.

[10] R. S. Yatnalkar, “Experimental Investigation of Plastic Deformation of Ti-6Al-4V under Various Loading Conditions,” p. 81, 2010.

[11] S. H. Haight, “An anisotropic and asy mmetric material model for simulation of metals under dynamic loading,” 2016.

[12] F. Report, “Development of a New Metal Material Model in LS-DYNA ® Part 1 : FAA , NASA , and Industry Collaboration Background,” 2014.

[13] D. Rittel, L. H. Zhang, and S. Osovski, “The dependence of the Taylor–Quinney

coefficient on the dynamic loading mode," *J. Mech. Phys. Solids*, vol. 107, pp. 96–114, 2017.

[14] J. Hodowany, G. Ravichandran, a Rosakis, and P. Rosakis, "Partition of plastic work into heat and stored energy in metals," *Exp. Mech.*, vol. 40, no. 2, pp. 113–123, 2000.

[15] J. J. Mason, A. J. Rosakis, and G. Ravichandran, "On the strain and strain rate dependence of the fraction of plastic work converted to heat: an experimental study using high speed infrared detectors and the Kolsky bar 1," *Mech. Mater.*, vol. 17, pp. 135–145, 1994.

[16] W. S. Farren and G. I. Taylor, "The Heat Developed during Plastic Extension of Metals," *Proc. R. Soc. London*, vol. 107, pp. 422–451, 1925.

[17] H. Quinney and G. I. Taylor, "The latent energy remaining in a metal after cold working," *Proc. R. Soc. London*, vol. A 143, no. 849, pp. 307–326, 1934.

[18] M. B. Bever, D. L. Holt, and a L. Titchner, "The Stored Energy of Cold Work," *Prog. Mater. Sci.*, vol. 17, pp. 1–177, 1973.

[19] A. T. Zehnder and A. J. Rosakis, "On the temperature distribution at the vicinity of dynamically propagating cracks in 4340 steel," *J. Mech. Phys. Solids*, vol. 39, no. 3, pp. 385–415, 1991.

[20] D. Rittel, "On the conversion of plastic work to heat during high strain rate deformation of glassy polymers," *Mech. Mater.*, vol. 31, no. 2, pp. 131–139, 1999.

[21] S. Nemat-nasser and R. Kapoor, "Determination of temperature rise during high strain rate deformation," *Mech. Mater.*, vol. 27, pp. 1–12, 1998.

[22] D. A. S. Macdougall and J. Harding, "The measurement of specimen surface temperature in high-speed tension and torsion tests," *Int. J. Impact Eng.*, vol. 21, no. 6, pp. 473–488, 1998.

[23] D. Macdougall, "Determination of the plastic work converted to heat using radiometry," *Exp. Mech.*, vol. 40, no. 3, pp. 298–306, 2000.

[24] A. Saai, H. Louche, L. Tabourot, and H. J. Chang, "Experimental and numerical study of the thermo-mechanical behavior of Al bi-crystal in tension using full field measurements and micromechanical modeling," *Mech. Mater.*, vol. 42, no. 3, pp. 275–292, 2010.

[25] W. Oliferuk, M. Maj, and K. Zembrzycki, "Determination of the Energy Storage Rate Distribution in the Area of Strain Localization Using Infrared and Visible Imaging," *Exp. Mech.*, vol. 55, no. 4, pp. 753–760, 2015.

[26] A. Eisenlohr, I. Gutierrez-Urrutia, and D. Raabe, “Adiabatic temperature increase associated with deformation twinning and dislocation plasticity,” *Acta Mater.*, vol. 60, no. 9, pp. 3994–4004, 2012.

[27] J. A. Rodríguez-Martínez, R. Pesci, and A. Rusinek, “Experimental study on the martensitic transformation in AISI 304 steel sheets subjected to tension under wide ranges of strain rate at room temperature,” *Mater. Sci. Eng. A*, vol. 528, no. 18, pp. 5974–5982, 2011.

[28] P. Knysh and Y. P. Korkolis, “Determination of the fraction of plastic work converted into heat in metals,” *Mech. Mater.*, vol. 86, pp. 71–80, 2015.

[29] E. Charkaluk, R. Seghir, L. Bodelot, J.-F. Witz, and P. Dufrénoy, “Microplasticity in Polycrystals: A Thermomechanical Experimental Perspective,” *Exp. Mech.*, vol. 55, no. 4, pp. 741–752, 2015.

[30] J. El Yagoubi, J. Lamon, J.-C. Batsale, J. Dhote, and M. Le Flem, “Multiscale Thermal Characterization of Mechanically Loaded Ceramic Matrix Composite: Estimation of Thermal Diffusivity at Micro/Mesoscale,” *Exp. Mech.*, vol. 55, no. 4, pp. 783–794, 2015.

[31] S. Dumoulin, H. Louche, O. S. Hopperstad, and T. Børvik, “Heat sources, energy storage and dissipation in high-strength steels: Experiments and modelling,” *Eur. J. Mech. A/Solids*, vol. 29, no. 3, pp. 461–474, 2010.

[32] G. H. Staab and A. Gilat, “A direct-tension split Hopkinson bar for high strain-rate testing,” *Exp. Mech.*, vol. 31, no. 3, pp. 232–235, Sep. 1991.

[33] K. Ogawa, “Impact-tension compression test by using a split-Hopkinson bar,” *Exp. Mech.*, vol. 24, no. 2, pp. 81–86, Jun. 1984.

[34] M. A. Sutton, J. J. Orteu, and H. Schreier, *Image correlation for shape, motion and deformation measurements: Basic concepts, theory and applications*. Boston, MA: Springer US, 2009.

[35] C. Solutions, “Inc. Coorrelated Solutions.” 2018.

[36] TELOPS, “Telops Infrared Camera User’s Guide,” no. January, 2016.

[37] L. del Campo *et al.*, “Emissivity measurements on aeronautical alloys,” *J. Alloys Compd.*, vol. 489, no. 2, pp. 482–487, 2010.

[38] B. P. Keller, S. E. Nelson, K. L. Walton, T. K. Ghosh, R. V. Tompson, and S. K. Loyalka, “Total hemispherical emissivity of Inconel 718,” *Nucl. Eng. Des.*, vol. 287, pp. 11–18, 2015.

[39] L. González-Fernández, E. Risueño, R. B. Pérez-Sáez, and M. J. Tello, “Infrared normal spectral emissivity of Ti–6Al–4V alloy in the 500–1150K temperature range,” *J. Alloys Compd.*, vol. 541, pp. 144–149, 2012.